UNIVERSITÀ DEGLI STUDI DI PADOVA
DIPARTIMENTO DI INGEGNERIA CIVILE, EDILE E AMBIENTALE
Department Of Civil, Environmental and Architectural Engineering

Master Degree in Mathematical Engineering

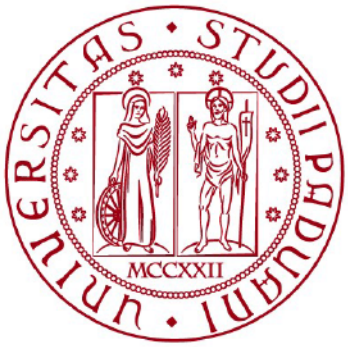

Final Dissertation

DEVELOPMENT OF SURFACE INTEGRAL EQUATION METHODS FOR ELECTROMAGNETIC PROBLEMS

Supervisor:
Dr. Francesco Lucchini

Candidate:
Samuele Segato

ACADEMIC YEAR 2022-2023

Contents

Abstract

In the field of computational electromagnetism, Integral Equation Methods (IEM) represent a valid alternative to Finite Element Methods (FEM), implemented in most commercial software. The peculiarity of IEM lies in the fact that discretization of electromagnetically inactive domains, such as the volume of air in which the studied device can be immersed, is not required, thus reducing the number of degrees of freedom of the problem (DOFs). This characteristic becomes particularly interesting for analyzing open boundary problems, for example involving antennas, where mesh generation would be particularly demanding. IEM are subdivided into Volume Integral Methods (VIE) and Surface Integral Methods (SIE). In particular, the second type results advantageous in physical cases where currents are located in surficial regions, thus requiring the discretization only of the surfaces of the device. This situation applies, for example, to the analysis of high-frequency interconnections in which current density naturally distributes on the surfaces of the conductors due to a marked skin effect. A limitation for integral methods compared to FEM, however, is the generation of dense matrices, coming from Galerkin formulation, rather than sparse ones for solving the problem. In this way, given the quadratic growth of the matrix dimensions with the DOFs, the computational load for memorization and inversion of the matrices could become onerous. Therefore, compression techniques based on the geometry of the problem are necessary, where elements distant from each other in space and experiencing weak mutual interactions are stored within a convenient way. An interesting technique which implements this condition is based on Hierarchical Matrix method (H-matrices). In this context, the thesis work focuses on the development of integral methods for the analysis of electromagnetic problems with specific attention to SIE. In particular, the state of art of the techniques presented in the literature is analyzed from both a theoretical and experimental point of view through the development of codes in MATLAB. Furthermore, the aforementioned compression techniques (H-matrices) are applied to large-scale problems to demonstrate their validity.

Chapter 1

Introduction

The *Finite Element Method* (FEM) is probably the most known and the most important numerical approach for solving partial differential equations and integral equations. Thanks to its generality, it can be applied to a wide number of problems, including static or dynamic problems, linear or less, and treating homogeneous or heterogeneous domains with complex geometries. Thanks to its ease of application, it can be implemented through many programming languages also making codes easily comparable. Thanks to its structure, it can be conveniently stored using sparse matrices which allows to save a lot of CPU memory and to consistently reduce CPU time demand even for large-size problems. In the field of application of electromagnetism, this is in general not different. When small components which keep the electrical field or the magnetic one confined in a small region (e.g. a capacitor or a solenoid having small dimensions) are involved, the FEM results in the best way to solve the formulated problem. The FEM is also implemented in the main commercial software for solving electromagnetic problems such as COMSOL®, and ANSYS®.

However, there are many situations in which the FEM approach turns out to be non-optimal. Some main examples concern the electric or magnetic field generated by a distribution of current charge, the study of propagation fields due to e.g. antennas, and the study of the behavior of fields at high frequencies. The first condition results particularly demanding when we look for the solution in a specific point of the domain, but the searched solution is difficult, if not even impossible, to be computed from the analytical point of view. On the other hand, the second eventuality requires the discretization of the whole domain in which the field is defined and so it can make the process very onerous from the computational point of view.

To overcome such issues, another kind of approach was introduced. This method is known as the *Integral Equation Method* (IEM) and it exploits a reformulation of the original problem based on the introduction - as the name itself states - of integral equations expressed as a function of alternative unknowns which are defined concerning equivalent sources.

The IEM started to be introduced around the '40s, aiming to solve problems re-

lated to Maxwell's equations as an alternative to solvers based on partial differential equations such as the FEM itself or the *Finite Difference Method* (FDM). Indeed, such techniques are based on the research of the direct solution for the aforementioned kinds of problems. Conversely, IEMs are based on the reformulation of the statement as a function of alternative sources and boundary conditions. Then, similarly to FEM, the discretization of the domain is required to approximate the solution of the problem. This way IEM provides a very convenient way to reach the result, overcoming the issues discussed above or e.g. related to complex open-boundary region scattering and radiation problems: on one hand IEM are very general and flexible and they give an alternative way to solve problems whose analytical solution is not computable. Moreover, they allow consistent reduction of the load associated with the discretization of the domain when open-boundary problems are involved, e.g. when the study of the propagation of fields is required: indeed, IEM asks for the discretization of the only active part of the domain, while the mesh of the air or of the medium in which the field propagates is not necessary, thus considerably reducing the load for the computation and the application of the mesh.

Among the IEM, two main categories can be identified: *Volume Integral Equations* (VIE) and *Surface Integral Equations* (SIE). The first type is based on the discretization of the whole three-dimensional domain over which the problem is defined. Such a method maintains all the advantages listed above and it results particularly conveniently when the three sizes of the involved domain are comparable to one another. On the other hand, SIE shows its effectiveness when one of the dimensions of the domain is negligible concerning the other two when the charge density is concentrated along the surface of the domain, or again when an electromagnetic scattering signal at very high frequency localizes along the external walls e.g. of a conductor because of an important *skin effect*.

The skin effect is an electromagnetic phenomenon that occurs when an electromagnetic field penetrates a conductor. For high-frequency conductors current flux concentrates primarily in the outer part of the conductor, generating a sort of "skin" through which the current flows. Such behavior is due to the induction of eddy currents flowing in the opposite direction inside the core of the conductor, thus reducing the area through which the current effectively moves. The skin effect is even stronger at high frequencies, as at low frequencies the field would have penetrated more uniformly into the conductor. The result is an increase in the apparent resistance of the conductor at high frequencies compared to what one would expect based solely on the resistivity of the material. The approximate formula for the depth of penetration (or "skin depth", Fig.1.1) δ in a conductor is given by:

$$\delta = \sqrt{\frac{2}{\omega\mu\sigma}} \tag{1.1}$$

where ω is the angular frequency of the wave, μ is the magnetic permeability of the

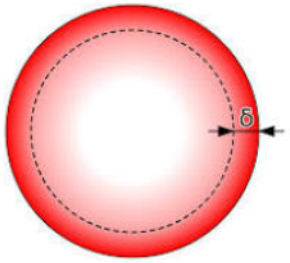

Figure 1.1: Graphical representation of the skin depth in a circular conductor.

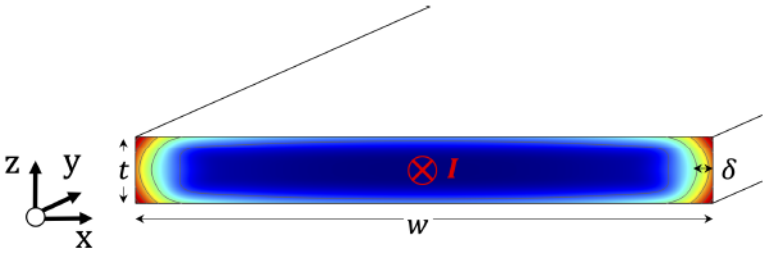

Figure 1.2: Skin effects on the rectangular copper coil with $w = 6{\cdot}10^{-4}$ m and $t = 7{\cdot}10^{-5}$ m.

conductor's material, and σ is the electrical conductivity of the conductor's material. More in detail the skin effect increases in the equivalent resistance of the conductor at high frequencies due to the redistribution of the currents.

The skin effect is encountered in various applications where electromagnetic fields and high-frequency currents play a crucial role. Some important examples include high-voltage power transmission lines, especially at radio frequencies (RF), where the skin effect influences the distribution of current in the conductors; microwave systems, for which the skin effect affects the behavior of conductors and transmission lines, impacting signal integrity and power distribution; antennas whose design and performance are influenced by the skin effect, particularly in high-frequency communication systems; high-frequency electronics, telecommunication systems, submarine communication cables, and electromagnetic shielding. It is important to understand why complete knowledge in terms of theory and managing the skin effect is crucial to optimize the performance and the efficiency of systems that involve high-frequency electromagnetic fields.

A graphical example of the skin effect over the rectangular cross-section of a conductor is depicted in Fig. 1.2. This way it directly becomes clear why for the skin effect the discretization of the domain along one of the dimensions would require the adoption of very small elements to accurately capture the distribution of the current density, thus making the process quite demanding. Alternatively, it is also possible to highlight this issue when a mesh with constant size along the three directions is adopted: if this was the case when the small size is taken into account, small elements would have been

defined to obtain an acceptable solution, but the total number of elements along the other two dimensions would have become very huge. In this perspective, SIE allows to neglect the discretization along the highlighted dimension and they look for the solution of a new problem whose statement has a domain coincident with the surface of the considered body or electrical component. This way also the number of unknowns is dramatically reduced. However, nowadays SIE has not found a well-defined field of application because of some theoretical questions specifically related to functions that present singularities of any kind and which have to be properly discussed. The SIE approach is available in commercial software such as FEKO®.

Furthermore, despite all the advantages presented by IEM, one important issue regards the storage of matrices describing the problem. Differently from what happens when FEM is applied, IEM generates dense matrices having several entries which scale as $\mathcal{O}(N^2)$ where N is the number of the degrees of freedom (DOFs) of the problem. We can consider as an example Maxwell's equation expressing the electric field, for which the Green function

$$G(\mathbf{r}, \mathbf{r}') = \frac{e^{ik\|\mathbf{r}-\mathbf{r}'\|}}{4\pi\|\mathbf{r}-\mathbf{r}'\|} \tag{1.2}$$

is strongly involved. We can suppose to consider a matrix whose entries are defined by such expression, where $\mathbf{r}$ and $\mathbf{r}'$, which are vectors identifying two points in the space, now describe the indices of the matrix itself, respectively along its rows and columns. Even if the Green function can assume very small values, it always provides positive results (a much in-depth analysis of its singular values which appear for self-interacting elements, i.e. elements along the diagonal, will be carried out in the following chapters), and this makes the entries of the matrix not vanish even when the denominator approaches infinity. Another direct consequence of such an issue concerns the CPU time required: indeed, from this point of view, the greater the number of entries different from zero is, the greater the cost for the inversion of the matrix will be, as well as the one for the application of the solver. Indeed, it was shown that the time for matrix inversion can scale even with order $\mathcal{O}(N^3)$).

Just for clarity, an example of the patterns of the system matrices arising from FEM and IEM discretization approaches are illustrated in Fig. 1.3. Here it can be noticed that, keeping constant the number of DOFs, the null-entries stored by the FEM method is much higher, so that the matrix in Fig. 1.3a can be considered as a sparse matrix, while the one obtained from IEM (Fig. 1.3a) can be not.

Even if questions related to the density of the matrix can be neglected for small-order problems having only a few unknowns, when the number of DOFs increases such issues must be properly treated. Indeed, if the CPU time and memory requirements become too large, the convenience of IEM concerning the FEM would vanish. That's why specific techniques for the compression of matrices and the consequent memory saving should be adopted, bringing also the reduction of the computation time. Among these methods, two main families can be distinguished. The first one is based on the

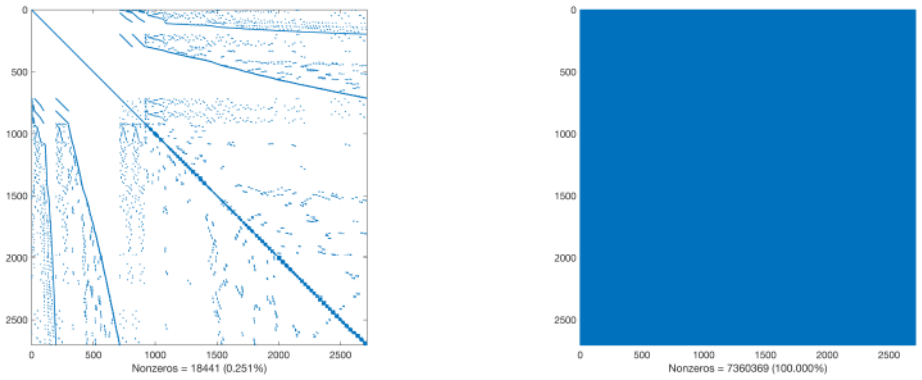

(a) FEM. (b) IEM.

Figure 1.3: Example of the pattern of matrices from FEM (a) and IEM (b) approaches.

decomposition of the function expressing the entries of the matrix, while the second one is based on the concrete relation between the elements obtained from the discretization. If we refer to the first approach as *mathematical* or *physical* approach since the function is analyzed with a theoretical perspective, the second one is denoted as *geometrical* because it allows exploiting such kind of considerations, i.e. the mutual distance between elements, so that if they are close to each other their respective interaction is, in general, stronger, while the contribution of elements far from each other can be neglected inside the entries of the matrix if properly treated.

From this perspective, this thesis work was developed. The main scope is to provide a general survey about the IEM, with specific attention to both theoretical and numerical analysis for the SIE, which should give the majority of the tools for choosing which of the methods for solving linear problems is the best option, case by case. The work is divided as follows: Chapter 2 provides a general analytical overview of Maxwell's equation. The respective integral equations that arise from them after the application of the Galerkin method for the solution of the Method of Moments are described as well. Finally, the matricial version of the problem obtained from the application of numerical reasoning is introduced. This formulation is fundamental in the treatment of the Integral equations. Chapter 3 is split into two sections: the first one focuses on the application of SIE, describing one by one many possible alternatives to suitably treat the singularities that appear inside the problem; the second one compares the results obtained using each method - with particular attention to the *modified line integral* one - and a fully numeric approach to verify the consistency of the adopted formulations. Examples whose analytical solutions are known from the state of the art are adopted in this second section, to check how well the SIE can approximate the results. Chapter 4 is finally fully dedicated to methods for matrix compression and model order reduction. First, a theoretical analysis of many distinct methods with their pros and cons will be reported. Then, the importance of such techniques, and in particular of the *Hierarchical matrices* method, will be stressed by their application to concrete numerical examples.

About the notation that is adopted in the following chapters, square brackets in general indicate the matricial behavior of the component. The bold character is adopted to refer to a vector (small letter) or a matrix (capital letter).

Chapter 2

Integral Equation Methods

In this chapter, the Integral Equation Method (IEM) for the solution of electromagnetic (EM) problems is introduced. The purpose of the discussion is to give a brief overview of the mathematical formulation of the IEMs, indeed, a detailed discussion of this topic can be found in many books, such as [1]. The starting point of the discussion, is the well-known Maxwell's equations, governing the physical behavior of the electromagnetic field in the domain $\Omega \subset \mathbf{R}^3$, here written in the frequency domain:

$$\nabla \times \mathbf{E} = -i\omega\mathbf{B} \tag{2.1}$$

$$\nabla \times \mathbf{H} = \mathbf{J}_c + i\omega\mathbf{D} \tag{2.2}$$

$$\nabla \cdot \mathbf{D} = \varrho_c \tag{2.3}$$

$$\nabla \cdot \mathbf{B} = 0 \tag{2.4}$$

where $\mathbf{E}$ is the electric field, $\mathbf{B}$ is the magnetic flux density field, $\mathbf{D}$ is the electric displacement field, $\mathbf{H}$ is the magnetic field, $\mathbf{J}_c$ is the conduction current density, ϱ_c is the free volume charge density, and $\omega = 2\pi f$ is the angular frequency. The constitutive relations that allow connecting field intensities and flux densities and which close the problem from the mathematical point of view involve electric permittivity $\varepsilon = \varepsilon_r\varepsilon_0$ and magnetic permeability $\mu = \mu_r\mu_0$:

$$\mathbf{D} = \varepsilon\mathbf{E}, \quad \mathbf{B} = \mu\mathbf{H}. \tag{2.5}$$

In the most general case, i.e. for an inhomogeneous and anisotropic body, these quantities are 3x3 matrices, but in this work, we assume to treat homogeneous and isotropic materials, so that ε and μ are assumed to be scalar constants multiplied by the Identity matrix which is neglected in the following. The current density and the electric field are related through the constitutive relation for the current field:

$$\mathbf{J}_c = \sigma\mathbf{E}, \tag{2.6}$$

where σ is the electric conductivity. Thanks to the fact that $\mathbf{B}$ is divergence-free, focusing on the quantities which are related to the electric field, it's also possible to introduce the *magnetic vector potential* or simply *vector potential* $\mathbf{A}$ such that:

$$\mathbf{B} = \nabla \times \mathbf{A}. \tag{2.7}$$

By inserting this equation into Faraday's law (2.1) and employing the vector calculus identity stating $\nabla \times \nabla[\bullet] = 0$, it's also possible to introduce the *electric scalar potential* φ_e, which makes the following equality hold:

$$\mathbf{E} = -i\omega\mathbf{A} - \nabla\varphi_e. \tag{2.8}$$

2.1 Electric and Magnetic Field Integral Equations

Starting from Faraday's law (2.1) rewritten in terms of magnetic and scalar potentials (2.8), the foundations of integral equations are briefly described in this section. This analysis aims to define an integral form involving the fields $\mathbf{A}$ and φ_e, linking them with their physical sources. From these expressions, it will be also possible to obtain an integral equation for $\mathbf{E}$ as a function of its sources. The analysis starts by coupling Maxwell-Ampere's law (2.2) with the first of the constitutive laws (2.5), and noticing that $\mathbf{H} = 1/\mu_0 \nabla \times \mathbf{A}$ we end up with the formula:

$$\frac{1}{\mu_0}\nabla \times (\nabla \times \mathbf{A}) = \mathbf{J}_c + i\omega\varepsilon_0\mathbf{E}. \tag{2.9}$$

Then we can apply the vector identity $\nabla \times (\nabla \times [\bullet]) = \nabla(\nabla \cdot [\bullet]) - \nabla^2[\bullet]$ to the left-hand side of the equation, while we substitute equation (2.8), getting the formula:

$$\frac{1}{\mu_0}(\nabla(\nabla \cdot \mathbf{A}) - \nabla^2\mathbf{A}) = \mathbf{J}_c + i\omega\varepsilon_0(-i\omega\mathbf{A} - \nabla\varphi_e). \tag{2.10}$$

Finally the *Lorenz gauge* $\nabla \cdot \mathbf{A} = -i\omega\varepsilon_0\mu_0\varphi_e$ allows to separate $\mathbf{A}$ from φ_e in order to conclude:

$$\mu_0\mathbf{J}_c = (i\omega)^2\mu_0\varepsilon_0\mathbf{A} - \nabla^2\mathbf{A} = \Box\mathbf{A}, \tag{2.11}$$

where $\Box := (i\omega)^2 c_0^2 - \nabla^2$ is the *d'Alembertian operator*. The solution of such an equation can be derived from a well-known partial differential equation:

$$\nabla^2 G(\mathbf{r}, \mathbf{r}') + \beta G(\mathbf{r}, \mathbf{r}') = -\delta(\mathbf{r}, \mathbf{r}'), \tag{2.12}$$

where $\delta(\mathbf{r}, \mathbf{r}')$ is the Dirac delta and $G(\mathbf{r}, \mathbf{r}')$ is the *Green's function* given by the formula:

$$G(\mathbf{r}, \mathbf{r}') = \frac{e^{ikR}}{4\pi R}, \tag{2.13}$$

where again i is the imaginary unit, R is defined as the distance between the observation and source points, $R = \|\mathbf{r} - \mathbf{r}'\|$, and the complex wavenumber has the form:

$$k = \omega\sqrt{\varepsilon\mu} = k' + ik'', \tag{2.14}$$

which, for the case of non-magnetic materials (i.e., when $\mu_r = 1$), is usually expressed as:

$$k = \frac{\omega}{c_0}\sqrt{\varepsilon_r + i\frac{\sigma}{\varepsilon_0\omega}} \tag{2.15}$$

where c_0 is the speed of light in vacuum, approximately of $3 \cdot 10^8$ m/s. Based on these assumptions, we get the integral form for the magnetic vector potential $\mathbf{A}$:

$$\mathbf{A}(\mathbf{r}) = \mu_0 \int_{\Omega_c} \mathbf{J}_c(\mathbf{r}')G(\mathbf{r}, \mathbf{r}')d\mathbf{r}', \tag{2.16}$$

where Ω_c here stands for the "conductive" domain, i.e., the subset where the conduction current density $\mathbf{J}_c$ is non-zero. There exists also a simplified version which holds when the frequency-dependent terms are negligible, i.e. when $\omega^2\mu_0\varepsilon_0 \to 0$ and the dynamic version of Green's equation is substituted by its static form:

$$\mathbf{A}(\mathbf{r}) = \mu_0 \int_{\Omega_c} \mathbf{J}_c(\mathbf{r}')G_0(\mathbf{r}, \mathbf{r}')d\mathbf{r}', \tag{2.17}$$

where the static Green function is defined as:

$$G_0 = \frac{1}{R}. \tag{2.18}$$

Recalling the Lorenz gauge, we can exploit this formula aiming to develop an integral equation for φ. To do that we also introduce a vector calculus identity stating that for a vector field $\mathbf{\Lambda}$ and a scalar field α, $\nabla \cdot (\alpha\mathbf{\Lambda}) = \alpha\nabla \cdot \mathbf{\Lambda} + \nabla\alpha \cdot \mathbf{\Lambda}$. Therefore the result we get is:

$$\begin{aligned} -i\omega\varphi_e(\mathbf{r}) = \frac{\nabla \cdot \mathbf{A}(\mathbf{r})}{\varepsilon_0\mu_0} &= \varepsilon_0^{-1} \int_{\Omega_c} \nabla \cdot (\mathbf{J}_c(\mathbf{r}')G(\mathbf{r}, \mathbf{r}'))d\mathbf{r}' \\ &= -\varepsilon_0^{-1} \int_{\Omega_c} \nabla \cdot \mathbf{J}_c(\mathbf{r}') \cdot \nabla' G(\mathbf{r}, \mathbf{r}')d\mathbf{r}', \end{aligned} \tag{2.19}$$

where in the last equality we have applied the vector identity presented above and we have noticed that $\nabla \cdot \mathbf{J}_c(\mathbf{r}') = 0$ and $\nabla G(\mathbf{r}, \mathbf{r}') = -\nabla' G(\mathbf{r}, \mathbf{r}')$ meaning that the ∇ operator acts no longer on $\mathbf{r}$ but on $\mathbf{r}'$. Finally the continuity equation for $\mathbf{J}_c$ should be introduced. Let's define ς_c as the *free surface electric charge density* laying on a surface over which $\mathbf{J}_c$ is discontinuous and let's denote with $\mathbf{J}_c^{\pm}$ the two sides of the discontinuity surface, while the outer normal is described as $\hat{n}$; then

$$\nabla' \cdot \mathbf{J}_c(\mathbf{r}') = -i\omega\varrho_c(\mathbf{r}'), \qquad (\mathbf{J}_c^+(\mathbf{r}') - \mathbf{J}_c^-(\mathbf{r}')) \cdot \mathbf{n} = -i\omega\varsigma_c(\mathbf{r}'). \tag{2.20}$$

As we mentioned before, our reasoning is focused on the case of an homogeneous medium, so that the only discontinuity surface that can be identified is the boundary of the domain Ω_c, $\partial\Omega_c = \Gamma_c$ and the second equation in (2.20) has components $\mathbf{J}_c^+(\mathbf{r}') = 0$ (indeed this side of the surface belongs to Ω_c) and

$$\mathbf{J}_c^-(\mathbf{r}') \cdot \mathbf{n} = i\omega\varsigma_c(\mathbf{r}) = \mathbf{J}_c(\mathbf{r}') \cdot \mathbf{n}. \tag{2.21}$$

Applying the divergence theorem to the first term on the right-hand side of equation (2.19) and substituting equation (2.21) into the resulting one, we end up with the final form of the integral equation for the scalar potential φ:

$$\varphi_e(\mathbf{r}) = \varepsilon_0^{-1}\left[\int_{\Gamma_c} \varsigma_c(\mathbf{r}')G(\mathbf{r},\mathbf{r}')d\Gamma' + \int_{\Omega_c} \varrho_c(\mathbf{r}')G(\mathbf{r},\mathbf{r}')d\mathbf{r}'\right]. \tag{2.22}$$

Finally, it's possible to adopt the two integral equations (2.16) and (2.22), and substitute them into equation (2.8) to develop an equation which will be fundamental in electromagnetic problem's formulation. Such equation is known as *Electric Field Integral Equation*, or simply EFIE:

$$\begin{aligned}\mathbf{E}(\mathbf{r}) = &- i\omega\mu_0 \int_{\Omega_c} \mathbf{J}_c(\mathbf{r}')G(\mathbf{r},\mathbf{r}')d\mathbf{r}' \\ &- \varepsilon_0^{-1}\nabla\left[\int_{\Gamma_c} \varsigma_c(\mathbf{r})'G(\mathbf{r},\mathbf{r}')d\Gamma' + \int_{\Omega_c} \varrho_c(\mathbf{r}')G(\mathbf{r},\mathbf{r}')d\mathbf{r}'\right],\end{aligned} \tag{2.23}$$

which can be also rewritten as a function of the only $\mathbf{J}_c$ using the respective continuity equation (2.20):

$$\begin{aligned}\mathbf{E}(\mathbf{r}) = &- i\omega\mu_0 \int_{\Omega_c} \mathbf{J}_c(\mathbf{r}')G(\mathbf{r},\mathbf{r}')\mathbf{r}' \\ &- \frac{\nabla}{i\omega\varepsilon_0}\left[\int_{\bar{\Gamma}_c} (\mathbf{J}_c^+(\mathbf{r}')\mathbf{J}_c^-(\mathbf{r}')) \cdot \hat{n}G(\mathbf{r},\mathbf{r}')d\Gamma' + \int_{\Omega_c} \nabla' \cdot \mathbf{J}_c(\mathbf{r}')G(\mathbf{r},\mathbf{r}')d\mathbf{r}'\right].\end{aligned} \tag{2.24}$$

The integral equations object of the thesis arises from the coupled electromagnetic problems, i.e. when the electric field interacts with a magnetic one. In this case, the EFIE shown in (2.23) should be modified with the introduction of a new term due to the presence of the magnetic field itself. Moreover the current density should now be identified trough a subscript which verifies wether we are referring to the electric or to the magnetic current density. Therefore the following equations hold:

$$\nabla \cdot \mathbf{E} = \frac{\varrho_e}{\varepsilon_0}, \qquad -\nabla \times \mathbf{E} = \mathbf{J}_m + i\omega\mu_0\mathbf{H} \tag{2.25}$$

$$\begin{aligned}\mathbf{E}(\mathbf{r}) = &- i\omega\mu_0 \int_{\Omega_e} \mathbf{J}_e(\mathbf{r}')G(\mathbf{r},\mathbf{r}')d\mathbf{r}' \\ &- \frac{\nabla}{\varepsilon_0}\left[\int_{\Gamma_e} \varsigma_e(\mathbf{r}')G(\mathbf{r},\mathbf{r}')d\Gamma' + \int_{\Omega_e} \varrho_e(\mathbf{r}')G(\mathbf{r},\mathbf{r}')d\mathbf{r}'\right] \\ &- \frac{\nabla}{\varepsilon_0} \times \int_{\Omega_m} \mathbf{J}_m(\mathbf{r}')G(\mathbf{r},\mathbf{r}')d\mathbf{r}'. \end{aligned} \tag{2.26}$$

At the same time, we need to introduce a corresponding *Magnetic Field Integral Equation*, or briefly MFIE, which can be formulated in an analogous way to the EFIE. The final result is:

$$\begin{aligned}\mathbf{H}(\mathbf{r}) = &- i\omega\varepsilon_0 \int_{\Omega_m} \mathbf{J}_m(\mathbf{r}')G(\mathbf{r},\mathbf{r}')d\mathbf{r}' \\ &- \frac{\nabla}{\mu_0}\left[\int_{\Gamma_m} \varsigma_m(\mathbf{r}')G(\mathbf{r},\mathbf{r}')d\Gamma' + \int_{\Omega_m} \varrho_m(\mathbf{r}')G(\mathbf{r},\mathbf{r}')d\mathbf{r}'\right] \\ &- \frac{\nabla}{\mu_0} \times \int_{\Omega_e} \mathbf{J}_e(\mathbf{r}')G(\mathbf{r},\mathbf{r}')d\mathbf{r}'. \end{aligned} \tag{2.27}$$

In summary, in this section a brief introduction concerning the mathematical foundations of the Integral Equation (IE) approach was given. The expressions for the electric field and the magnetic field integral equations, EFIE and MFIE, are reported at the end of the section. EFIE and MFIE usually are the starting point for the analysis of the electromagnetic problem in $\Omega \subset \mathbf{R}^3$ [2], however, the analytical solution of the fields is unfeasible in the majority of situations, thus computer-aided engineering (CAE) tools are required.

2.2 Discretization of integral equations

The analysis is then moved to the search of a solution for the described problem. As very efficient and general solver for partial differential equation or integral equation problem, Galerkin's testing method is usually applied. Such a procedure consists of choosing two different functions: the first one, called *basis function*, is the one that should approximate the exact solution of the problem so that Galerkin's method is based on minimizing the error between them. The second is the *testing function* which, once applied to the analyzed equation, should provide an orthogonality condition with the basis functions, i.e. the inner product between the differential or integral equation and the testing function must be zero. Each function belongs to a suitable vectorial space which must be a priori defined. After both the basis and the testing function are properly identified, a new formulation in terms of the basis and testing function for the examined problem should be developed. Finally, a numerical approach, such as the discretization for the finite element method or the numeric integration, must be applied to solve the outcoming equation. About such discretization, it can be shown - and it will be assumed in the following - that there exists an empirical law which holds in the case of electromagnetic scattering processes and which relates the dimension of

the mesh h and the wavelength λ as follows:

$$\max h < \lambda/5 \tag{2.28}$$

The Galerkin method specifically applied to electromagnetic scattering problems is discussed in detail in many articles such as [3, 4]. To quickly summarize these concepts, we have to introduce the *electric field integral operator* (EIFO) and the *magnetic field* one (MFIO):

$$\boldsymbol{\mathcal{L}}(\mathbf{f})(\mathbf{r}) = ik\boldsymbol{\mathcal{S}}(\mathbf{f})(\mathbf{r}) - \frac{1}{ik}\nabla\nabla\cdot\boldsymbol{\mathcal{S}}(\mathbf{f})(\mathbf{r}) \tag{2.29}$$

$$\mathcal{K}(\mathbf{f})(\mathbf{r}) = \nabla\times\boldsymbol{\mathcal{S}}(\mathbf{f})(\mathbf{r}) \tag{2.30}$$

where S represents the surface of the domain over which we are acting and

$$\boldsymbol{\mathcal{S}}(\mathbf{f})(\mathbf{r}) = \int_S d\mathbf{r}' G(\mathbf{r},\mathbf{r}')\mathbf{f}(\mathbf{r}') \tag{2.31}$$

This way the integral equations we are looking for can be expressed in terms of the scattered tangential electric field and of the scattered surface current, which are respectively defined over S as a function of the surface electric current $\mathbf{j}$:

$$\mathbf{e}^s(\mathbf{j}) = \pi_\tau(\boldsymbol{\mathcal{L}}(\mathbf{j})) \tag{2.32}$$

$$\mathbf{j}^s(\mathbf{j}) = \frac{1}{2}\boldsymbol{\Lambda} + \gamma_\tau(\boldsymbol{\mathcal{K}}(\mathbf{j})) \tag{2.33}$$

where $\gamma_\tau(\mathbf{u}) = \hat{n}\times\mathbf{u}|_S$ is the twisted tangential trace operator and $\pi_\tau(\mathbf{u}) = \hat{n}\times(\mathbf{u}\times\hat{n})|_S = \gamma_\tau(\mathbf{u})\times\hat{n}$ is the tangential trace operator. Moreover two equations involving the incident electric ($\mathbf{E}_{inc}$) and magnetic field ($\mathbf{H}_{inc}$) on S should be introduced:

$$\mathbf{j}_{inc} = \eta_0\gamma_\tau(\mathbf{H}_{inc}) \tag{2.34}$$

$$\mathbf{e}_{inc} = \pi_\tau(\mathbf{E}_{inc}) \tag{2.35}$$

Therefore specific formulations for the EFIE and the MFIE can be obtained by coupling (2.32) and (2.33) with (2.35) and (2.34) and have validity over S:

$$\mathbf{e} = \mathbf{e}_{inc} + \mathbf{e}_s(\mathbf{j}) = 0 \tag{2.36}$$

$$\mathbf{j} = \mathbf{j}_{inc} + \mathbf{j}_s(\mathbf{j}) \tag{2.37}$$

The second step for the application of the Galerkin method (also known as weak formulation) involves the discretization of the domain we are considering into non-overlapping elements S_i such that $S = S_1\cup S_2,\ldots,\cup S_N$. Such decomposition allows to find an approximation of the unknown current value $\tilde{\mathbf{j}}$ as a function of the current over each

sub-element S_m, $m \in \{1, \dots, N\}$

$$\tilde{\mathbf{j}} = \bigoplus_{m=1}^{N} \mathbf{j}_m(\mathbf{r}) \tag{2.38}$$

The trial function is chosen from the $\mathbf{L}^2(S)$ space so that they are defined with elementwise compact support and it is possible to adopt such trial function to best approximate the current locally. Specific considerations about the basis and testing functions for the integral equations object of the thesis are discussed later. For the moment we choose as an example vector polynomials so that we get local trial functions $\mathbf{\Lambda}_m$ which are continuous inside the element S_m and which are allowed to be discontinuous across element boundaries. Summarizing, we can define the basis function over m as $\Phi_m = \text{span}_i\{\mathbf{\Lambda}_i^{m,p}\}$ where p is the degree of the polynomial, the local approximation for the current is formulated as:

$$\mathbf{j}_m(\mathbf{r}) = \sum_i a_{m,i} \mathbf{\Lambda}_i^{m,p}(\mathbf{r}) \tag{2.39}$$

Thus the scattered electric field must satisfy the following EFIE formulation:

$$\mathbf{e}_{inc,m} = -\sum_{n=1}^{N} \pi_\tau(\boldsymbol{\mathcal{L}}(\mathbf{j_n}, S_n)) \qquad \text{on } S_m \tag{2.40}$$

and we can estimate the error committed in such approximation by evaluating the surface residual which can be also interpreted as the tangential error electric field:

$$\mathcal{R}_m^{(1)} = \mathbf{e}_{inc,m} + \sum_{n=1}^{N} \pi_\tau(\boldsymbol{\mathcal{L}}(\mathbf{j_n}, S_n)) \qquad \text{on } S_m, \tag{2.41}$$

where the index (1) suggests that we are dealing with the first iteration of the process. If we choose the same function space adopted above also for expanding the *testing* function, i.e. $\mathbf{\Lambda}'_m \in \Phi_m$, the outcoming Galerkin formulation assumes form:

$$\left\langle \mathbf{\Lambda}'_m, \mathcal{R}_m^{(1)} \right\rangle_{S_m} = \left\langle \mathbf{\Lambda}'_m, \mathbf{e}_{inc,m} \right\rangle_{S_m} + \left\langle \mathbf{\Lambda}'_m, \sum_{n=1}^{N} \pi_\tau(\boldsymbol{\mathcal{L}}(\mathbf{j_n}, S_n)) \right\rangle_{S_m}, \tag{2.42}$$

with the surface integral term defined by the scalar product for vector spaces as:

$$\left\langle \mathbf{\Lambda}', \mathbf{u} \right\rangle_{S_m} = \int_{S_m} d\mathbf{r} \mathbf{\Lambda}' \cdot \mathbf{u}. \tag{2.43}$$

Finally it is possible to further expand (2.42) thanks to EIFO (2.29) getting:

$$\begin{aligned}
\left\langle \boldsymbol{\Lambda}'_m, \mathcal{R}_m^{(1)} \right\rangle_{S_m} &= \left\langle \boldsymbol{\Lambda}'_m, \mathbf{e}_{inc,m} \right\rangle_{S_m} + \left\langle \boldsymbol{\Lambda}'_m, \sum_{n=1}^{N} \pi_\tau(\boldsymbol{\mathcal{L}}(\mathbf{j_n}, S_n)) \right\rangle_{S_m} \\
&= \left\langle \boldsymbol{\Lambda}'_m, \mathbf{e}_{inc,m} \right\rangle_{S_m} + ik_0 \left\langle \boldsymbol{\Lambda}'_m, \sum_{n=1}^{N} \pi_\tau(\boldsymbol{\mathcal{S}}(\mathbf{j_n}, S_n)) \right\rangle_{S_m} \\
&- \frac{1}{ik_0} \left\langle \boldsymbol{\Lambda}'_m, \sum_{n=1}^{N} \pi_\tau(\nabla\nabla \cdot \boldsymbol{\mathcal{S}}(\mathbf{j_n}, S_n)) \right\rangle_{S_m} \\
&= \left\langle \boldsymbol{\Lambda}'_m, \mathbf{e}_{inc,m} \right\rangle_{S_m} + ik_0 \sum_{n=1}^{N} \left\langle \boldsymbol{\Lambda}'_m, \pi_\tau(\boldsymbol{\mathcal{S}}(\mathbf{j_n}, S_n)) \right\rangle_{S_m} \\
&- \frac{1}{ik_0} \sum_{n=1}^{N} \left\langle \boldsymbol{\Lambda}'_m, \pi_\tau(\nabla\nabla \cdot \boldsymbol{\mathcal{S}}(\mathbf{j_n}, S_n)) \right\rangle_{S_m} . \qquad (2.44)
\end{aligned}$$

The result presents issues related to the presence of hyper-singular terms which should be properly discussed. A solution proposed in [3] consists in applying Green's identity aiming to reduce the order of the singularity. However, since the objective of this discussion is to present an example of the application of the Galerkin method to EFIE, such proceed is not reported here.

The same idea at the base of the Galerkin method applied and the same procedure discussed for EFIE can be similarly extended also to the MFIE in order to extract an analogous result.

Coming back to the general formulation of integral equation problems, the matricial version of the electromagnetic scattering problem we are describing arises exactly from the application of Galerkin's method to both the augmented formulations. The basis functions that are adopted to apply this method should verify some important properties in order not to generate approximation problems when the numerical approach is applied. Specifically, a divergence-conforming Rao-Wilton-Glisson (RWG) is needed as both a test and basis function, otherwise, fictitious line charges for both the electric and magnetic current cases could be generated. Such basis functions are particularly suitable for analyzing numerical problems that exploit elements having small dimensions for the discretization of the domain. On the other hand, when the *Method of Moments* (MoM) is coupled with Galerkin's one to look at magnetic and electric inducted currents, these basis functions could generate double integrals presenting singularities which have to be appropriately treated.

The matricial analysis of the general problem is presented in many different papers with a variety of notations, involving [5, 6, 7]. Since we want to briefly describe the main points of such analysis, a unique notation is here reported to uniform all the considerations. In particular, two formulations are discussed here, each treating one specific situation of electromagnetic problems. The first and simplest case regards *Perfect Electric Conductors* (PEC), i.e. no mutual influence of the magnetic field on

the electric one and vice versa is considered. Under this condition, the augmented version of the EFIE (AEFIE), i.e. the EFIE coupled with the continuity equation of the current density, is also needed to avoid *low-frequency breakdowns* (LFB) problems that can arise because of the unbalance of the operators inside the simple EFIE. From here on we consider a sort of simplified version of the AEFIE applied to the SIE. In this specific case such formulation essentially differs from (2.26) for the surficial term, since when planar mesh is performed it completely loses its meaning. This way the AEFIE we are talking about states:

$$-\frac{\mathbf{E}}{\eta_0} = \mu_r \int_{S'_e} d\mathbf{r}' \mathbf{J}_e(\mathbf{r}') G(\mathbf{r}, \mathbf{r}') \cdot + \varepsilon_0^{-1} \int_{S'_e} d\mathbf{r}' \varrho_e(\mathbf{r}') \nabla G(\mathbf{r}, \mathbf{r}'), \tag{2.45}$$

and the continuity equation for the current is given by (2.20) described above. Before proceeding, it is necessary to briefly mention the fact that the basis and the testing functions should be different to avoid convergence issues under specific conditions; in our case, they are assumed to be coincident for simplicity of analysis since the error committed is indeed small. A more in-depth analysis concerning divergence-conforming functions which suit very well for solving this problem is presented below.

Now, adopting the Galerkin method and the RWG functions $\mathbf{\Lambda}$ for both the basis and the testing ones, defining the quantities $k_0 = \omega/c_0$ (c_0 is the speed of light in vacuum $c_0 = 1/(\varepsilon_0 \mu_0)$) and q the pulse basis function

$$q_i(\mathbf{r}) = \begin{cases} \frac{1}{A_i} & \text{if } \mathbf{r} \in S_i \\ 0 & \text{otherwise} \end{cases}, \tag{2.46}$$

the matrix-block version of the problem can be expressed as:

$$\begin{bmatrix} \mathbf{L} & \mathbf{D}^T \cdot \mathbf{P} \\ \mathbf{D} & k_0^2 \mathbf{I} \end{bmatrix} \cdot \begin{bmatrix} ik_0 \mathbf{j} \\ c_0 \varrho_e \end{bmatrix} = \begin{bmatrix} -\eta^{-1} \mathbf{b}_e \\ 0 \end{bmatrix}, \tag{2.47}$$

where $\mathbf{I}$ is the identity matrix, $\mathbf{D}$ is the incidence matrix defined as:

$$[\mathbf{D}]_{mn} = \begin{cases} 0 & \text{if patch } m \text{ does not belong to RWG } n \\ 1 & \text{if patch } m \text{ is the positive part of RWG } n \\ -1 & \text{if patch } m \text{ is the negative part of RWG } n \end{cases} \tag{2.48}$$

Equation (2.48) comes out from the application of the *method of cells* for the discretization of the domain in the specific case of RWG functions applied to surficial electromagnetic integral or finite element problems. This process is based on the subdivision into cells of the surface so that the distribution of the current density inside each cell is much easier to analyze through the RWG basis function itself. Moreover, the method of cells is very useful for dealing with complex geometries since it simplifies a lot the geometry of the scattering surface. The method of cells is described in detail

in [8], where it is also clear that the sparse incidence matrix $\mathbf{D}$ comes as the discrete counterpart of the divergence operator.

Finally, the remaining blocks are formulated as follows:

$$[\mathbf{L}]_{mn} = \mu_r \int_S d\mathbf{r} \mathbf{\Lambda}_m(\mathbf{r}) \cdot \int_{S'} d\mathbf{r}' G(\mathbf{r}, \mathbf{r}') \mathbf{\Lambda}_n(\mathbf{r}'), \tag{2.49}$$

$$[\mathbf{P}]_{mn} = \varepsilon_r^{-1} \int_S d\mathbf{r} p_m(\mathbf{r}) \cdot \int_{S'} d\mathbf{r}' G(\mathbf{r}, \mathbf{r}') p_n(\mathbf{r}'), \tag{2.50}$$

$$\mathbf{b}_m = \int_S d\mathbf{r} \mathbf{\Lambda}_m(\mathbf{r}) \cdot \mathbf{E}_{inc}(\mathbf{r}). \tag{2.51}$$

At very low frequencies, charge neutrality still causes rank deficiency for the above formulation. It is possible to present such an issue by noticing that inside the matricial formulation, the vector of length p is the null space of the matrix $\mathbf{D}^T$ and for multiple object problems the dimension of the null space is equal to the number of disconnected objects. This way it is possible to define a normalized vector $\mathbf{a} \in \mathbb{R}^{(e+p)\times 1}$ such that the first e elements are zeros and the last p are $1/\sqrt{p}$:

$$\mathbf{a} = \frac{1}{\sqrt{p}} (0 \ \ldots \ 0 \ 1 \ \ldots \ 1)^T. \tag{2.52}$$

It can also be proved that such $\mathbf{a}$ is an eigenvector having very small eigenvalues k_0^2:

$$\mathbf{A}^T \cdot \mathbf{a} = k_0^2 \mathbf{a}, \tag{2.53}$$

and in the DC case $\mathbf{a}$ becomes the null space of $\mathbf{A}^T$. Moreover, because of the charge neutrality, the smallest eigenvalue makes the condition number of the matrix very large. One possible way to cancel the singularity that arises, in this case, is the deflation method described in [9, 10]. A simpler one which is also taken into account here is based on the reduction of the number of unknowns by the direct application of the charge neutrality into (2.47). In particular, we assume that there are t disconnected objects for a problem so that there are also t spanning trees, each containing p_i triangular patches such that $\sum_{i=1}^{t} p_i = p$. The concept of charge neutrality can be expressed by the fact that the total charge of each spanning tree is zero. To enforce this condition we drop one charge for each spanning tree and we reduce the vector of charge to $\varrho_r \in \mathbb{C}^{(p-t)\times 1}$. A convenient way to express this new vector is to introduce two highly sparse matrices, $\mathbf{F} \in \mathbb{R}^{(p-t)\times p}$ which maps the full vector to the reduced one and the inverse one $\mathbf{B} \in \mathbb{R}^{p\times(p-t)}$:

$$\varrho_r = \mathbf{F} \cdot \varrho_e, \tag{2.54}$$

$$\varrho_e = \mathbf{B} \cdot \varrho_r. \tag{2.55}$$

This way the final form of the matricial problem is expressed by:

$$\begin{bmatrix} \mathbf{L} & \mathbf{D}^T \cdot \mathbf{P} \cdot \mathbf{B} \\ \mathbf{F} \cdot \mathbf{D} & k_0^2 \mathbf{I}_r \end{bmatrix} \cdot \begin{bmatrix} ik_0 \mathbf{j} \\ c_0 \varrho_r \end{bmatrix} = \begin{bmatrix} -\eta^{-1} \mathbf{b}_r \\ 0 \end{bmatrix}, \tag{2.56}$$

where the identity matrix $\mathbf{I}_r$ has now dimensions $(p-t) \times (p-t)$. This formulation is also very important since it ensures full rank down to DC and it will be adopted for the computations regarding the Perfect Electric Conductor (PEC) sphere in the following chapters.

The second condition analyzed in this thesis work involves dielectric media. In this specific situation, the solution for both the problems formulated concerning the external region - where we assume the losses are very small or completely negligible - and the internal one have to be computed. In particular, it is possible to describe the problem in the external region by adopting the EFIE formulation, while the internal problem for the conductor is represented by the MFIE formulation:

$$\hat{\boldsymbol{n}} \times [\mathcal{L}^S_{ext}(\mathbf{J}_{e,S}) + \mathcal{K}^S_{ext}(\mathbf{J}_{m,S})] = -\hat{\boldsymbol{n}} \times \mathbf{E}_{ext} \qquad \mathbf{r} \in S, \tag{2.57}$$

$$\hat{\boldsymbol{n}} \times [\mathcal{L}^S_{int}(\mathbf{J}_{e,S}) + \mathcal{K}^S_{int}(\mathbf{J}_{m,S})] = 0 \qquad \mathbf{r} \in S, \tag{2.58}$$

where S represents the surface of the conductor, $\hat{\boldsymbol{n}}$ is it's outer normal, and $\mathbf{J}_{e,S}$ and $\mathbf{J}_{m,S}$ are respectively the equivalent electric and magnetic current densities which are defined by the equivalence principle for integral equations in electromagnetic scattering problems. Finally, the formulation for $\mathcal{L}$ and $\mathcal{K}$ considered here is slightly different from the one described by (2.29) and (2.30), since we want to adopt a notation which is consistent for both the internal and the external region:

$$\mathcal{L}(\mathbf{f})(\mathbf{r}) = t_j \left[\int_S d\mathbf{r}' G_j \cdot \mathbf{f}(\mathbf{r}') + \frac{1}{k_j^2} \int_S d\mathbf{r}' \nabla G_j(\mathbf{r}, \mathbf{r}') \nabla' \cdot \mathbf{f}(\mathbf{r}') \right], \tag{2.59}$$

$$\mathcal{K}(\mathbf{f})(\mathbf{r}) = (-1)^{j+1} \frac{1}{2} \hat{\boldsymbol{n}} \times \mathbf{f}(\mathbf{r}') + \oint_S d\mathbf{r}' \mathbf{f}(\mathbf{r}') \times \nabla G_j(\mathbf{r}, \mathbf{r}'), \tag{2.60}$$

where $\mathbf{f}(\mathbf{r}')$ is either $\mathbf{J}_{e,S}(\mathbf{r}')$ with $t_j = i\omega\mu_j$ or $\mathbf{J}_{m,S}(\mathbf{r}')$ with $t_j = i\omega\varepsilon_j$ and $j = 0$ stays for the external region while $j = 1$ identifies the internal one. In particular, $\mathcal{K}$ matrix presents ill-conditioning problems if non-suitable test and basis functions are chosen, so a proper discussion will be introduced later. Finally, coming back to the AEFIE formulation in the dielectric case, it's possible to expand both the electric ($\mathbf{J}$) and magnetic current ($\mathbf{M}$) by the respective basis functions $\mathbf{\Lambda}^J$ e $\mathbf{\Lambda}^M$ and testing the equation with the function $\mathbf{T}$.

Adopting the *extinction theorem* and again the augmentation technique to minimize

the LFB phenomenon, the final matrix expression of the problem becomes:

$$\begin{bmatrix} \mathbf{L}^v_{ext} & \mathbf{D}^T \cdot \mathbf{P} & \eta^{-1}\mathbf{K}_{ext} & 0 \\ \mathbf{D} & k_0^2\mathbf{I} & 0 & 0 \\ \eta_0^{-1}\mathbf{K}_{int} & 0 & \mathbf{L}^v_{int} & \mathbf{D}^T \cdot \mathbf{P}_{int} \\ 0 & 0 & \mathbf{D} & k_0^2\mathbf{I} \end{bmatrix} \cdot \begin{bmatrix} ik_0\mathbf{j}_{e,S} \\ c_0\varrho_e \\ ik_0\mathbf{j}_{m,S} \\ c_0\varrho_m \end{bmatrix} = \begin{bmatrix} \eta_0^{-1}\mathbf{b} \\ 0 \\ 0 \\ 0 \end{bmatrix}. \tag{2.61}$$

The blocks adopted in this formulation are defined in analogy with the aforementioned (2.49), (2.50) and (2.51) apart for the constants in front of the integrals. In fact when the external region is considered, $j = 0$ and $\mu_r = \mu_j/\mu_0 = 1$, $\varepsilon_r = \varepsilon_0/\varepsilon_j = 1$, while when the internal region is taken into account we have $j = 1$ and then $mu_r = \mu_1\mu_0$, $\varepsilon_r = \varepsilon_0/\varepsilon_1$. Furthermore, the Green function should be identified with a subscript index, G_j, since k which appears at the exponent of the numerator now depends on which region is considered. Finally, the new blocks appearing in (2.61) are defined as:

$$[\mathbf{K}_j]_{mn} = \int_S d\mathbf{r}\mathbf{\Lambda}_m(\mathbf{r}) \cdot \oint_{S'} d\mathbf{r}' G_j(\mathbf{r}, \mathbf{r}') \times \mathbf{\Lambda}_n(\mathbf{r}'), \tag{2.62}$$

$$\mathbf{J}_m, S = \sum_{n=1}^{N} \mathbf{j}_{m,S_n}\mathbf{\Lambda}_n, \tag{2.63}$$

$$\varrho_m(\mathbf{r}) = \sum_{n=1}^{N} \varrho_{mn} q_n(\mathbf{r}'). \tag{2.64}$$

An alternative version of the matricial formulation above is adopted in [6, 11]. It states:

$$\begin{bmatrix} \mathbf{L}_{ext} & -\frac{1}{2}\hat{\boldsymbol{n}} \times \mathbf{I} + \mathbf{K}_{ext} & \mathbf{D}^T \cdot \mathbf{P}_{ext} \cdot \mathbf{B} \\ \mathbf{L}_{int} & \frac{1}{2}\hat{\boldsymbol{n}} \times \mathbf{I} + \mathbf{K}_{int} & \mathbf{D}^T \cdot \mathbf{P}_{int} \cdot \mathbf{B} \\ \mathbf{F} \cdot \mathbf{D} & 0 & k_0^2\mathbf{I} \end{bmatrix} \cdot \begin{bmatrix} ik_0\mathbf{j} \\ \eta_0^{-1}\mathbf{m} \\ c_0\rho_r \end{bmatrix} = \begin{bmatrix} -\eta_0^{-1}\mathbf{b} \\ 0 \\ 0 \end{bmatrix}, \tag{2.65}$$

where again

$$[\hat{\boldsymbol{n}} \times \mathbf{I}]_{mn} = \int_S d\mathbf{r}\mathbf{\Lambda}_m(\mathbf{r}) \cdot \left(\hat{\boldsymbol{n}}(\mathbf{r}) \times \mathbf{\Lambda}^M_n(\mathbf{r})\right). \tag{2.66}$$

However for this thesis work the formulation in (2.61) is considered in the following numerical analysis. Indeed (2.61) expresses a sort of symmetry between the electric field component and the magnetic field one so that it should be easier to be implemented.

In this work, the Rao-Wilton-Glisson (RWG) basis functions are used for the expansions of the surface current density. The RWG basis functions, firstly introduced in [12] are here briefly summarized by considering the two triangles illustrated in Fig. 2.1. Referring to these triangles, the RWG basis function associated with the shared edge is written as:

$$\mathbf{\Lambda}(\mathbf{r}') = \begin{cases} \frac{1}{2A^+}(\mathbf{r}' - \mathbf{q}^+) & \text{if } \mathbf{r}' \in S^+ \\ -\frac{1}{2A^-}(\mathbf{r}' - \mathbf{q}^-) & \text{if } \mathbf{r}' \in S^- \end{cases} \tag{2.67}$$

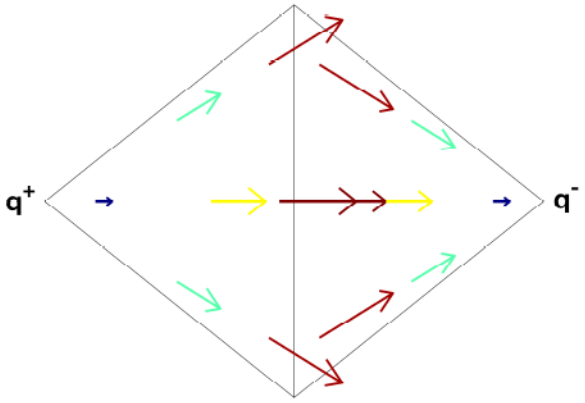

Figure 2.1: General behavior of Rao-Wilton-Glisson (RWG) basis functions

$$\nabla \cdot \mathbf{\Lambda}(\mathbf{r}') = p(\mathbf{r}') = \begin{cases} \frac{1}{A^+} & \text{if } \mathbf{r}' \in S^+ \\ -\frac{1}{A^-} & \text{if } \mathbf{r}' \in S^- \end{cases} \tag{2.68}$$

where the indices $\pm$ identify the sign of the charge over each of the two patches. It is important to note that usually, the trial and testing basis functions are defined in different spaces. Indeed, by using $\mathbf{\Lambda}$ both for the test and trial spaces, matrix $\mathcal{K}$ turns out to be poorly tested and ill-conditioned. Aiming to solve this issue, different testing functions can be used, for example, the $\mathbf{n}\times$ RWG, as highlighted in [13]. The div-conforming and quasi-curl conforming Buffa-Christiansen (BC) basis functions, similar to RWG's are usually adopted to improve the conditioning of the resulting matrices [14, 15, 16]. The BC's basis functions are defined on the barycentric refinement of the mesh, and their detailed construction can be found for example in [15]. Strictly speaking, the BC's basis functions are expressed as a linear combination of the div-conforming RWG's basis. A graphical example of the shape of the BC basis function is illustrated in Fig. 2.2.

Since the results presented in this thesis work are almost theoretical and since the numerical implementations described in the following can be easily extended to any basis function once it is properly defined, the RWG basis functions are adopted for both basis and testing functions for simplicity.

Concerning the solution of the problem in the dielectric case, for the external region the formulation is given by the first equation of the system (2.65) and can be simply solved thanks to the singularity subtraction method. For what concerns the internal one the discussion is slightly more complicated. We will see in the following chapters that the singularities cannot be treated with the singularity subtraction method so four different types of integrals involving the Green function will be introduced to simplify the analysis:

$$I_1 = \int_{S'} d\mathbf{r}' \frac{e^{ikR}}{R} \tag{2.69}$$

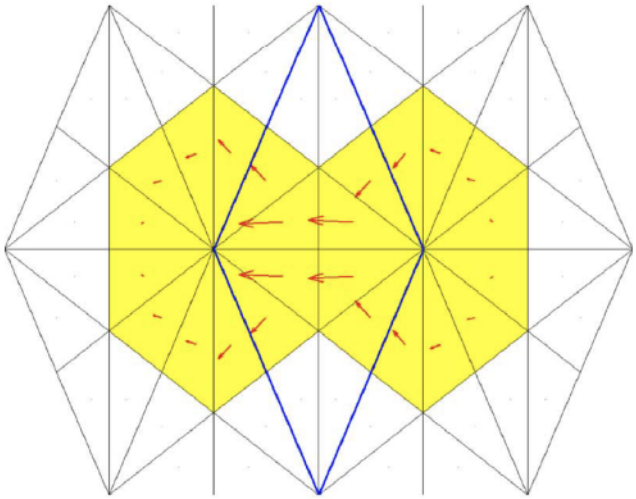

Figure 2.2: Graphical example of Buffa-Christiansen (BC) basis function. Figure taken from [15].

$$\mathbf{I}_2 = \int_{S'} d\mathbf{r}' \frac{e^{ikR}}{R}(\mathbf{r}' - \mathbf{q}) \tag{2.70}$$

$$\mathbf{I}_3 = \int_{S'} d\mathbf{r}' \nabla \left(\frac{e^{ikR}}{R}\right) \tag{2.71}$$

$$\mathbf{I}_4 = \int_{S'} d\mathbf{r}' \nabla \left(\frac{e^{ikR}}{R}\right) \times (\mathbf{r}' - \mathbf{q}) \tag{2.72}$$

Summarizing, this chapter is dedicated to the general theoretical introduction of the main tools we will adopt in next sections for the description of the SIE. In particular an overview of how the Surface Integral Method arises is given, starting from the general Maxwell's equations and applying the Galerkin method. The required divergence-conforming functions are properly described as well. Then, integral equations expressing both the electric and the magnetic fields are derived from the theoretical point of view, as well as their augmented version obtained from the coupling with continuity equations. As a result, the block-matrix formulation of the problem is obtained for both PEC elements and dielectric media.

Chapter 3

Evaluation of Singular Integrals in SIE

In the previous chapter the mathematical foundation of the Integral Equation Method (IEM) for the solution of electromagnetic problems, is given. The well-known Galerkin method allows for the translation of the continuous mathematical problem into a discrete system, for example, the one shown in (2.61), which can be solved numerically. As explained in the previous chapter, the matrices appearing in the system require the evaluation of double integrals, showing a singular behavior. As an example, the inductance matrix $\mathbf{L}$, whose elements are given in (2.49), requires the integration of the basis function $\mathbf{\Lambda}$ together with the Green's kernel (2.13). It is worth noting that such kinds of integrals do appear for every Integral Equation (IE) method, that is both for the Volume Integral Equation (VIE) approach and the Surface Integral Equation (SIE) method. To solve this issue sophisticated mathematical procedures are required especially when the dynamic part of the Green's kernel (2.13) cannot be neglected. Generally speaking, the mathematical procedures aim to evaluate the inner integrals of the form:

$$\int_\Omega G(\mathbf{r},\mathbf{r}')\mathbf{\Lambda} d\mathbf{r}', \quad \int_\Omega \nabla G(\mathbf{r},\mathbf{r}') \times \mathbf{\Lambda} d\mathbf{r}', \tag{3.1}$$

with analytical formulas [17], so that, the entries of the fully populated matrices $\mathbf{L}, \mathbf{P}$, and $\mathbf{K}$ can be constructed via a semi-analytical formula.

Summarizing, one of the most crucial issues that has to be solved when we try to build the matrices that compose the integral methods regards the singularity appearing inside both the static and the dynamic version of Green's function and the non-evaluability of the first derivative of eq (2.13). In the following sections, some approaches that try to analyze this question will be described, in the context of the Surface Integral Equation (SIE) method. Section 3.1 is dedicated to the approach proposed by Fabbri which looks for an analytical solution to the static version of the Green function while Section 3.2 and Section 3.3 discuss methods for the analysis of its dynamic version. Section 3.4 regards the theoretical description of an alternative fully numeric approach for getting the exact solution to the problem we are analyzing.

Finally Section 3.5 and Section 3.6 present the numerical results obtained from the application of all the considered methods.

3.1 Fabbri's analytical method for static Green's function

One of the first important methods that try to solve singularity issues inside a function of the form $1/R$ was introduced by Fabbri in 2008 [18]. This method is here described even if it concerns only a static version of the Green function, i.e.:

$$G_0(\mathbf{r},\mathbf{r}') = \frac{1}{4\pi R}, \qquad R = \|\mathbf{r}-\mathbf{r}'\| \tag{3.2}$$

Its validity is therefore limited to the only case of low frequencies and the analysis is reported only with a didactic scope since it will be adopted as a comparison tool to check the results obtained from the other approaches. This method is in general known as *Fabbri's method* from the name of its developer and it tries to find an analytical expression that allows to rewriting of the integral:

$$W_f(\mathbf{r}) = \int_{S_f} \frac{d\mathbf{r}'}{\|\mathbf{r}-\mathbf{r}'\|} \tag{3.3}$$

over a 2-dimensional triangular surface S_f, to not consider a singular formulation. The final expression which will be discussed is very important in fundamental integral evaluation. First, we should introduce the identity:

$$\frac{1}{\|\mathbf{r}-\mathbf{r}'\|} = \hat{n}_f \cdot \nabla' \times \left(\hat{n}_f \times \frac{\mathbf{r}'-\mathbf{r}}{\|\mathbf{r}'-\mathbf{r}\|}\right) - \frac{[(\mathbf{r}'-\mathbf{r})\cdot\hat{n}_f]^2}{\|\mathbf{r}'-\mathbf{r}\|^3} \tag{3.4}$$

where $\hat{n}_f$ is the value of the unit vector normal to S_f surface, $\mathbf{r}$ is the target point we are considering and $(\mathbf{r}'-\mathbf{r})\cdot\hat{n}_f$ can be considered constantly equal to $(\mathbf{r}_f-\mathbf{r})\cdot\hat{n}_f$ where $\mathbf{r}_f$ is an arbitrary point of the triangular surface. It's also necessary to define the version of W_f applied to an edge of the triangle:

$$w_e(\mathbf{r}) = \int_{l_e} \frac{d\mathbf{r}'}{\|\mathbf{r}-\mathbf{r}'\|} \tag{3.5}$$

Here l_e is the edge concerning which we are making the computations and $\mathbf{r}_{1,2}$ are the vertices of the e-th edge. The solution of such an integral is known from the literature [19]:

$$w_e(\mathbf{r}) = \ln \frac{\|\mathbf{r}_2-\mathbf{r}\| + \|\mathbf{r}_1-\mathbf{r}\| + \|\mathbf{r}_2-\mathbf{r}_1\|}{\|\mathbf{r}_2-\mathbf{r}\| + \|\mathbf{r}_1-\mathbf{r}\| - \|\mathbf{r}_2-\mathbf{r}_1\|} \tag{3.6}$$

Using the equations (3.6) and (3.4) inside (3.3) it's possible to obtain the final form of W_f:

$$W_f(\mathbf{r}) = \sum_{l_e \in \partial S_f} \hat{n}_f \times (\mathbf{r}_e-\mathbf{r})\cdot\mathbf{u}_e w_e(\mathbf{r}) - [(\mathbf{r}_f-\mathbf{r})\cdot\hat{n}_f]\Omega_f(\mathbf{r}) \tag{3.7}$$

where $\mathbf{r}_e$ is an arbitrary point on the e-th edge, $\mathbf{u}_e$ is the unit vector along the edge l_e and:

$$\Omega_f(\mathbf{r}) = 2\,\mathrm{atan}\left[\frac{(\mathbf{r}_1-\mathbf{r})\cdot(\mathbf{r}_2-\mathbf{r})\times(\mathbf{r}_3-\mathbf{r})}{D}\right], \tag{3.8}$$

$$\begin{aligned} D = &\|\mathbf{r}_1-\mathbf{r}\|\|\mathbf{r}_2-\mathbf{r}\|\|\mathbf{r}_3-\mathbf{r}\| \\ &+ \|\mathbf{r}_3-\mathbf{r}\|(\mathbf{r}_1-\mathbf{r})\cdot(\mathbf{r}_2-\mathbf{r}) \\ &+ \|\mathbf{r}_2-\mathbf{r}\|(\mathbf{r}_1-\mathbf{r})\cdot(\mathbf{r}_3-\mathbf{r}) \\ &+ \|\mathbf{r}_1-\mathbf{r}\|(\mathbf{r}_2-\mathbf{r})\cdot(\mathbf{r}_3-\mathbf{r}). \end{aligned} \tag{3.9}$$

3.2 Singularity subtraction method

From the chronological point of view, one of the first methods which tried to solve the presence of singularity inside the dynamic Green's function was the *Singularity Subtraction method* [13, 20, 21, 22, 23, 24]. Recalling the definition of (2.13), the method looks for, as the name itself explains, a way to approximate this function avoiding the denominator to disappear. One of the simplest and most famous approaches having these characteristics is the Taylor expansion, which was adopted to express the required function. More in detail, the exponential part was expanded using the Taylor series:

$$e^{ikR} = \sum_{q=0}^{\infty}\frac{(ikR)^q}{q!} = 1 + ikR - \frac{k^2R^2}{2} + \frac{ik^3R^3}{6} - \dots \tag{3.10}$$

so that the Green's function became:

$$G(\mathbf{r},\mathbf{r}') = \sum_{q=-1}^{\infty}\frac{(ik)^{q+1}R^q}{(q+1)!} = \frac{1}{4\pi}\left(\frac{1}{R} + ik - \frac{k^2R}{2} + \frac{ik^2R^2}{6} - \dots\right) \tag{3.11}$$

The main issue regarding such formulation involves odd terms which are the singular ones. Indeed, as introduced above, the first derivative of Green's function cannot be evaluated when $R = \|\mathbf{r}-\mathbf{r}'\| \to 0$. Luckily when the product kR is very small high powers having such a product at the exponent decreases very quickly and can be finally neglected, so that odd terms of the expansion are not needed to be computed analytically.

In conclusion, the singularity subtraction method is based on the subdivision of the Green's function expressed by eq.(3.12) into two terms: on one hand we have a smooth part G_s (3.13), on the other one the non-smooth functions are collected. If G_s, which coincides with the initial Green's function deprived of non-smooth terms, can be integrated straightforward, e.g., using the Gaussian quadrature rule, the remaining non-smooth terms must be evaluated analytically.

$$\int_S G(\mathbf{r},\mathbf{r}')\mathbf{F}(\mathbf{r}')d\mathbf{r}' = \int_S G_s(\mathbf{r},\mathbf{r}')\mathbf{F}(\mathbf{r}')d\mathbf{r}' + \frac{1}{4\pi}\int_S\frac{1}{R}\mathbf{F}(\mathbf{r}')d\mathbf{r}' - \frac{k^2}{8\pi}\int_S R\mathbf{F}(\mathbf{r}')d\mathbf{r}' \tag{3.12}$$

$$\int_S G_s(\mathbf{r},\mathbf{r}') = \frac{1}{4\pi}\int_S \left(\frac{e^{ikR}-1}{R}+\frac{k^2R}{2}\right)d\mathbf{r}' \tag{3.13}$$

3.3 Line integral method

The third crucial method for the analysis of singular integrals is the *Line Integral Method* [25]. It is based on the equations shown at the end of Chapter 2, which express the integrals obtained through RWG basis functions [26] and which are fundamental in the exstimation of the matrix components (2.69), (2.70), (2.71) and (2.72). The validity of such method can be shown by the evaluation of these integrals in both conditions of lossless and lossy medium through geometrical considerations. In particular, we should consider the projection of the source point on the target triangle, $\mathbf{r}_0$, and we have to divide the initial polygon in 3 sub-triangles whose edges are identified by two vertices of the triangle and by $\mathbf{r}_0$. Elements inside each sub-triangle that will be useful for later computations are stressed in figure 3.1. We have to pay attention also to the order in which the vertices of the sub-triangles are assumed: in fact it must be consistent and we assume e.g. to move clockwise.

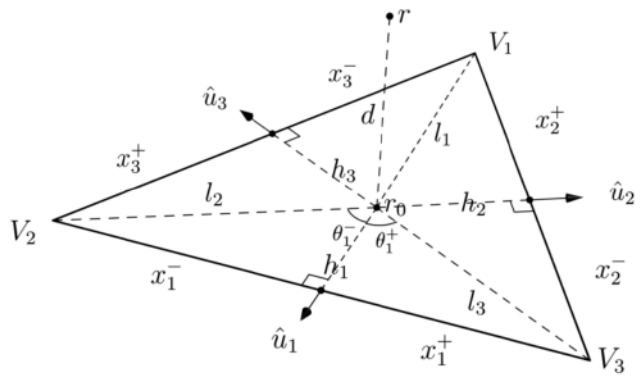

Figure 3.1: Sub-triangles identification and components denominations

The name of the method is indeed due to the fact that a surface integral is decoupled into three line integrals which are evaluated separately, thanks to this subdivision of the target triangle. We first focus on the integral I_1 which is the fundamental one. The integration over the triangular element is converted through a change of variables into a double integral over the vertex angle θ and $\rho = \mathbf{r}' - \mathbf{r}_0$. Notice also that from the definition of $R = \|\mathbf{r}-\mathbf{r}'\|$, we have that $R = \sqrt{\rho^2+d^2}$ and then $RdR = \rho d\rho$. Therefore the integral can be rewritten as:

$$I_1 = \sum_{i=1}^{3}\int_{\theta_i^-}^{\theta_i^+} d\theta \int_0^{\rho(\theta)} d\rho\rho\frac{e^{ikR}}{R} = \sum_{i=1}^{3}\int_{\theta_i^-}^{\theta_i^+} d\theta \int_0^{R(\theta)} dR\frac{e^{ikR}}{R} = \sum_{i=1}^{3}\int_{\theta_i^-}^{\theta_i^+} d\theta\frac{e^{ikR(\theta)}-e^{ikd}}{ik}$$
$$= \frac{1}{ik}\sum_{i=1}^{3}\int_{x_i^-}^{x_i^+} dx\frac{h_i}{h_i^2+x^2}\left(e^{ik\sqrt{d^2+h_i^2+x^2}}-e^{ikd}\right) \tag{3.14}$$

Moving on, we can define some important vectorial quantities that will be useful in the

evaluation of the remaining main integrals:

$$\mathbf{I}_\beta = \int_{S'} d\mathbf{r}' \frac{e^{ikR}}{R} \rho(\mathbf{r}') \tag{3.15}$$

$$\mathbf{I}_\perp = \mathbf{d} \int_{S'} d\mathbf{r}' \frac{ikR - 1}{R^3} e^{ikR} \tag{3.16}$$

$$\mathbf{I}_\parallel = \int_{S'} d\mathbf{r}' \frac{ikR - 1}{R^3} e^{ikR} \rho(\mathbf{r}') \tag{3.17}$$

This way, the final form of the the equations (2.70), (2.71) and (2.72) respectively become:

$$\mathbf{I}_2 = (\mathbf{r} - \mathbf{q}_0) I_1 + \mathbf{I}_\beta \tag{3.18}$$

$$\mathbf{I}_3 = \mathbf{I}_\perp - \mathbf{I}_\parallel \tag{3.19}$$

$$\mathbf{I}_4 = \mathbf{I}_\perp \times (\mathbf{r}_0 - \mathbf{q}) + (\mathbf{r} - \mathbf{q}) \times \mathbf{I}_\parallel \tag{3.20}$$

To make $\mathbf{I}_\beta$ and $\mathbf{I}_\parallel$ easier to be evaluated we have to apply a further subdivision of the three sub-triangles by using the arc of radius h_i as in figure 3.2. The reasoning we

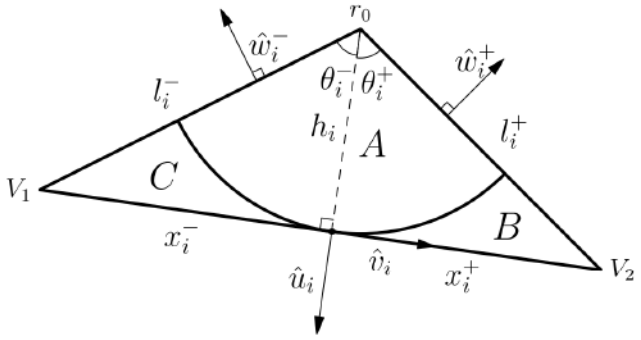

Figure 3.2: Sub-triangle subdivision into A,B,C areas

have to apply can be extended to any function $f(R)$ which has to be integrated over the three regions. Concerning a generic function, the results here state:

$$\int_A d\mathbf{r}' f(R) \rho(\mathbf{r}') = \int_0^{h_i} \rho^2 d\rho f(\rho) \begin{pmatrix} \sin\theta_i^+ - \sin\theta_i^- \\ \cos\theta_i^- - \cos\theta_i^+ \end{pmatrix}, \tag{3.21}$$

$$\int_B d\mathbf{r}' f(R) \rho(\mathbf{r}') = \int_{h_i}^{l^+} \rho d\rho f(\rho) \begin{pmatrix} \rho \sin\theta_i^+ - s_i^+ \sqrt{\rho^2 - h_i^2} \\ h_i - \rho\cos\theta_i^+ \end{pmatrix}, \tag{3.22}$$

$$\int_C d\mathbf{r}' f(R) \rho(\mathbf{r}') = \int_{h_i}^{l^-} \rho d\rho f(\rho) \begin{pmatrix} s_i^- \sqrt{\rho^2 - h_i^2} - \rho \sin\theta_i^- \\ \rho\cos\theta_i^- - h_i \end{pmatrix}, \tag{3.23}$$

where we have defined:

$$\begin{pmatrix} a \\ b \end{pmatrix} = a\hat{u}_i + b\hat{v}_i \quad \text{and} \quad s_i^\pm = \frac{\theta_i^\pm}{|\theta_i^\pm|} \tag{3.24}$$

We can apply some simplifications noticing that some terms have the same value and opposite sign when evaluated on the common edge of two sub-triangles. This way the surviving can be summarized as:

$$\sum_{i=1,h_i\neq 0}^{3}\begin{pmatrix}\left(-s_i^+\int_{h_i}^{l_i^+}-s_i^+\int_{h_i}^{l_i^-}\right)\rho d\rho f(R)\sqrt{\rho^2-h_i^2}\\ h_i\left(\int_{h_i}^{l_i^+}-\int_{h_i}^{l_i^-}\right)\rho d\rho f(R)\end{pmatrix}. \tag{3.25}$$

The last remaining step requires to substitute the functions $f(R)=e^{ikR}/R$ and $f(R)=(ikR-1)e^{ikR}/R^3$ inside the general formulation. This way, defining $R_i^{\pm}=\sqrt{d^2+(l_i^{\pm})^2}$, we end up with:

$$\mathbf{I}_\beta=\sum_{i=1,h_i\neq 0}^{3}\begin{pmatrix}-\int_{x_i^-}^{x_i^+}\frac{x^2}{R(x)}e^{ikR(x)}dx\\ \frac{h_i}{ik}(e^{ikR_i^+}-e^{ikR_i^-})\end{pmatrix}, \tag{3.26}$$

$$\mathbf{I}_\parallel=\sum_{i=1,h_i\neq 0}^{3}\begin{pmatrix}-\int_{x_i^-}^{x_i^+}\frac{x^2}{R^3(x)}(ikR(x)-1)e^{ikR(x)}dx\\ \frac{h_i}{ik}\left(\frac{e^{ikR_i^+}}{R_i^+}-\frac{e^{ikR_i^-}}{R_i^-}\right)\end{pmatrix}, \tag{3.27}$$

In conclusion, concerning $\mathbf{I}_\perp$, it can be modified in analogy with the considerations exposed for I_1. This way it finally provides:

$$\mathbf{I}_\perp=-\sum_{i=1,h_i\neq 0}^{3}\int_{x_i^-}^{x_i^+}dx\frac{h_i}{h_i^2+x^2}\left(\frac{e^{ikd}}{d}-\frac{e^{ik\sqrt{d^2+h_i^2+x^2}}}{\sqrt{d^2+h_i^2+x^2}}\right). \tag{3.28}$$

Unfortunately the line integral method, and in particular I_1 and $\mathbf{I}_\perp$, shows a singularity when $h_i\to 0$, and so both the integrand functions are not smooth. Moreover, the behavior of such a method is particularly similar to the exact value in the case of lossy media, losing its effectiveness in the lossless case. To solve these remaining issues, a change of variable was applied to the initial function. The new arising method is therefore called *Modified Integral method* [11].

Such method is bases its formulation on the substitution of the function $R(x)=\sqrt{d^2+h_i^2+x^2}$ with an alternative version:

$$R(\theta)=\sqrt{d^2+\frac{h_i^2}{\cos^2\theta}}, \tag{3.29}$$

changing the previous equations into two new statements:

$$I_1=\sum_{i=1,h_i\neq 0}^{3}\int_{\theta_i^-}^{\theta_i^+}\frac{d\theta}{ik}(e^{ikR(\theta)}-e^{ikd}), \tag{3.30}$$

$$\mathbf{I}_\perp=\hat{d}\sum_{i=1,h_i\neq 0}^{3}\int_{\theta_i^-}^{\theta_i^+}d\theta\left(\frac{d}{R(\theta)}e^{ikR(\theta)}-e^{ikd}\right). \tag{3.31}$$

An important question to be discussed arises when the projection of the target point is located in a critical position, i.e. outside of the total triangle. To analyze this situation we have to figure out the fact that when we integrate a constant function, e.g. $f(\theta) = 1$, over the sum of the sub-triangles the final result is the total area of the triangle if the point is inside the triangle, while it provides nulla value if the point is outside of the triangle. In particular, such value can be obtained if we think to reverse the order in which we take the vertices of the sub-triangles which lay completely outside of the bigger one, or again it coincides with swiping the sign of $\theta_i^+ > 0$ and $\theta_i^- < 0$.

For the sake of completeness, a quick analysis of the factor e^{ikd} of the integrand function between θ_i^- and θ_i^+ is also reported. This function is constant concerning θ, hence it can be brought outside of the integral. Moreover, we can notice that if $h_i \to 0$ the integral becomes null. Thus if we define:

$$I_0 = \sum_{i=1, h_i \neq 0}^{3} \int_{\theta_i^-}^{\theta_i^+} d\theta e^{ikd}, \tag{3.32}$$

- if $\mathbf{r}_0$ is inside the triangle, $I_0 = 2\pi e^{ikd}$
- if $\mathbf{r}_0$ is on an edge of the triangle, $I_0 = \pi e^{ikd}$
- if $\mathbf{r}_0$ is outside the triangle, $I_0 = 0$

However for the computations reported in the following sections the equations (3.30) and (3.31) were adopted. These formulations are generally valid and they evaluate the situation also for ($\mathbf{r}_0$) coincident with a vertex of the triangle, whose value in terms of vertex angles cannot be apriori defined.

Last, a fundamental situation that needs to be discussed carefully regards the target point lying on the test triangle, i.e. the situation when $d = 0$. For such condition both the first term of (3.30) and (3.15) provide null contribution, so that I_1 and $\mathbf{I}_2$ are directly proportional to I_0:

$$I_1 = -\frac{1}{ik} I_0 \qquad \text{and} \qquad \mathbf{I}_2 = -\frac{1}{ik} I_0 (\mathbf{r}_0 - \mathbf{q}) \tag{3.33}$$

We can also make the same considerations for the components generating $\mathbf{I}_3$ and $\mathbf{I}_4$: $\mathbf{I}_\parallel$ completely vanishes, as well as the part of $\mathbf{I}_\perp$ linearly dependent on d inside equation (3.31). Thus the only contribution to the integrals $\mathbf{I}_3$ and $\mathbf{I}_4$ becomes proportional to I_0 and it follows the formulas:

$$\mathbf{I}_3 = \mp I_0 \hat{n} \qquad \text{and} \qquad \mathbf{I}_4 = \mp I_0 \hat{n} \times (\mathbf{r}_0 - \mathbf{q}), \tag{3.34}$$

where the negative sign is chosen when $\mathbf{r}$ resides on the surface of the triangle where $\hat{n}$ points to. We can also notice that from these results $\mathbf{I}_3$ is directed along the outer normal to the surface of the triangle, while, noticing that $(\mathbf{r}_0 - \mathbf{q})$ lays on the plane of the triangle, $\mathbf{I}_4$ lays on such plane as well.

3.4 Fully numerical algorithm: DIRECTFN

One last method discussing the singularities of the Green function is presented in this section. Such a method was presented in detail in [27], it is based on a fully numeric approach and we refer to it from now on as DIRECTFN. This section is simply presented for the sake of completeness from the theoretical point of view, but it will not be adopted in the following analyses. As it will be explained at the end of this section, they provide a very general approach at the expense of efficiency.

The analysis presented in this section is carried out in the case of singular integrals resulting again from the application of SIE through the Galerkin method. In particular, we discuss the SIE formulations arising from the *Maxwell single layer potential* and the *Maxwell double layer potential*, namely:

$$\boldsymbol{\mathcal{L}}(\boldsymbol{\Lambda})(\mathbf{r}) = ik\boldsymbol{\mathcal{S}}(\boldsymbol{\Lambda})(\mathbf{r}) - \frac{1}{ik}\nabla\mathcal{S}(\nabla'_s \cdot \boldsymbol{\Lambda})(\mathbf{r}) \tag{3.35}$$

$$\mathcal{K}(\boldsymbol{\Lambda})(\mathbf{r}) = \nabla \times \boldsymbol{\mathcal{S}}(\boldsymbol{\Lambda})(\mathbf{r}) \tag{3.36}$$

where Λ identifies the suitable basis or testing function and the following definitions hold for the *single layer (acoustic) potentials*:

$$\boldsymbol{\mathcal{S}}(\boldsymbol{\Lambda})(\mathbf{r}) = \int_S d\mathbf{r}' G(\mathbf{r},\mathbf{r}')\boldsymbol{\Lambda}(\mathbf{r}') \tag{3.37}$$

$$\mathcal{S}(f)(\mathbf{r}) = \int_S d\mathbf{r}' G(\mathbf{r},\mathbf{r}') f(\mathbf{r}') \tag{3.38}$$

Moreover, the integration is only implemented over edges l of the triangles which are either shearing a vertex (Vertex Adjacent, VA), an edge (Edge Adjacent, EA), or coincident with themselves (Self Term, ST). Therefore, after the application of the Galerkin method, the singular integrals we want to solve become:

$$(I^l_{\mathcal{L}})_{m,n} = ik\int_{S_P} d\mathbf{r}\boldsymbol{\Lambda}_m \cdot \int_{S_Q} d\mathbf{r}' G\boldsymbol{\Lambda'}_n + \frac{1}{ik}\int_{S_P} d\mathbf{r}\nabla_S \cdot \boldsymbol{\Lambda}_m \int_{S_Q} d\mathbf{r}' G\nabla'_S \cdot \boldsymbol{\Lambda'}_n \tag{3.39}$$

$$(I^l_{\mathcal{K}})_{m,n} = \frac{1}{2}\int_{S_P} d\mathbf{r}\boldsymbol{\Lambda}_m \cdot \boldsymbol{\Lambda'}_n + \int_{S_P} d\mathbf{r}\ \hat{\boldsymbol{n}} \times \Lambda_m \int_{S_Q} d\mathbf{r}' \nabla G \times \boldsymbol{\Lambda'}_n \tag{3.40}$$

where m, n identify the appropriate divergence conforming basis or testing functions and P, Q are respectively the observation and the source triangles. An interesting observation regards both the integrals, which turn out to be weakly singular in the specific case of curvilinear elements, and in particular, the second term of (3.40) vanishes when we consider planar elements. Moreover, the basis and the testing functions that are taken into account for this method are respectively the RWG and the BC, for the same considerations expressed in section 2.2.

The main idea behind the DIRECTFN method is to introduce a series of variable transformations to cancel the singularities that appear in previous integrals. Such

transformation consists in the introduction of an equilateral parameter space for each triangle, $\{\eta, \xi\}$, such that $-1 \leq \eta \leq 1$ and $0 \leq \xi \leq \sqrt{3}(1 - |\eta|)$ and the governing transformations from the original space are:

$$\mathbf{r} = \begin{bmatrix} \frac{x_1+x_2}{2} \\ \frac{y_1+y_2}{2} \\ \frac{z_1+z_2}{2} \end{bmatrix} + \begin{bmatrix} \frac{x_2-x_1}{2} & \frac{2x_3-x_1-x_2}{2\sqrt{3}} \\ \frac{y_2-y_1}{2} & \frac{2y_3-y_1-y_2}{2\sqrt{3}} \\ \frac{z_2-z_1}{2} & \frac{2z_3-z_1-z_2}{2\sqrt{3}} \end{bmatrix} \begin{bmatrix} \eta \\ \xi \end{bmatrix} = [\mathbf{A}] + [\mathbf{Q}] \begin{bmatrix} \eta \\ \xi \end{bmatrix} \tag{3.41}$$

with a constant Jacobian $J = A/\sqrt{3}$ and A is the area of the original triangle. This way the integrals in (3.39) and (3.40) can be evaluated by:

$$I = (J_p, J_q) \int_{-1}^{1} d\eta \int_{0}^{\xi(\eta)} d\xi \int_{-1}^{1} d\eta' \int_{0}^{\xi(\eta')} d\xi' \tag{3.42}$$

where $\xi(\eta) = \sqrt{3}(1 - |\eta|)$, J_p, J_q are the associated Jacobians and the kernels we have are only functions of the geometrical data so that they can be expressed as:

$$\begin{aligned} \zeta_1 &= \frac{\sqrt{3}(1-\eta) - \xi}{2\sqrt{3}} \\ \zeta_2 &= \frac{\sqrt{3}(1+\eta) - \xi}{2\sqrt{3}} \\ \zeta_3 &= \frac{\xi}{\sqrt{3}} \end{aligned} \tag{3.43}$$

The toolbox for the immediate implementation of this method is available online at [28]. Finally, regarding the efficiency of fully numerical methods such as DIRECTFN, it could be observed that they provide an approach that is less efficient than methods that involve analytical integrations. On the other hand, they can be generally applied to compute both weakly and strongly singular integrals, meaning that they have a wider range of validity.

3.5 Comparison of integration methods

In this section, we will discuss some remarkable results concerning the formulations developed above. In particular, we will first show the behavior of each single integrals (2.69), (2.70), (2.71), (2.72) computed through all the methods presented in the previous chapter to observe that the block components of the matrices are computed suitably concerning the theoretical results. We also take into account a fully numeric integration method implemented using the Gaussian quadrature rule applied to the general integrated functions and with a variable number of points of integration points.

3.5.1 Behaviour of integrals with frequency

The first proposed analysis concerns the trends of the fundamental integrals as a function of the frequency. Here the source triangle S' is identified with the vertices with coordinates $(0,0,0)$, $(0,1,0)$, $(1,0,0)$, in mm, while the target point is located at $\mathbf{r} = (0.49, 0.5, 0)$ mm.

The complex wavenumber shown in (2.15) is considered in this analysis, where $\sigma = 10^6$ S/m and $\varepsilon_r = 1$. The absolute value of the real part of I_1 for the frequency range $[10^6 - 10^{12}]$ Hz is reported in Fig. 3.3.

It is worth noting that by increasing the number of Gauss points for the numerical quadrature, both the fully numeric evaluation of I_1 and the singularity subtraction method increase their accuracy. For the former, the reason is trivial, while for the latter the increased accuracy can be traced back to the improved numerical integration of the smooth Green's kernel part G_s (3.13).

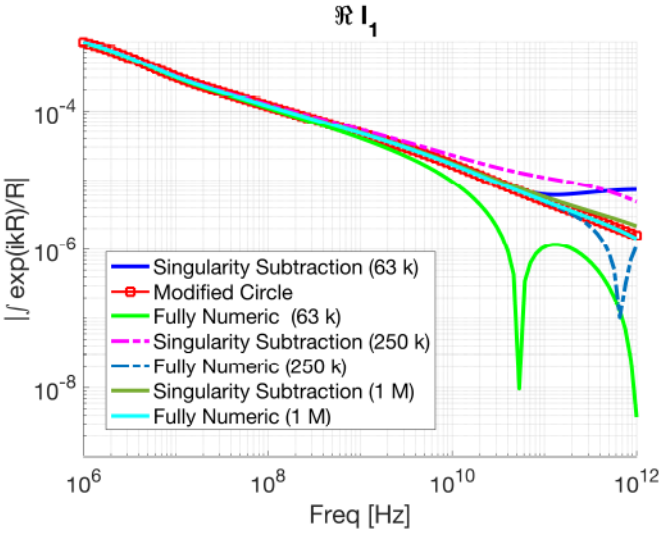

Figure 3.3: Absolute value of the real part of I_1 as a function of frequency and number of integrations points.

The same kind of analysis is presented for $\mathbf{I}_2$ in Fig. 3.4 but with fewer considered methods. Specifically the modified line integral method and the numerical quadrature rule with an increasing number of Gauss points are considered. The former is assumed as a representative of the semi-analytical methods since it is the one which seems not to break or show strange behavior at high frequencies. The same test triangle, target point, and input parameters for the wavenumber as above are adopted for this analysis.

About the outcoming results, we can notice that the two methods show very similar behavior in the frequency range $[10^6 - 10^9]$, even with a, relatively if we compare to the analysis of Fig. 3.3, low number of Gauss points. However, as f approaches 10^{10} Hz, the numerical approach starts to spread from the result provided by the modified line method. In any case, it was verified that in agreement with what is shown above for I_1, by increasing the number of integration points the order of accuracy of the numerical

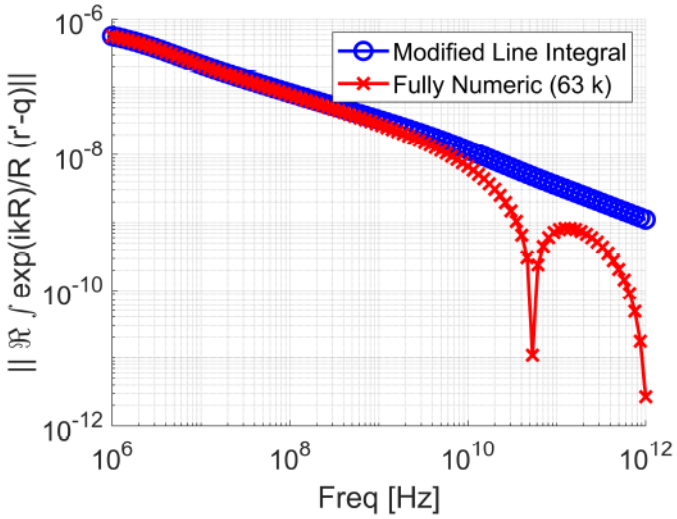

(a) Real component of $\mathbf{I}_2$.

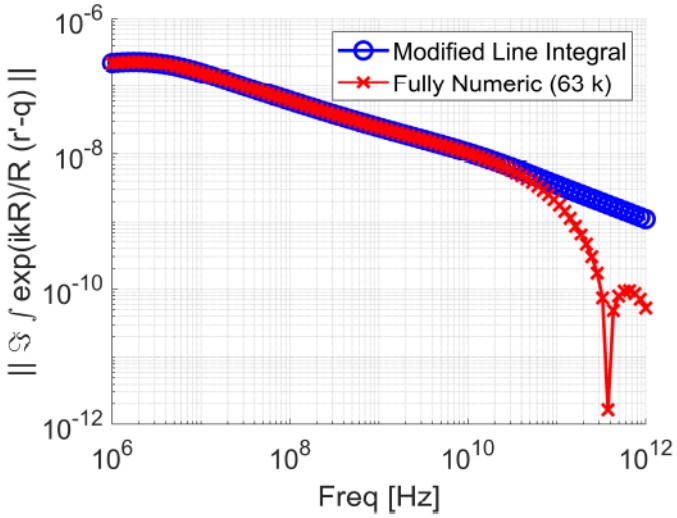

(b) Imaginary component of $\mathbf{I}_2$.

Figure 3.4: Norm of $\mathbf{I}_2$ obtained by modified line integral method and fully numeric approach with 63k Gauss points.

rule improves as well.

To conclude the analysis about I_1 and $\mathbf{I}_2$ obtained with the *modified integral method*, we show here one last case study. Since these integrals can be obtained from the simple evaluation of the three quantities I_0, I_α, and $\mathbf{I}_\beta$, we perform this analysis in order verify the effectiveness of their value. In particular, we focus on the argument and the phase of such results, computed through the application of a fully numeric method with a variable number of Gauss points. Indeed these integrals can be computed in two different ways: the first one is based on a numerical technique that is already implemented in MATLAB®, for which an absolute error tolerance should be provided as an input. This approach is the one adopted e.g. for the computation of I_1. Differently, the second one is based on adopting a variable number of Gauss points for applying

the Gaussian quadrature rule to the function over the triangle. This method is applied here to compare the behavior of each of the two integrals with the increment of the number of points.

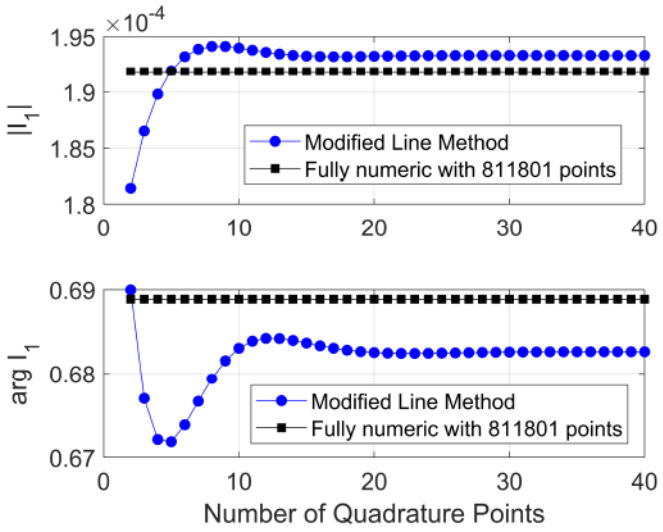

Figure 3.5: Argument and phase of I_1, obtained by a fully numeric approach and by the modified integral method whose components were computed by quadrature rule with an increasing number of Gauss points.

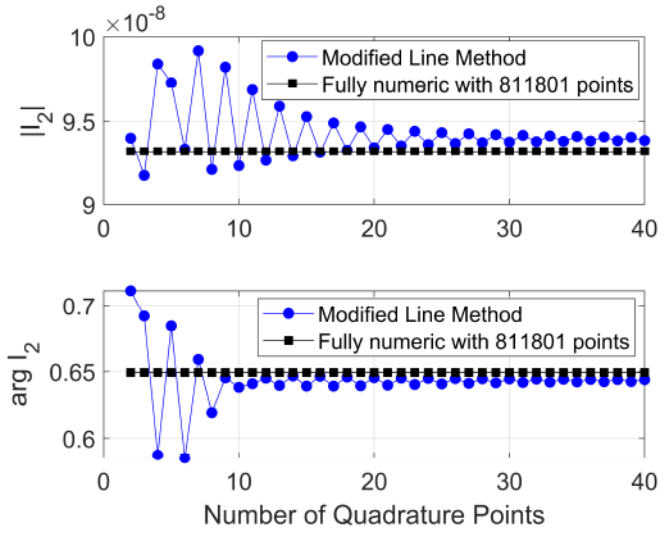

Figure 3.6: Argument and phase of $\mathbf{I}_2$ (y-component), obtained by a fully numeric approach and by the modified integral method whose components were computed by quadrature rule with an increasing number of Gauss points.

The input parameters which were adopted for such analysis are again the position of the vertices of the triangle $(0,0,0)$, $(0,1,0)$, $(1,0,0)$, and the position of target points $(0.49, 0.50, 0)$, both assumed in mm. The complex wavenumber in (2.14) is obtained considering $\sigma = 10^6$ S/m, $\varepsilon_r = 1$ and $f = 30$ MHz. The number of Gauss points for the general numerical approach is approximately 800k, so we can assume such a function to

be very similar to the analytic value. The number of points for computing I_0, I_α, and $\mathbf{I}_\beta$, increases from 2 to 40, showing an increment of the degree of accuracy as well. The final values are collected into I_1 and $\mathbf{I}_2$ and then split into the argument and the phase of such quantities. The graphical results are reported in Fig. 3.5 and Fig. 3.6, where their validity is indeed shown when compared to the fully numeric value computed with a huge number of integration points.

The results developed for I_1 and $\mathbf{I}_2$ can be then used to extend the same kind of analysis also to $\mathbf{I}_3$ (2.71) and $\mathbf{I}_4$ (2.72). Since here the integrated functions present a singularity of order greater than one, they have to be treated with much more attention. Therefore we discuss the behavior of such integrals computed with *Modified Line Integral Method* from Section 3.3 and their numerical counterpart. The input parameters we adopt here almost coincide with the analysis proposed above, apart from the target point which is moved to position $(0.49, 0.50, 0.10)$ mm. Thanks to the brief discussion at the end of the same section about the situation that arises $\mathbf{d} = 0$, we wish to move the attention to a more general situation for which all the three components of the integral are different from zero to verify the validity of the adopted method.

Observing the graphs we can easily notice how the *Modified Line Integral* method provides a good approximation for the numerical values. In particular, we can focus on the behavior at very high frequencies: differently from what happened for I_1 and $\mathbf{I}_2$ for which the correspondence broke down, here the oscillations are captured very well by the method we have implemented.

Finally, the analysis of $\mathbf{I}_4$ as a function of the frequency is reported. The same input parameters of the first analyses and the same target point of the analysis of $\mathbf{I}_3$ are assumed for this study case. The point $\mathbf{q}$ (which should be associated with the vertex of the target triangle opposite to the edge to which the RWG basis function is applied) is arbitrarily identified with the vertex $(0, 0, 0)$. The range of variation of the frequency is reduced to $[10^9 - 10^{12}]$ to better appreciate the frequencies at which the differences between the analyzed approaches become more pronounced.

The graphical results are reported in Fig. 3.8, where we can notice that, as happened for $\mathbf{I}_3$, the behavior of the integral as a function of the frequency and computed by adopting the numerical approach is closely followed by the one computed through *Modified Line Integral* method. Moreover, thanks to the reduction of the range of frequencies, it is possible to notice that even at very high values of f in [Hz] the oscillations of the function are well captured by the *Modified Line Integral* method.

3.5.2 Behaviour of integrals with target point position

Now we move to the analysis of the same main integrals as a function of the position of the active point in the space, keeping the frequency fixed. The input parameters that were implemented are the coordinates of the vertices of the test triangle $(0, 0, 0)$, $(0, 1, 0)$, $(1, 0, 0)$, and the positions of target points, which are a total of 2500 uniformly distributed in the squared domain $[-1.5, 1.5] \times [-1.5, 1.5]$ at a constant height $z = 0$.

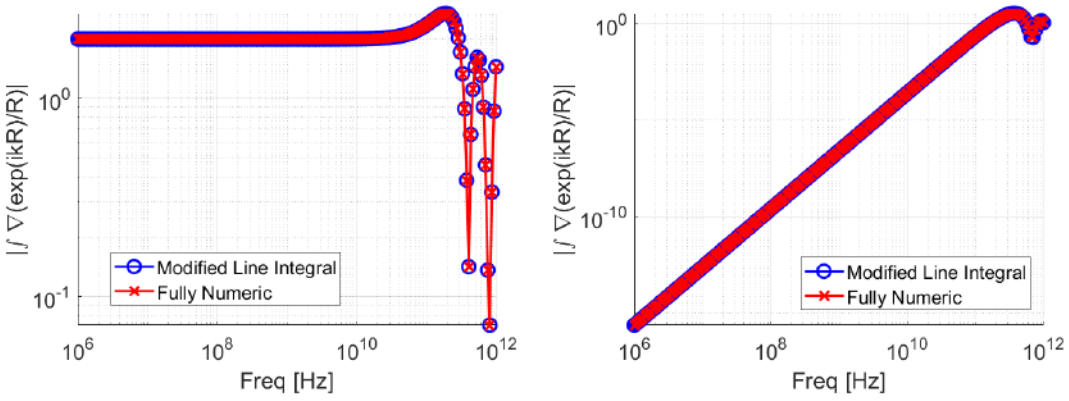

(a) Real component along x of $\mathbf{I}_3$.

(b) Imaginary component along x of $\mathbf{I}_3$.

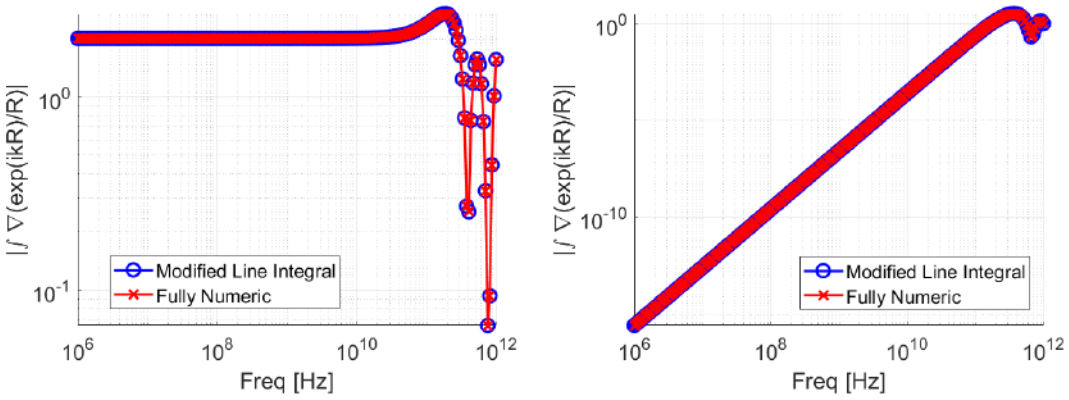

(c) Real component along y of $\mathbf{I}_3$.

(d) Imaginary component along y of $\mathbf{I}_3$.

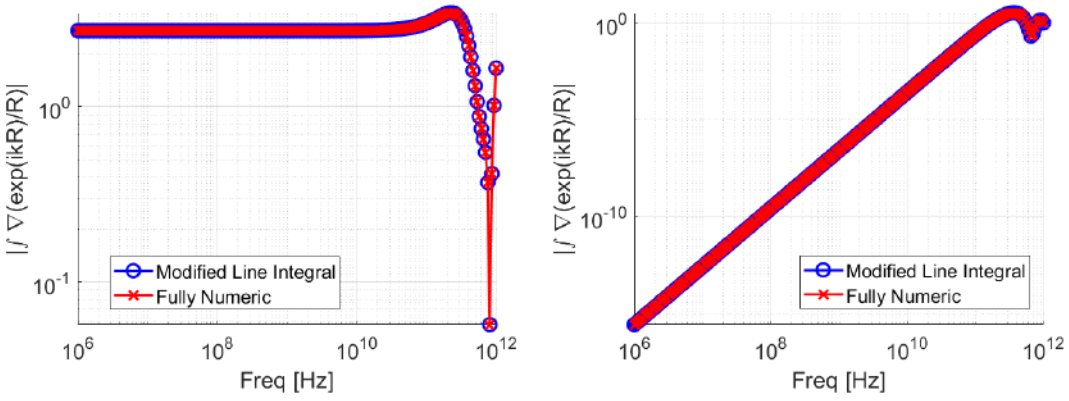

(e) Real component along z of $\mathbf{I}_3$.

(f) Imaginary component along z of $\mathbf{I}_3$.

Figure 3.7: Real and imaginary components of $\mathbf{I}_3$ obtained by modified line integral method and fully numeric approach with 63k Gauss points.

Notice that all the units of the coordinated points are in mm. The complex wavenumber described by (2.14) is again considered here, adopting the same parameters as in the previous section, but keeping the frequency constant. A comparison between the values of I_1 with the greatest part of the methods illustrated in the chapter above is given. The fully numeric analysis is performed with about $10k$ points for each active point in order not to make heavy from the time CPU point of view the numerical analysis.

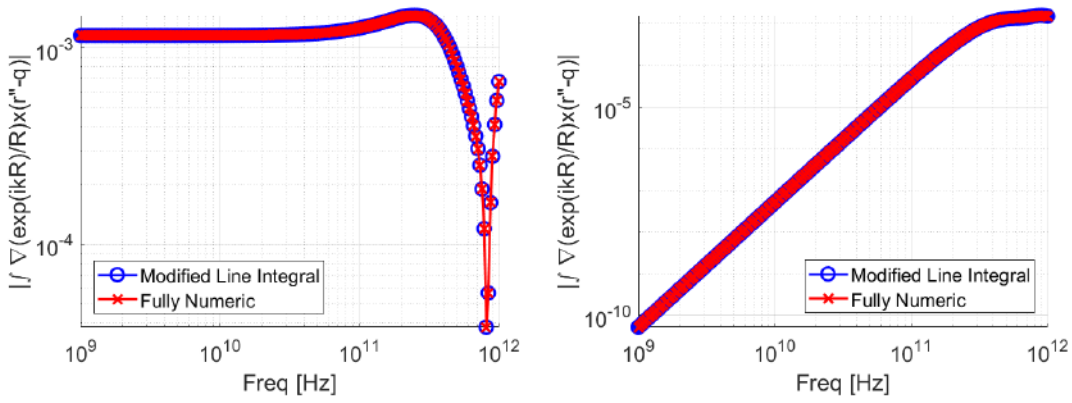

(a) Real component along x of $\mathbf{I}_4$. (b) Imaginary component along x of $\mathbf{I}_4$.

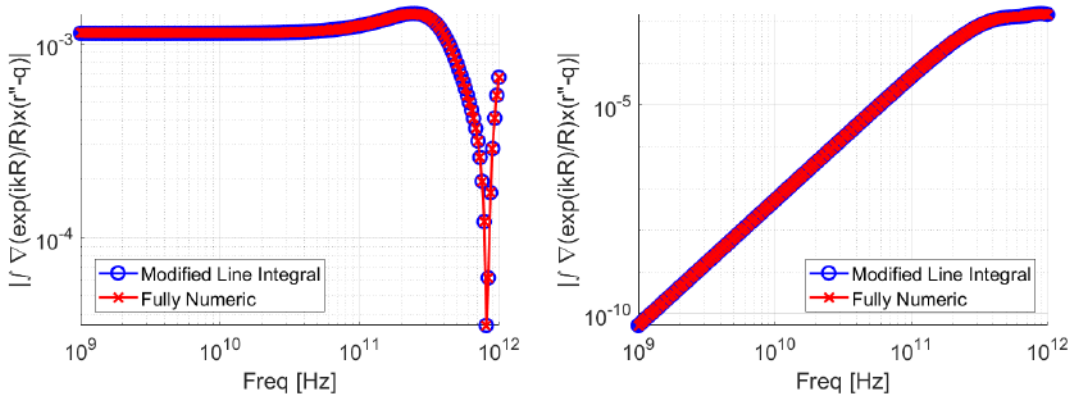

(c) Real component along y of $\mathbf{I}_4$. (d) Imaginary component along y of $\mathbf{I}_4$.

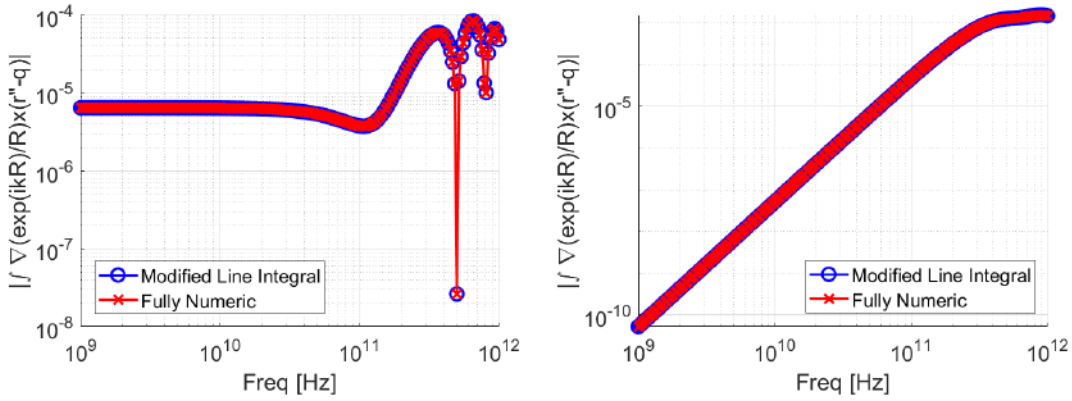

(e) Real component along z of $\mathbf{I}_4$. (f) Imaginary component along z of $\mathbf{I}_4$.

Figure 3.8: Real and imaginary components of $\mathbf{I}_3$ obtained by modified line integral method and fully numeric approach with 63k Gauss points.

As a starting point, the low-frequency behavior of the integral is analyzed, and $f = 100$ Hz is adopted. We can notice that the numerical approach provides a very good approximation even with a quite small number of Gauss points. Furthermore, it can be observed that in such cases Fabbri's approach, which neglects the exponential term, is a good approximation for I_1, indeed, the real parts shown in Fig. 3.9 agree very well with the value provided by the other three methods. The imaginary parts, given in

Fig. 3.10, are different since Fabbri's integral is only real.

Two further observations can be made: the first one verifies when increasing the operational frequency e.g. to $f = 10^7$ Hz. In this way, the contribution of the exponential terms increases and the low-frequency Fabbri's method starts to provide a no longer valid approximation for the Green dynamic function. The imaginary part highlights the same reasoning as above so it is not reported here while the real part of I_1 in such conditions is printed in Fig. 3.11.

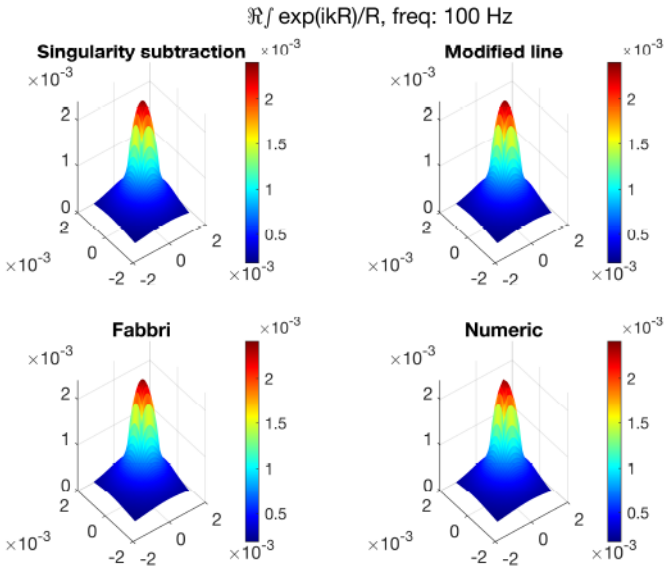

Figure 3.9: I_1 real values as a function of the position computed by methods in previous sections with a frequency of 100 Hz.

The second observation regards the behavior of $\mathbf{I}_2$, $\mathbf{I}_3$ and $\mathbf{I}_4$. A direct parallelism can be made between between integrals I_1 and $\mathbf{I}_3$ and between integrals $\mathbf{I}_2$ and $\mathbf{I}_4$. In fact the latter present an integrand function which is expressed in terms of the point $\mathbf{q}$. At the same time I_1 and $\mathbf{I}_2$ share the same integrand function apart for the cross product inside $\mathbf{I}_2$, as well as for what happens between $\mathbf{I}_3$ and $\mathbf{I}_4$. Then, in order to simplify the analysis, the differences among the four methods can be summarized into two main cases, i.e. the analysis of I_1 and $\mathbf{I}_3$, which can be considered as the respective simpler counterparts. This way, once we have verified that the behavior of such integrals computed through any of the semi-analytical methods and by the fully numeric one are similar to each other, we can also assume that the values obtained for $\mathbf{I}_2$ and $\mathbf{I}_4$ follow this regularity thanks to the fact that the cross product provides the same factor both when computed with a semi-analytical or fully numeric approach. Therefore, in analogy to what discussed also at the end of the previous section, since such techniques do not showed significant differences when studying $\mathbf{I}_2$ as a function of the frequency, the results are not reported. Despite of all these considerations which allowed to lighten the thesis work, all the checks were performed to assure the correct

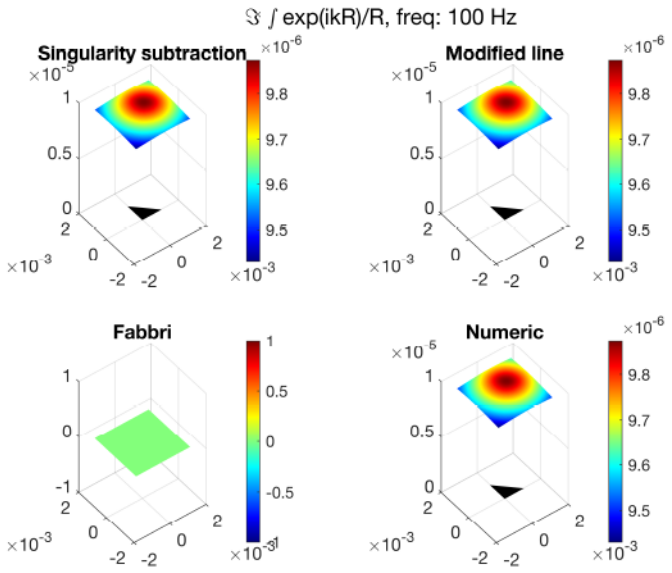

Figure 3.10: I_1 imaginary values as a function of the position computed by methods in previous sections with a frequency of 100 Hz.

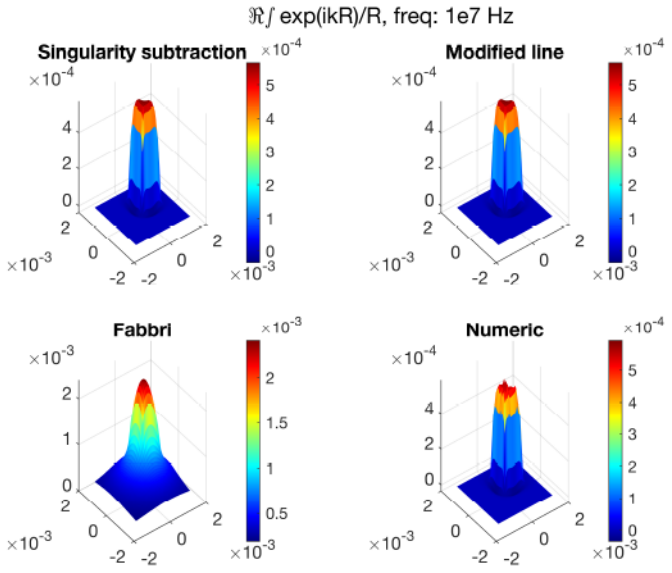

Figure 3.11: I_1 real values as a function of the position computed by methods in previous sections with a frequency of 10^7 Hz.

behavior of each integral.

Finally the analysis of (2.71) as a function of the position of the source point is performed. The argument of the integral now involves the divergence of the Green function and so the behavior is in principle different from what computed for I_1. The inputs assumed here are similar to the previous analysis, i.e. the vertices of the triangle are located $(0,0,0)$, $(0,1,0)$, $(1,0,0)$ mm, the active point assumes one of the possible 2500

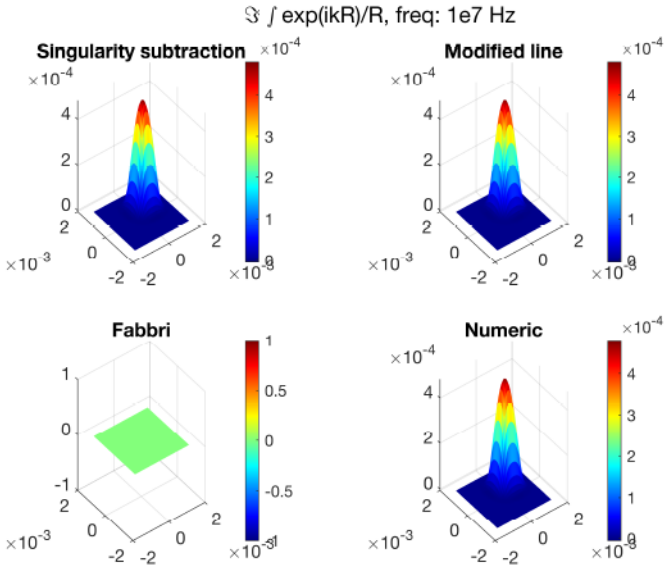

Figure 3.12: I_1 imaginary values as a function of the position computed by methods in previous sections with a frequency of 10^7 Hz.

discrete positions inside the area $[-1.5, 1.5]\text{mm} \times [-1.5, 1.5]\text{mm}$ at a constant height of $z = 0.1\text{mm}$. The complex wavenumber described by (2.14) is taken into account here, adopting the same parameters as in the previous paragraph, apart from the (high) frequency which is kept constant at $f = 10^9$. Fig.3.13 and Fig.3.14 respectively show

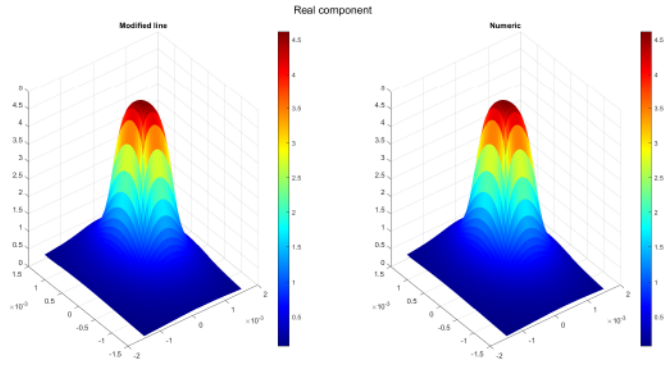

Figure 3.13: I_3 real values as a function of the position computed by methods in previous sections with a frequency of 10^9 Hz.

the comparison between the real and the imaginary parts of the solution computed via modified line integral method and fully numeric approach, making us observe that the SIE method provides a very good approximated result. Finally, extending what stated above, we can assume (and it was indeed verified) that the behavior of the solution computed for $\mathbf{I_4}$ by the modified line integral method and the fully numeric one are very similar to each other.

Summarizing, in this section the performances of the different methods proposed

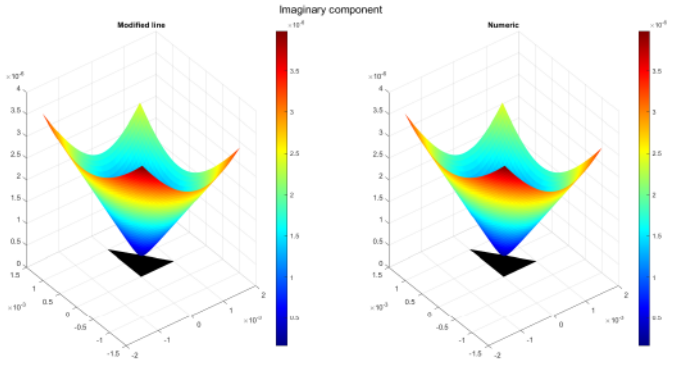

Figure 3.14: I_3 imaginary values as a function of the position computed by methods in previous sections with a frequency of 10^9 Hz.

in the literature for the evaluation of the singular integrals (2.69)-(2.72) are compared. The well-known analytical method proposed by Fabbri works well for the static or very low-frequency regime, indeed the oscillating part carried by the exponential term in Green's function (2.13) is completely neglected. In the literature, singularity subtraction was the first proposed approach to analytically compute the singular integrals, however, as highlighted in [11], it may fail under certain operational conditions, embedded in the complex wavenumber k. This limitation is overcome by exploiting the modified line integral method. It is worth noting that a fully numeric approach for the evaluation of the integral may be conceived, as shown in Fig. 3.3, a huge number of Gauss points are required to reach the convergence, making this solution practically unfeasible.

3.6 Numerical solution of RCS of PEC sphere

In this section, the numerical solution of the *Perfect Electrical Conducting* (PEC) sphere is performed. The PEC sphere is a canonical structure used in the study of electromagnetic scattering phenomena since its *Radar Cross Section* (RCS) formula is well known from the analytical point of view. Some examples of papers adopting such a model as a reference are given by [29, 30, 31]. A couple of papers discussing the RCS behavior of specific objects involving the PEC sphere are [32, 33, 34, 35]. In our test, following the academic benchmark, the PEC sphere is excited by a plane wave of the form:

$$\mathbf{E}_i(z) = \exp(-ikz)\hat{\mathbf{x}}, \tag{3.44}$$

where in this case $k = k_0$ is the vacuum wavenumber.

The analytic form of the excitation of electrical eddy current for a sphere is described in [36]. The solution is obtained in analogy to what one can get from the analysis of a cylinder subjected to a field deployed along a transversal direction from its axis, after a proper change to spherical coordinates. To show that, let's consider Maxwell's equations

introduced at the beginning of Chapter 2. The total magnetic field is obtained from the linear superimposition of two contributions: $\mathbf{B} = \mathbf{B}_i + \mathbf{B}_e$, where the first term comes from the application of arbitrarily imposed external sources, while the second one is given by eddy field which arises from the charges moving inside any conductive material. Since $\mathbf{B}_i$ is generated by external agents beyond the region of interest, it is possible to assume that it has null curl $\nabla \times \mathbf{B}_i = 0$, while for the second term, it simply holds:

$$\nabla \times \mathbf{B}_e = \mu_0 \mathbf{J}_e \tag{3.45}$$

Considering Ampere's law $\nabla \times \mathbf{B} = \mu_0 \sigma \mathbf{E}$ and applying to it the curl operator to both sides of the equations, as well as all the considerations seen in this paragraph and the vectorial identity shown in Chapter 2, the result we get states:

$$\nabla^2 \mathbf{B}_e + k^2 \mathbf{B}_e = -k^2 \mathbf{B}_i \tag{3.46}$$

where k is the usual complex wavenumber. Once the solution for $\mathbf{B}_e$ is computed from such equation, the induced current density $\mathbf{J}_e$ can be obtained straightforward from (3.45). Now, since the cylinder does not show any symmetry concerning which the solution of the problem is easy to compute, we need to recall the Gauss' law $\nabla \cdot \mathbf{B} = 0$ so that the vector potential field $\mathbf{A}$ can be associated to the magnetic field through:

$$\mathbf{B} = \nabla \times \mathbf{A} \tag{3.47}$$

In analogy to what is seen again in the theoretical introduction, we can recall the definition of the electric scalar potential coming from Faraday's law (2.8). Following the already seen procedure which considers the application of Ampere's law, of Ohm's law, and of the gauge $\nabla \cdot \mathbf{A} = \mu_0 \sigma \varphi$, the final formulation we want to take into account is expressed by:

$$\nabla^2 \mathbf{A} + k^2 \mathbf{A} = 0 \tag{3.48}$$

The importance of such an equation can be highlighted by noting that $\mathbf{A}$ exactly expresses the nonhomogeneous source term $\mathbf{B}_i = B_0 \hat{\mathbf{x}}$ in cylindrical coordinates as:

$$\mathbf{A}_i(\rho, \phi) = B_0 \rho \sin(\phi) \hat{\mathbf{z}} \tag{3.49}$$

where ϕ is the azimuthal coordinate and ρ is the radial one. Let's also notice that the orthogonality of $\mathbf{A}$ and $\mathbf{B}$ makes the first to be directed along $\hat{z}$, imposing that the final solution coming from the Helmholtz equation will be expressed along the same axis. In particular the functional form of the solution is $\mathbf{A} = A(\rho, \phi)\hat{\mathbf{z}}$ and the corresponding Helmholtz equation should satisfy:

$$\rho^2 \frac{\partial^2 A}{\partial \rho^2} + \rho \frac{A}{\rho} + k^2 \rho^2 A = -\frac{^2 A}{\phi^2} \tag{3.50}$$

whose solution can be found by the application of the separation of variables. From the outcoming solution, it is possible to notice that the current density satisfies the relation:

$$\mathbf{J}_e = -i\omega\sigma\mathbf{A} \tag{3.51}$$

and then, by solving for the total eddy current density we get the solution for the case of a cylinder subjected to a transverse excitation:

$$\mathbf{J}_e(\rho,\phi) = \hat{\mathbf{z}}\left[\frac{-2i\omega\sigma B_0 R}{kRJ_1'(kR)+J_1(kR)}\right] J_1(k\rho)\sin(\phi) \tag{3.52}$$

where J_1 is the Bessel function of order 1 and R is the radius of the base of the cylinder so that $\rho < R$. The extension of such analysis can be carried out for the sphere by applying a change of coordinates so that (3.48) is expressed as:

$$\frac{1}{r^2}\frac{\partial}{\partial r}\left(r^2\frac{\partial A}{\partial r}\right) + \frac{1}{r^2\sin\theta}\frac{\partial}{\partial\theta}\left(\sin\theta\frac{\partial A}{\partial\theta}\right) - \frac{A}{r^2\sin^2\theta} + k^2 A = 0 \tag{3.53}$$

where θ is the elevation angle, r is the radial coordinate, and ϕ is again the azimuth, and hence the final solution is:

$$\mathbf{J}_e(r,\phi) = \hat{\theta}\left[\frac{-3i\omega\sigma B_0 R}{2kRJ_1'(kR)+4J_1(kR)}\right] J_1(k\rho)\sin(\phi) \tag{3.54}$$

In the following, the monostatic RCS of the 1-meter radius PEC sphere is defined as:

$$RCS = 4\|\mathbf{r}_{trg}\|^2\mathbf{E}_s\cdot\mathbf{E}_s^*, \tag{3.55}$$

where $\mathbf{E}_s$ is the scattered field, $\mathbf{E}_s^*$ its conjugate, and $\mathbf{r}_{trg}$ is the observation point, which must be sufficiently distant from the object. The scattered field $\mathbf{E}_s$ is evaluated analytically with the MIE series [37] for the target point located at $\mathbf{r}_{trg} = [200, 200, 200]$.

The analytical solution (3.55) is thus compared with the implemented SIE approach, based on the modified line integral method, over the frequency range $5\cdot10^7 - 5\cdot10^8$ Hz. Such a frequency range is selected to capture several oscillations of the RCS and verify the capability of the numerical approach in following them. The results are reported in Fig. 3.15, where it can be seen that the accuracy of the numerical approach decreases for high frequencies. This is a well-known problem in SIE formulation, which can be reduced by increasing the quality of the mesh, following for example the empirical rule (2.28). Indeed for $f = 5\cdot10^8$ the mesh-size $h \geq \lambda_0/5$ so a mesh refinement must be performed. The RCS with the refined mesh of 2800 triangles is highlighted in Fig. 3.15 with the magenta marker.

The current density distribution induced on the surface of the PEC sphere, at the frequency of $f = 500$ MHz, is then analyzed with different numerical approaches. Fig 3.16 shows the magnitude of real and imaginary parts of $\mathbf{J}_s$ with the SIE method described in this work. The resulting trend agrees very well with the solution obtained

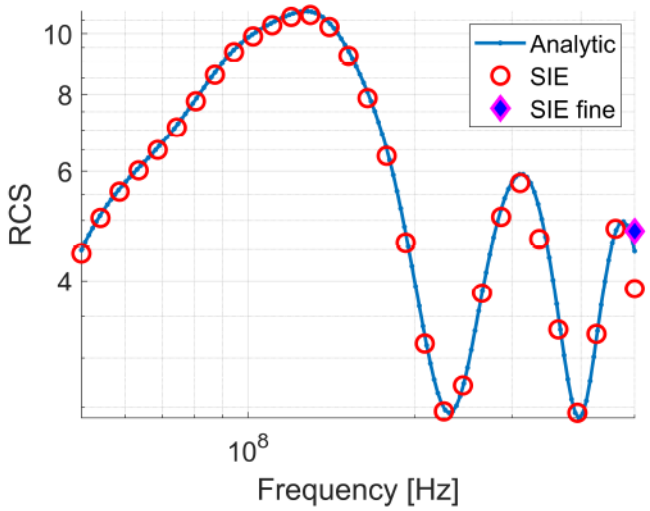

Figure 3.15: Monostatic RCS of the unit sphere over the range $5 \cdot 10^7 - 5 \cdot 10^8$ Hz. Comparison between the analytic formula (3.55) and the numeric solution, by using a coarse mesh (in red) and a fine mesh only for $f = 500$ MHz.

with a reference integral equation solver, illustrated in Fig 3.17.

It's important to highlight a significant distinction that emerges when assessing singular integrals through a fully numeric approach as opposed to the semi-analytical method outlined in Section 3.3. To demonstrate this, three distinct domain discretizations, labeled as *mesh 1*, *mesh 2*, and *mesh 3* with 2800, 6500, and 12000 elements, respectively are executed. The resulting surface current density magnitudes are reported in Fig. 3.18. By using a Gauss quadrature with 9 points, as expected, the solution differs considerably concerning that illustrated in Fig. 3.16, and Fig. 3.17, especially for the *mesh 1*. The last mesh, with 12000 triangles, has a similar shape of the surface current density, however, the computational burden both for the storage and the solution of the linear system rapidly increases. This behavior suggests that both the meshing procedure and the evaluation of singular integrals, so the matrices of the system of equations, must be carefully addressed in the context of surface integral equation methods.

To conclude the section, the surface current density distribution evaluated with the commercial FEM software COMSOL® Multiphysics is reported. The PEC problem is solved in COMSOL® with the *Radio Frequency* (RF) module. To capture the oscillation on the sphere surface, a huge number of DOFs is required in this case, over 7M. This considerably increases both the memory requirements and the computational time for the solution as reported in Table 3.1. It is worth pointing out that a direct method is used in this case, indeed the suggested iterative solver is not able to reach the desired tolerance for the solution. The large computational time for the SIE based on the semi-analytic formulas described in Section 3.3, is due to a non-optimized numerical procedure. Indeed, the semi-analytical formulas are required only for near source and

Solver	DOFs Number	Memory [GB]	Time
FEM (COMSOL®)	7M	≈ 250	≈ 3 h
SIE (fully numeric)	30k (*mesh 3*)	≈ 8	0.4 h
SIE (semi-analytic)	7k (*mesh 1*)	≈ 0.5	1.5 h

Table 3.1: Comparison of computational resources for PEC sphere problem.

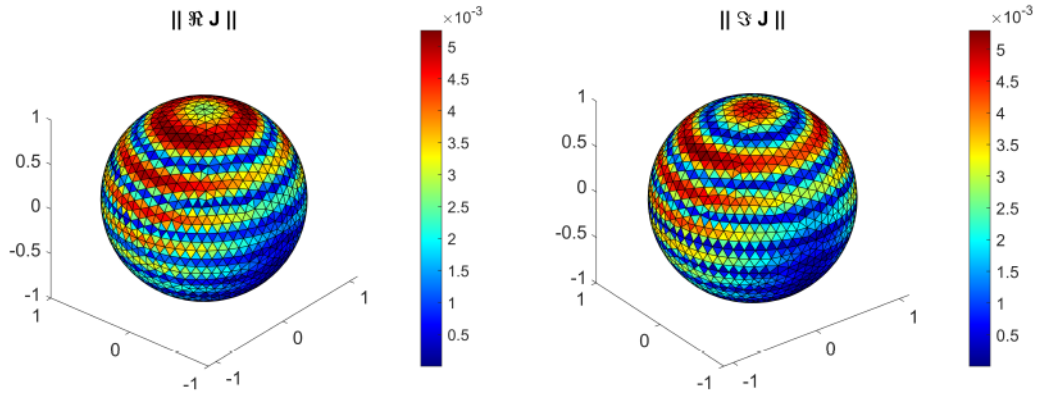

(a) Real part. (b) Imaginary part.

Figure 3.16: Norm of surface current density evaluated with the SIE approach developed in this work. The domain is discretized with 2800 triangles.

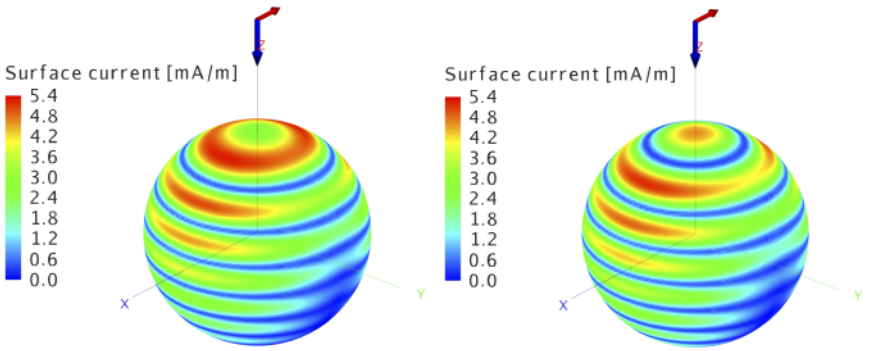

(a) Real part. (b) Imaginary part.

Figure 3.17: Norm of surface current density evaluated via a reference integral equation solver.

target points, where the singularities arise. If the points are sufficiently far apart, the fully numerical approach can be used. However, the decomposition between near and far points is not performed.

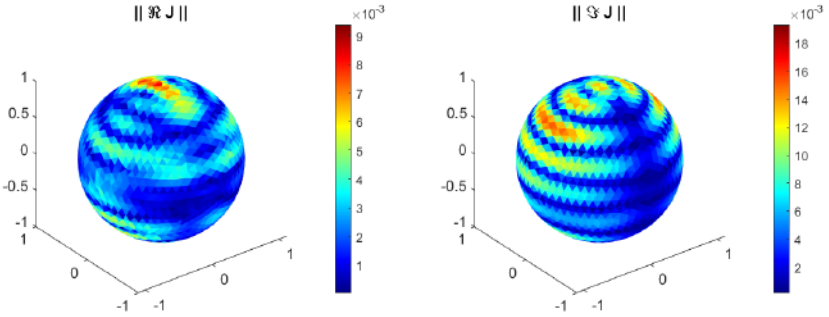

(a) Real part *mesh 1* (2800 triangles).(b) Imaginary part *mesh 1* (2800 triangles).

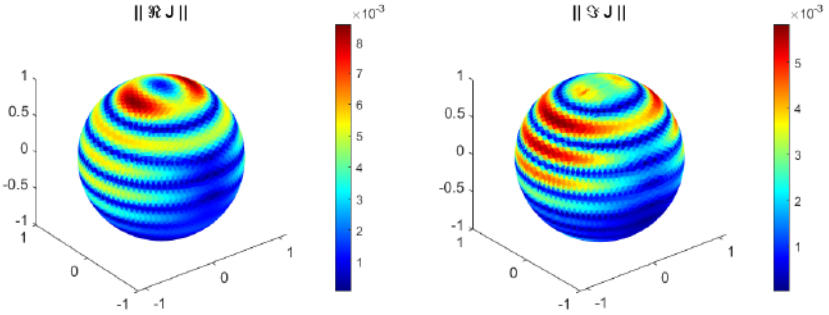

(c) Real part *mesh 2* (6500 triangles).(d) Imaginary part *mesh 2* (6500 triangles).

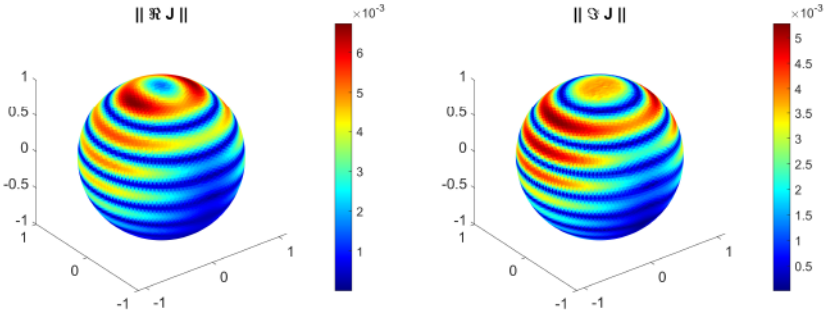

(e) Real part *mesh 3* (12000 triangles).(f) Imaginary part *mesh 3* (12000 triangles).

Figure 3.18: Norm of surface current density for different meshes evaluated with the fully numeric integration approach.

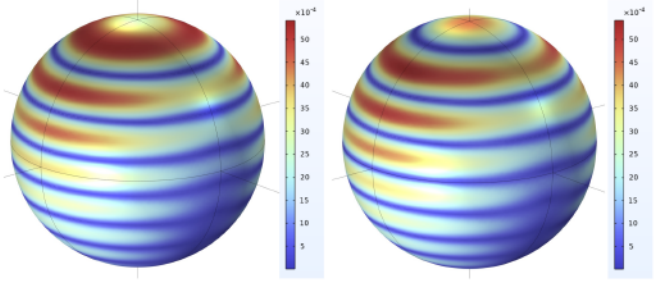

(a) Real part. (b) Imaginary part.

Figure 3.19: Norm of surface current density evaluated via the FEM software COMSMOL® Multiphysics.

Chapter 4

Accelerating integral equations

The block matrices we have described above are in general sparse, except for the ones depending on the Green's function. Indeed, even in the static case and even for points very far from each other, such an expression always provides a term different from the null one. This way the total cost for storing each matrix is of order $\mathcal{O}(N^2)$, where N is the number of degrees of freedom of the problem. For small-order problems, this question can be simply neglected since the computational cost for storing matrices is still sustainable. But when N starts to become very large, the total cost in terms of CPU memory required could be not enough, or, even when it is, the convenience of integral methods such as SIE in terms of computational time cost with respect e.g. to FEM fails to meet. In summary, the purpose of the techniques presented in this section is to express conveniently the matrices whose terms depend on the Green function, to make them have a total number of elements that scale with N with an order smaller than 2.

Nowadays many important techniques can be adopted: one first example is given by the speed-up of the methods for the computation of near-optimal matrices, i.e. matrices that share the same rank of another starting matrix. In particular, once the initial dense block, e.g $\mathbf{A}$, is approximated through the application of methods for rank-reduction e.g. with $\mathbf{A}_{approx}$, it could be useful to substitute such result with a third matrix, e.g. $\mathbf{C}$ in such a way that

$$\|\mathbf{A} - \mathbf{C}\| \leq \|\mathbf{A} - \mathbf{A}_{approx}\| + \delta \tag{4.1}$$

where δ represents the tolerance for the error committed. The main advantage shown by this method concerns the fact that the A is first sparsified and then quantified, considerably reducing the memory needed to store it and the CPU time required for the computations. These steps are discussed in detail in [38] where a further speed-up of the method based on the use of orthogonal iterations or Lanczos iterations is implemented.

A second remarkable way to proceed is the *Tensor Train* (TT) decomposition presented in [39] and then extended and applied in [40]. The idea behind this approach consists of decoupling the function expressing the entries of a tensor $\mathcal{A}$ having elements

$\mathcal{A}(i_1, \ldots, i_d)$, where $i_j \in I_j = \{1, \ldots, N_j\}$, by:

$$\mathcal{A}(i_1, \ldots, i_d) = G_1(i_1) \cdot G_2(i_2) \cdot \ldots \cdot G_d(i_d) \tag{4.2}$$

where $G_k(i_k)$ is an $r_{k-1} \times r_k$ matrix and r is the rank of the tensor. This way the outcoming product is itself a matrix of size $r_0 \times r_d$ and -under suitable boundary conditions e.g. $r_0 = r_d = 1$- it can be noticed to be a straightforward block generalization of the rank-1 tensor. The tensor train approach allows to store the tensor $\mathcal{A}$ with $\mathcal{O}(dr_{max}^2 N)$, with r_{max} the maximum rank of the decomposition. Thus, the decomposition is extremely convenient for small r_{max}, as is usually the case. TT shows its efficiency in the specific case of systems of linear algebraic equations involving purely Toeplitz matrices, meaning that the mesh expressing the problem should be regular enough. Under such conditions, both the memory and CPU time scale with $\mathcal{O}(\log N)$. To make this approach more general and applicable to arbitrarily shaped inhomogeneous objects, an iterative conjugate gradient-TT method was also developed [41], having CPU and memory scaling respectively as $\mathcal{O}(N)$ and $\mathcal{O}(r^2 N \log N)$, being r the *effective rank* of the matrix. However following works such as [42] it can be shown that TT loses its effectiveness when the surface of the domain, and hence the mesh, is not regular. Therefore the validity of the TT method is not completely proven and its field of application is nowadays quite limited.

One last procedure that will be mentioned regards the VINCO framework which was developed in the last years [43]. VINCO is briefly introduced since it is a method for specifically solving large-dimension VIE eddy-current problems. The main characteristics that make VINCO peculiar concerning other methods regard the use of element-wise uniform basis functions to approximate the continuous current density. Then the MAGICA factorization [44] allows the decomposition of the stiffness matrix representing the problem as a product of a dense matrix and a set of sparse matrices. An important advantage given by VINCO concerns the fact that it provides efficient and accurate results when adopted for solving problems having the properties introduced above and for any arbitrarily shaped geometry.

Nevertheless, this thesis work focuses on two approaches which are probably the most known and implemented thanks to their generality and because of their efficiency in the field of application of integral equations. In particular, two different methods will be presented, which differ from each other in the path they adopt to store in a convenient way large-size dense matrices. The first one is the *Fast Multipole Method* (FMM), arising from the analysis of the Green function which is decoupled into two different sub-functions to split the dependence from **r** and **r'**. The second method looks instead for a way to conveniently store the matrix by exploiting the mutual distance between the elements composing the domain; specifically, the *hierarchical matrices* method (briefly $\mathcal{H}$-matrix) will be discussed in this thesis work.

On one hand, the first approach will be presented with a didactic scope to have a general overview of the compressibility method for dense matrices based on the study

of the Green function, i.e. from the analytical point of view. Differently, the second section is dedicated to methods based on the geometry of the domain, which has to be analyzed in depth. Only the latter method will be investigated from the numerical point of view, comparing the results with the case where no storing technique is implemented, in terms of accuracy and memory saving.

4.1 Fast Multipole Method

An important method that is usually taken into account for solving issues of element storing for huge dimensional scale problems is the FMM. Here we focus on the particular field of application of electromagnetic scattering. The general formulation of the problem is presented in many different papers, such as [45, 46, 47, 48]. A point of view more related to the SIE is instead treated in [49].

As we have briefly introduced above, the main idea of the FMM consists of splitting the dependence of the Green function from **r** and **r**', so that the resulting one becomes

$$G(\mathbf{r}, \mathbf{r}') \approx \sum h(\mathbf{r}) f(\mathbf{r}') \tag{4.3}$$

where **r** and **r**' in this situation identify the central point of elements coming from the discretization of the domain and the summary is intended over all the elements. However, the separability of the Green function cannot be given for granted, so a more in-depth analysis is carried out.

The first proposed formulation is carried out in [45] and was obtained as an adaptation of the FMM developed for acoustic scattering problems [50] to exterior Dirichlet electromagnetic scattering problem. Since we aim to provide a simple overview for such a method, for simplicity a two-dimensional conducting body having an axis aligned with the z coordinate direction is considered. We also consider an electromagnetic wave incident to such a body with an electric field vector parallel to the axis of the body. This way both the incident and the scattered fields satisfy the equation:

$$\nabla^2 E_z + k^2 E_z = 0 \tag{4.4}$$

where $k = 2\pi/\lambda$ is the wavenumber and λ is the wavelength of the incident field in the exterior region. The boundary condition for the problem states that the total field **E** vanishes on the surface of the conductor, namely:

$$E_z^{tot} = E_{z,inc} + E_{z,scat} = 0 \qquad \text{on } \Gamma \tag{4.5}$$

where Γ represents the boundary of the conductor. Then we can also consider n nodes on the boundary of the scatterer and divide the boundary itself into p equal segments in such a way that each part contains n/p nodes and, being the total length of the boundary L, each segment's length is p/L. Let's finally denote the center of each

segment as z_i. Considering each segment as a cluster of n/p sources and considering the sources in each segment as a single aggregate source, the radiation field of the equivalent source is approximated using the first N multipoles located at the center of the segment. This way the radiation field at any particular node on the boundary is the sum of the contribution of N multipoles of each of the far-away segments and the direct contribution of the nearby segments.

To express these considerations from a mathematical point of view, we introduce the incident and the scattered electric field formula in the transverse magnetic (TM) case:

$$-2E_{z,inc}(\mathbf{r}) = \psi + 2\int_{\Gamma} dl' \frac{\partial G(k - \|\mathbf{r} - \mathbf{r}'\|)}{\partial n(\mathbf{r}')}\psi(\mathbf{r}') \tag{4.6}$$

$$E_{z,scat}(\mathbf{r}) = \int_{\Gamma} dl' \frac{\partial G(k - \|\mathbf{r} - \mathbf{r}'\|)}{\partial n(\mathbf{r}')}\psi(\mathbf{r}') \tag{4.7}$$

and the scattered one can be seen as a fictitious source function $\mathbf{K}(\boldsymbol{\rho})$, being $\boldsymbol{\rho}(\rho, \theta)$ a point on Γ. It is worth noting that in our two-dimensional case such $\mathbf{K}(\boldsymbol{\rho})$ has only a component on the xy plane. We can also notice that the current satisfying (4.6) radiates the scattered field in the exterior region so that on the outside surface of Γ we have that $E_{z,scat} = -E_{z,inc}$ and the scattered electric field is in the three-dimensional case is given by:

$$\mathbf{E}_{inc}(\vec{\rho}) = -\nabla \times \int_{\Gamma} dl' G(k\|\boldsymbol{\rho} - \boldsymbol{\rho}'\|)\mathbf{K}(\vec{\rho}') \tag{4.8}$$

which indeed coincides with (4.7) if we consider the two-dimensional case and we make $\mathbf{K} = \psi$. Another important consideration allows rewriting the Green function for the two-dimensional case as:

$$G(k|\mathbf{r} - \mathbf{r}'|) = iH_0^{(1)}(k\|\mathbf{r} - \mathbf{r}'\|) \tag{4.9}$$

where the right-hand side of the equation is defined by the Hankel function of the first kind of order zero. Now, the crucial point of the FMM method comes. Considering a sub-segment Γ' of Γ, the Hankel function can be expanded in terms of higher-order Hankel and Bessel functions:

$$H_0^{(1)}(k\|\mathbf{r} - \mathbf{r}'\|) = \sum_{m=-\infty}^{\infty} H_m^{(1)}(k\rho)J_m(k\rho')\exp(im(\theta - \theta')) \tag{4.10}$$

and, for a discretized source at r points located at $x'_j = (\rho'_j, \theta'_j), j = 1, 2, \ldots, r$, the scattered two-dimensional field is therefore rewritten as:

$$E_{z,scat}(\rho, \theta) = \sum_{m=-\infty}^{\infty}\sum_{j=1}^{r} i\frac{\partial J_m(k\rho'_j)\exp(-im\theta'_j)}{\partial n(x'_j)}H_m^{(1)}(k\rho)\exp(im\theta)K(x'_j)\Delta l'_j \tag{4.11}$$

where $\Delta l'_j$ is the discretized element of arc length containing the source $K(x'_j)$ and it is possible to truncate the infinite summation over m at N for a given accuracy, i.e.

to calculate only N multipole of the sources. As a result of the application of this method, the order of the number of operations is reduced from the usual quadratic one to $\mathcal{O}(N^{3/2})$. Moreover, it could be shown that if this process is applied iteratively the order can be further reduced to $\mathcal{O}(N^{3/4})$.

An alternative approach focused on the application of the FMM to the EFIE and the MFIE is described in [46]. Similarly to what was seen in the previous paragraph, we start from the subdivision of scatterers into groups, and then a representation of the scattered field as a wave emitted by the *center* of the union of a scatterer group is proposed by exploiting the addition theorem of Bessel functions. The interactions between groups can therefore be calculated, basing computations on the mutual geometrical distance. Finally, the addition theorem is again used to translate the scattered fields around the group center to its group members. Even in this case, the resulting formulas provide matrices whose memory-storage load is not quadratic as the original one, but it is of order $\mathcal{O}(N^{3/2})$. Moreover, a further method that considers the ray-propagation can be applied to the result of the FMM, making such a method even more efficient in terms of memory saving, thus finally obtaining a total number of stored elements of order $\mathcal{O}(N^{4/3})$.

4.2 Hierachical matrices

The $\mathcal{H}$-matrix method belongs to the set of geometrical approaches. Differently from the FMM, it is based on the rework of the structure of the matrix we are analyzing. This approach is discussed in detail in many papers, both from the analytical and from the empirical point of view. A wide contribution is given by [51, 52, 53, 54, 55, 56, 57]. Here a summary of the theory at the base of H-matrices is reported. Then, the theoretical discussion is applied to verify the difference in terms of the accuracy of the final result as a function of the reduction of the memory used for storing elements. For simplicity, we start the discussion with the analysis of the singular values of a function having the structure:

$$A_{ij} = \frac{1}{(i-j)^2 + \alpha} \tag{4.12}$$

where i, j can be seen as the elements a matrix $\mathbf{A}_{ij}$ which discretizes a domain $[0,1] \times [0,1]$ expressed by the matrix entries and α is an arbitrarily small constant. To determine the required singular values, we could proceed by applying the classic *Singular Value Decomposition* (SVD) to $\mathbf{A}$ or we could adopt a randomized version of it [58]. The standard SVD decomposition of a $m \times n$ matrix $\mathbf{A}$ provides a factorization of the form $\mathbf{A} = \mathbf{U}\mathbf{S}\mathbf{V}^T$ where $\mathbf{U}$ is a $m \times m$ orthogonal matrix of left singular values, $\mathbf{S}$ is an $m \times n$ diagonal matrix having entries coincident with the singular values of $\mathbf{A}$ in decreasing order and $\mathbf{V}$ is an $n \times n$ orthogonal matrix. The most important issue related to the application of this standard version concerns large-size matrices for which the computational cost could make the process unfeasible. In this sense, it is sometimes

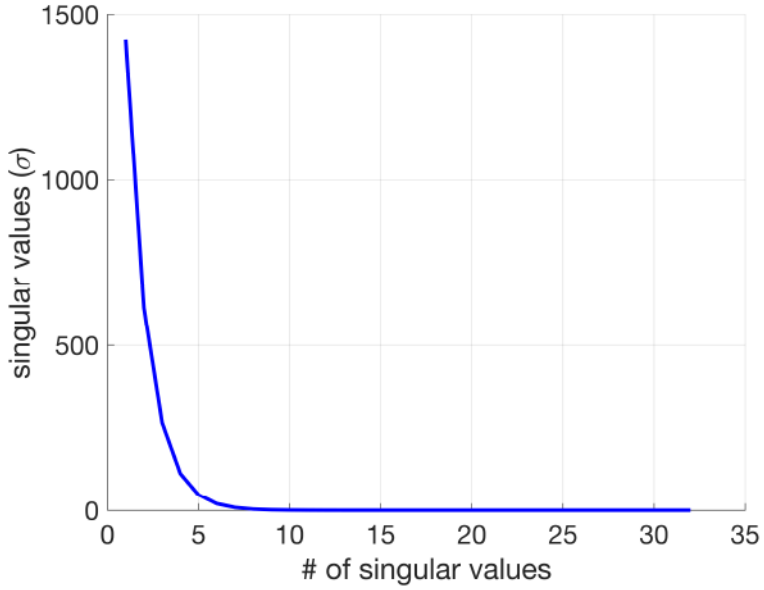

Figure 4.1: First 32 singular values of for a matrix $\mathbf{A}$ discretizing a domain $[0,1] \times [0,1]$ with 250 elements on each side and whose entries are of the form $1/[(i-j)^2 + \alpha]$ with $\alpha = 0.1$.

convenient to proceed with the decomposition of near-best rank matrix approximation. In this context, *random SVD* technique is adopted. Such a method is based on the standard Gaussian random vectors and on the matrix-vector product theory. We start by computing the products:

$$\begin{cases} \mathbf{y}_1 & = \mathbf{A}\mathbf{x}_1 \\ & \cdot \\ & \cdot \\ & \cdot \\ \mathbf{y}_{k+p} & = \mathbf{A}\mathbf{x}_{k+p} \end{cases} \tag{4.13}$$

where $\mathbf{x}_1, \ldots, \mathbf{x}_{k+p}$ are the standard Gaussian random vector named above with identically and independently distributed entries and $p \geq 1$ is an oversampling parameter. The second step requires the economized QR factorization $[\mathbf{y}_1, \ldots, \mathbf{y}_{k+p}] = \mathbf{QR}$. Last, the approximant $\mathbf{QQ}^T\mathbf{A}$ having rank $\leq k + p$ can be computed. Two observations about such structure should be reported: the first one concerns the fact that if $\mathbf{A}$ is symmetric, $\mathbf{QQ}^T\mathbf{A}$ can be simply computed by application of matrix-vector product involving $\mathbf{A}$. The second one regards the fact that the quality of the quality of the approximation is given by the Halko theorem [59] which states that, given $\mathbf{A}$ with the structure described above, $k \geq 1$ and $p \geq 4$, if we define $\Omega \in \mathbb{R}^{n \times (k+p)}$ a standard Gaussian matrix such that the economized QR decomposition is expressed by $\mathbf{QR} = \mathbf{A}\Omega$,

then, $\forall u, t \geq 1$:

$$\left\|\mathbf{A} - \mathbf{Q}\mathbf{Q}^T\mathbf{A}\right\| \leq \left(1 + t\sqrt{\frac{3k}{p+1}}\right)\sqrt{\sum_{j=k+1}^{n}\sigma_j^2(\mathbf{A})} + ut\frac{\sqrt{k+p}}{p+1}\sigma_{k+1}(\mathbf{A}) \tag{4.14}$$

where the norm at the left-hand side is a Frobenius norm, the failure probability is at most $2t^{-p} + e^{-u^2}$ and the best rank k approximation error to $\mathbf{A}$ in Frobenius norm is given by the squared tail of the singular values of $\mathbf{A}$ itself, i.e. the component of the right-hand side $\sqrt{\sum_{j=k+1}^{n}\sigma_j^2(\mathbf{A})}$. Two generalizations of the randomized SVD to multivariate Gaussian random vectors and to Hilbert-Schmidt operator allow to extend the field of application of such technique [58]. However, since these methods will not be taken into account in this thesis work.

Coming back to the analysis of the $\mathbf{A}$ whose entries are expressed by (4.12), since the modulus of its singular values decreases very fast (Fig. 4.1), we can hypothesize to introduce an alternative decomposition of $\mathbf{A}$ for which only a fewer number of elements of $\mathbf{S}$ are stored while small ones are neglected. Thus, supposing N the size of the problem and $r < N$ the number of elements we store, the final decomposition states:

$$\tilde{\mathbf{A}} = \tilde{\mathbf{U}}\tilde{\mathbf{S}}\tilde{\mathbf{V}}^{\top} \tag{4.15}$$

where the dimensions of the sub matrices are $\tilde{\mathbf{S}} = r \times r$, $\tilde{\mathbf{U}} = N \times r$, $\tilde{\mathbf{V}}^{\top} = r \times N$. In many reference papers, r is also known as the *effective rank* of the matrix, i.e. the number of non-negligible singular values, but it is not a priori defined and it has to be determined by specific procedures. An example involves the adoption of a *rank revealing method*. Such approaches consist of the computation of the effective rank of a matrix by choosing only singular values that overcome a certain threshold. A more specific example of a rank-revealing technique is well described in [60].

A different procedure for the determination of the effective rank of a matrix can be introduced in analogy to the *Adaptive Cross Approximation* method (ACA), which aims to memory saving during matrix storing proceeds. In particular, ACA belongs to the category of algebraic methods for the reduction of computational costs. Differently from physics-based methods which are in general more efficient in terms of both memory and CPU time, algebraic methods can be applied in general contexts and require only linear algebra to be applied, making it expressible by modular parts and easy to couple with the applications of the *Method of Moments*. Moreover, ACA in general does not require complete knowledge of the integral equations kernel, basis functions, or integral equation formulation. Concretely, ACA's CPU time requirements scale as $N^{4/3}\log N$. The essential code describing ACA, which is presented in [61] is here reported with the purpose of clarifying all the steps involved. Let's start from the introduction of the

matrix $\mathbf{Z}^{m\times n}$ which ACA aims to approximate by the matrix:

$$\tilde{\mathbf{Z}}^{m\times n} = \mathbf{U}^{m\times r}\mathbf{V}^{\top r\times n} = \sum_{i=1}^{r} \mathbf{u}_i^{m\times 1}\mathbf{v}_i^{1\times n} \tag{4.16}$$

where r is the effective rank of the matrix $\mathbf{Z}$ and $\mathbf{U}$, $\mathbf{V}$ are rectangular matrices coming from its decomposition. To assure that $\tilde{\mathbf{Z}}^{m\times n}$ provides a good approximation for the initial matrix, a test based on the *error matrix* $\mathbf{R}$ is adopted, meaning that for a given tolerance ε it must hold:

$$\left\|\mathbf{R}^{m\times n}\right\| = \left\|\mathbf{Z}^{m\times n} - \tilde{\mathbf{Z}}^{m\times n}\right\| \leq \varepsilon\|\mathbf{Z}\|^{m\times n} \tag{4.17}$$

where the norm symbol indicates the Frobenius one. Finally, to understand the passages of the pseudo-code in algorithm 1, four more definitions have to be introduced, namely $\mathbf{I} = \{I_1, \ldots, I_r\}$ and $\mathbf{J} = \{J_1, \ldots, J_r\}$ which identify respectively orderly selected row and column indexes of $\mathbf{Z}^{m\times n}$, $\mathbf{u}_k$ which is the kth column of $\mathbf{U}$ and $\mathbf{v}_k$ which is the kth row of $\mathbf{V}$. Therefore the ACA algorithm is described (adopting MATLAB® notation for vectors and matrices) by the following steps: It is worth noting that the algorithm requires only a partial knowledge of the original matrix, making this approach very efficient. Finally, since each step inside the kth iteration contains a $\mathcal{O}(r(m+n))$ operations and a total of r iterations have to be applied, the memory needed is $\mathcal{O}(r(m+n))$ while the CPU time scales as $\mathcal{O}(r^2(m+n))$.

We can then come back to (4.15), in order to check that the matrix $\tilde{\mathbf{A}}$ provides a good approximation for $\mathbf{A}$, the following inequality should be verified:

$$\frac{\left\|\mathbf{A} - \tilde{\mathbf{A}}\right\|}{\|\mathbf{A}\|} < \varepsilon \tag{4.18}$$

where ε is an arbitrarily small parameter that should reflect the precision threshold the operator desires. Thus, if the inequality is not verified, the number of stored singular values should be increased and the check should be applied again to the outcoming decomposition.

Now, the object of the analysis moves to the study of which blocks of the matrix can be saved in memory in the "convenient" way described above. In particular, we aim to determine which of the blocks of a matrix can be assumed to be *low-rank*. First, we can make an intuitive assumption: considering the element i, it's reasonable to hypothesize that the ones associated with a close index (e.g. $i\pm 1$) are also the ones close to i from a geometrical point of view, i.e. the ones feeling strongest mutual interaction according to formula (4.12). That's why we can also expect to find the highest values of the matrix along the diagonal blocks. However real situations almost always present a numeration of the elements which does not accomplish this consideration, meaning that the distance of the entries of the matrix $\mathbf{A}$ from the diagonal does not reflect the geometric distance between elements in the space and e.g. the index $i+1$ can be associated to an element

Algorithm 1 ACA algorithm:

Initialization:

1: initialize the first row index: I_1 and set $\tilde{\mathbf{Z}} = 0$;

2: initialize the first row of the approximate error matrix: $\tilde{\mathbf{R}}(I_1, :) = \mathbf{Z}(I_1, :)$;

3: find the first column index J_1 such that $\left|\tilde{\mathbf{R}}(I_1, J_1)\right| = \max_j(\left|\tilde{\mathbf{R}}(I_1, j)\right|)$;

4: $\mathbf{v}_1 = \tilde{\mathbf{R}}(I_1, :)/\tilde{\mathbf{R}}(I_1, J_1)$;

5: initialize the first column of the approximate error matrix: $\tilde{\mathbf{R}}(:, J_1) = \mathbf{Z}(:, J_1)$;

6: $\mathbf{u}_1 = \tilde{\mathbf{R}}(:, J_1)$;

7: $\left\|\tilde{\mathbf{Z}}^{(1)}\right\|^2 = \left\|\tilde{\mathbf{Z}}^{(0)}\right\|^2 + \|\mathbf{u}_1\|^2\|\mathbf{v}_1\|^2$;

8: find the second row index I_2 such that $\left|\tilde{\mathbf{R}}(I_2, J_1)\right| = \max_i(\left|\tilde{\mathbf{R}}(i, J_1)\right|)$, $i \neq I_1$;

kth iteration

9: update (I_k)th row of the approximate error matrix: $\tilde{\mathbf{R}}(I_k, :) = \mathbf{Z}(I_k, :) - \sum_{l=1}^{k-1}(\mathbf{u}_l)_{I_k}\mathbf{v}_l$;

10: find kth column index J_k such that $\left|\tilde{\mathbf{R}}(I_k, J_k)\right| = \max_j(\left|\tilde{\mathbf{R}}(I_k, j)\right|)$, $j \neq J_1, \ldots, J_{k-1}$;

11: $\mathbf{v}_k = \tilde{\mathbf{R}}(I_k, :)/\tilde{\mathbf{R}}(I_k, J_k)$;

12: update (J_K)th column of the approximate error matrix: $\tilde{\mathbf{R}}(:, J_k) = \mathbf{Z}(:, J_k) - \sum_{l=1}^{k-1}(\mathbf{v}_l)_{J_k}\mathbf{u}_l$;

13: $\mathbf{u}_k = \tilde{\mathbf{R}}(:, J_k)$;

14: $\left\|\tilde{\mathbf{Z}}^{(k)}\right\|^2 = \left\|\tilde{\mathbf{Z}}^{(k-1)}\right\|^2 + 2\sum_{j=1}^{k-1}\left|\mathbf{u}_j^\top\mathbf{u}_k\right| \cdot \left|\mathbf{v}_j^\top\mathbf{v}_k\right| + \|\mathbf{u}_k\|^2\|\mathbf{v}_k\|^2$;

15: check convergence: if $\|\mathbf{u}_k\|\|\mathbf{v}_k\| \leq \varepsilon\left\|\tilde{\mathbf{Z}}^{(k)}\right\|$, end iteration;

16: find the next row index I_{k+1} such that $\left|\tilde{\mathbf{R}}(I_{k+1}, J_k)\right| = \max_i(\left|\mathbf{R}(\tilde{i}, J_k)\right|)$, $i \neq I_1, \ldots, I_k$.

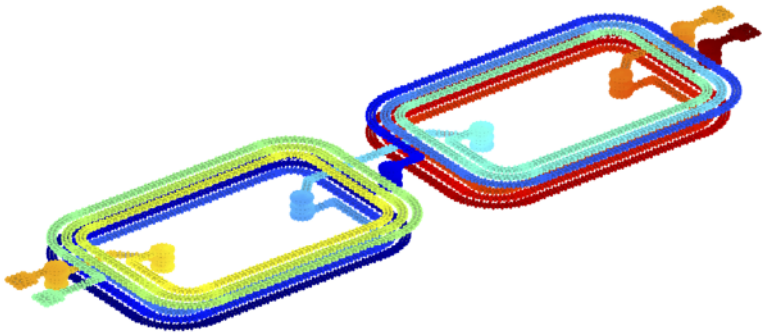

(a) Original index set.

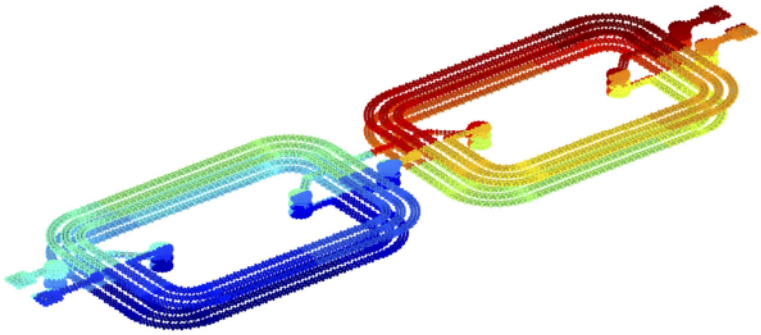

(b) Reordered index set.

Figure 4.2: Example of reordering of DOFs indices for an inductor with the bisection algorithm.

which is far from the one associated to i. Hence a preprocessing operation aiming to reorder the number of elements should be implemented before proceeding with the identification of the low-rank blocks.

At the same time, thanks to such preprocessing, we can assure the diagonal blocks of the matrix to be high-rank. Finally the preprocessing not only makes the analysis much easier and faster, but it is fundamental in making the compression process work because otherwise, it is not possible to identify a regular scheme in the position of the entries of the matrix. Fig. 4.2 shows a detailed example of how a reordering process reorganizes the numeration of DOFs. Intuitively, elements having similar color tones are also associated with close indices.

Once the renumbering of the elements is performed, the purpose of the analysis is to understand how the low-rank blocks should be saved. Hence we start implementing a bisection algorithm so that the rows and the columns of the matrix are split into two halves, $I_1 = \{1, \ldots, N/2\}$, $I_2 = \{N/2, \ldots, N\}$ along the vertical direction and $J_1 = \{1, \ldots, N/2\}$, $J_2 = \{N/2, \ldots, N\}$ along the horizontal one, so that a total of four blocks are obtained. Moreover, the off-diagonal blocks, i.e., the ones which are in principle low-rank, are the ones associated with the Cartesian product $I_2 \times J_1$ and $I_1 \times J_2$. It is worth noticing that calling e.g. $\mathbf{M} = I_2 \times J_1$ the decomposition performed

as:

$$\mathbf{M} = \mathbf{U}\mathbf{V}^T \tag{4.19}$$

provides two matrices having one of the dimensions whose number of elements is very small, hence reducing the total cost for storing both of them. In some reference works a matrix built as $\mathbf{M}$ is denoted as $\mathbf{R}r$-matrix and is considered as the main low-rank structure of an $\mathcal{H}$-matrix.

In principle, a subdivision of each single cluster can be iteratively performed until the smallest block possible is obtained, i.e. the one constituted by a single entry of the original matrix. Such a scheme is summarized in Fig. 4.3, where a tree structure is obtained from the application of the bisection algorithm. The last step of the process provides the *leaves* of the tree.

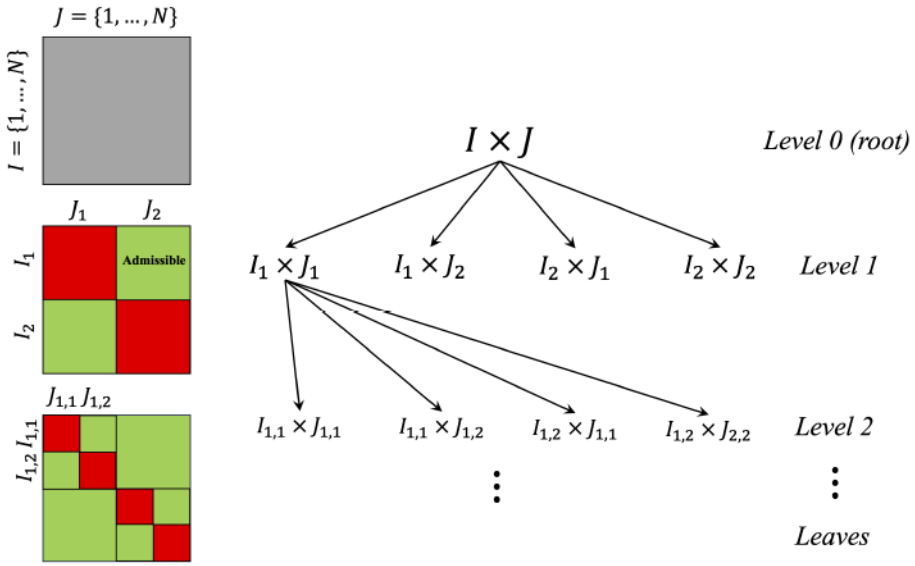

Figure 4.3: Example of the application of a bisection algorithm following a block-tree decomposition for the subdivision of the original matrix.

We wish to find out at what level of the tree we can assume a block to be low-rank. Let's suppose to associate the subset I_i or J_j (i.e. a discrete subset of entries of the original matrix, obtained at any iteration of the bisection process) with an element coming from the discretization of the domain. Specifically, looking at Fig. 4.4, I_i represent the indices of geometric entries in Ω_s and J_j represent the indices of geometric entries in Ω_t. The *admissibility criterion* for low-rank matrices is based on the definition of functions that evaluate the *diameter* of considered elements, i.e. the maximum distance between points belonging to that element e.g., diamI_i, diamJ_i. Since such points are all contained inside the cluster representing the element itself, the problem can be expressed as a function of the cluster instead of the element. Moreover, we have to introduce also the *distance between elements*, that is dist(I_i, J_j), which is considered as the distance between the central points of the elements themselves. Finally, the

above-mentioned criterion states:

$$\min\{\text{diam}(I_i), \text{diam}(J_j)\} \leq \eta \text{dist}(I_i, J_j) \tag{4.20}$$

where η is an arbitrary parameter that is chosen by the user and which defines "how much" each block has to be low-rank. Such criterion should then be applied to each block obtained from the cluster-tree subdivision. When a block does not satisfy it, a further bisection of the block itself has to be performed. In this way, we ensure the storage of more elements for blocks providing a greater contribution to the total matrix, i.e. high-rank blocks. That's the reason why diagonal blocks, in general, do not satisfy the admissibility criterion at the first iterations: since they are the ones with the highest rank, the user should want to store as many elements as possible from them, trying to neglect as many as possible from off-diagonal ones. Obviously, as η increases, the criterion is less restrictive and so it is easier for a block to accomplish it, making the method store much fewer elements, but obtaining a less precise approximation of the total matrix.

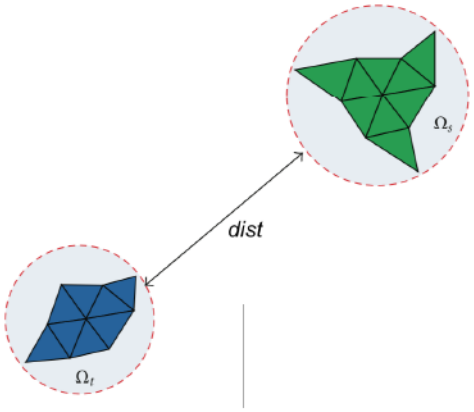

Figure 4.4: Graphical representation of the admissibility criterion between a source element Ω_s and a target one Ω_t.

The method described until now is also known as *Cluster Tree Partitioning* because of its structure based on progressive bisection of the elements along rows and columns. In summary, the function implementing such method has a total of three main parameters which have to be defined by the user and which determine the order of accuracy of the model. The first one is ε which is needed to impose how much the approximated matrix is different from the initial one. The second parameter is η and is related to the admissibility criterion for knowing if a block has a low rank. The last one is the block size the user wishes to have at the end of the process.

One final consideration regards the computation of the entries of the reduced matrix. Indeed, if they were computed at the beginning of the process or during each iteration of the cluster-tree subdivision, the computational cost would be dramatically increased. On the other hand, following this reasoning, only the last step is dedicated to this

process and it requires the definition of a simple function handle whose variables are the indices of the source and of the target elements. This way the computational cost is consistently reduced.

Many different libraries for the implementation of *hierarchical matrices* were written for many different coding languages. Two important examples are **HLIBpro** and **Strumpack**, which are both written using C and C++ but both provide a good interface for MATLAB® or Fortran. About MATLAB® written libraries, the most important one is **hm-toolbox** which computes $\mathcal{H}$ matrices adopting three different approaches for the construction of the cluster-tree structure:

- *hierarchically semi-separable* or **HSS**, based on the idea of identifying low-interacting terms inside each block;
- *hierarchically off-diagonal low-rank* or **HODLR**, based on the bisection only of diagonal terms, while off-diagonal elements are assumed to have low mutual interaction and so to have also low enough rank;
- *hierarchically adaptive low-rank* or **HALR**, very similar to HODLR but applying the cluster tree subdivision to all the blocks, independently of their position inside the matrix. They are more general than HODLR because they can be applied to any kind of matrix, independently of the way they were composed.

These methods will be adopted in the following section to perform numerical analysis which aims to compare the differences in terms of memory and CPU time requirements and in terms of the accuracy of the representation of the initial matrix. Some general considerations that regard the $\mathcal{H} - matrix$ approach involve the number of elements of the final matrix, which scales no longer quadratically with the number of DOFs, but it can be reduced to $O(N \log N)$. Another remarkable observation regards the canonical operations for matrices. Indeed a whole new algebra for $\mathcal{H}$-matrices needs to be introduced. [62]. This way the summation between matrices, the matrix-vector product, and the matrix inversion are still well defined. A brief theoretical discussion about these algebraic operators is reported here. A more in-depth point of view can be found in [63, 64].

First, we need to talk about the matrix-vector product involving an $\mathbf{R}r$-matrix, suppose $\mathbf{M} = \mathbf{U}\mathbf{V}^\top$. We aim to define an operator such that $\mathbf{x} \to \mathbf{y} := \mathbf{M}\mathbf{x}$. This operation is simply split into two steps: the first computes a dummy vector $\mathbf{z} = \mathbf{V}^\top\mathbf{x}$ while the second provides the searched result

$$\mathbf{y} = \mathbf{U}\mathbf{z} \tag{4.21}$$

Secondly, the addition for $\mathbf{R}r$-matrices should be introduced. Hence, let's consider $\mathbf{M}_1 = \mathbf{U}_1\mathbf{V}_1^\top$ and $\mathbf{M}_2 = \mathbf{U}_2\mathbf{V}_2^\top$. The summation is a $\mathbf{R}2r$-matrix defined as:

$$\mathbf{M}_1 + \mathbf{M}_2 = [\mathbf{U}_1\ \mathbf{U}_2][\mathbf{V}_1\ \mathbf{V}_2]^\top \tag{4.22}$$

In a similar way we can also define a formatted addition between two distinct $\mathbf{R}r$-matrices and associated to the symbol $\oplus$ as the best approximation in both spectral and Frobenius norm of their sum, meaning that it satisfies (4.18).

Finally, the last basic operation we need to define is the multiplication between an $\mathbf{R}r$-matrix and a general one $\mathbf{A}$. The solution is again an $\mathbf{R}r$-matrix and is obtained by the succession of two following steps as before:

$$\mathbf{MA} = \mathbf{UV}^\top\mathbf{A} = \mathbf{U}(\mathbf{A}^\top\mathbf{V})^\top \tag{4.23}$$

$$\mathbf{AM} = \mathbf{AUV}^\top = (\mathbf{AU})\mathbf{B}^\top \tag{4.24}$$

Once all the basic operations are defined for the low-rank clusters, we can extend such considerations also to $\mathcal{H}$-matrices. In fact an $\mathcal{H}$-matrix is in general obtained from sub-blocks which can be either represented as $\mathbf{R}r$-matrices or as leaves of the graph which do not need specific structure, in the algorithms denoted as "unstructured". We proceed with the description of the same operations presented for the low-rank clusters following an identical sequence, so the first one is the matrix-vector multiplication. Let's assume $\mathbf{H}$ to be an $\mathcal{H}$-matrix and let's define the set of the sons of a subset of indices J as $S(J)$. The matrix-vector product $\mathbf{y} := \mathbf{y} + \mathbf{Hx}$ is then defined by the algorithm 2 which provides the searched product in each leaf of the block tree.

Algorithm 2 Matrix-vector product for $\mathcal{H}$-matrix:

```
if S(J × I) ≠ ∅
    if J' × I' ∈ S(J × I)
        MVM(H, J' × I', x, y);
    end
else
    y|_J := y|_J + H|_{J×I} x|_I (unstructured or Rr-matrix)
end
```

The addition operation requires instead the assumption of three different $\mathcal{H}$-matrices, $\mathbf{H}$, $\mathbf{H}^{(1)}$, $\mathbf{H}^{(2)}$, such that the summation $\mathbf{H} := \mathbf{H}^{(1)} + \mathbf{H}^{(2)}$ is still an $\mathcal{H}$-matrix with block-wise rank $2r$. Alternatively, if we need the *formatted* version seen above, the formulation states $\tilde{\mathbf{H}} := \mathbf{H}^{(1)} \oplus \mathbf{H}^{(2)}$ and the implementation is described in algorithm 3, where the *formatted summation* described for $\mathbf{R}r$-matrices was adopted.

Algorithm 3 Addition between $\mathcal{H}$-matrices:

```
if S(J × I) ≠ ∅
    if J' × I' ∈ S(J × I)
        sum(H̃, J' × I', H^(1), H^(2));
    end
else
    H̃|_{J×I} := H^(1)|_{J×I} ⊕ H^(2)|_{J×I} x|_I (unstructured or Rr-matrices)
end
```

To introduce the multiplication between matrices we need again three distinct $\mathcal{H}$-matrices $\mathbf{H}$, $\mathbf{H}^{(1)}$, $\mathbf{H}^{(2)}$. About the usual dot product $(\cdot)$, the formulation $\mathbf{H} = \mathbf{H} + \mathbf{H}^{(1)} \cdot \mathbf{H}^{(2)}$ is defined under moderate assumptions and it turns out to give again an $\mathcal{H}$-matrix with complexity $\mathcal{O}(r \log(N))$. On the other hand, about the *formatted product*, the relative expression states $\tilde{\mathbf{H}} = \mathbf{H} \oplus \mathbf{H}^{(1)} \odot \mathbf{H}^{(2)}$. This operator is defined starting from the *formatted addition* for $\mathbf{R}r$ sub-blocks and is applied to three distinct cases:

- $\boxplus = \boxplus \odot \boxplus$: all the blocks are subdivided and the addition is performed inside the sub-blocks;
- $\boxplus = \square \odot \boxplus$: the target matrix is subdivided and (at least) one of the factors is not; then one of the factors has rank equal to the maximum between r and the maximum rank of the leaves of the tree. The low-rank products have to be computed adopting the multiplication between matrices defined for $\mathbf{R}r$ blocks and then it must be summed to the target matrix;
- $\square = \boxplus \odot \boxplus$: the target matrix is not subdivided; then a specific algorithm (5) must be implemented.

All these cases are summarized in algorithm 4, where K is assumed to be another subset of indices just like J and I.

Algorithm 4 Multiplication between $\mathcal{H}$-matrices:

```
if S(J × K) ≠ ∅ and S(K × I) ≠ ∅
{Case 1: All matrices are subdivided :}
    if J' ∈ S(J), K' ∈ S(K), I' ∈ S(I)
        MulAdd(H̃, J', K', I', H^(1), H^(2));
    end
    if S(J × I) ≠ ∅
{Case 2: Target matrix is subdivided :}
        Compute H' := H^(1)|_{J×K} H^(2)|_{K×I}
        Sum H' to H̃|_{J×I}
    end
else
{Case 3: Target matrix is not subdivided :}
    Follow algorithm 5
end
```

In any of the presented situations which can verify for the *formatted multiplication* the order of complexity is $\mathcal{O}(Nr^2\log(N)^2$.

One further important operation which was not treated for $\mathbf{R}r$-matrices is necessary to complete the outlining of the algebra for $\mathcal{H}$-matrix, i.e. the inversion of a 2×2 block $\mathcal{H}$-matrix. The stardar inverse can be computed when through the Schur complement when the matrix is e.g. positive definite. About the *formatted* counterpart, the exact sums and products are substituted by the respective *formatted* operators $\oplus, \odot$ and the algorithm 6 holds.

Algorithm 5 MulAddRk for $\mathcal{H}$-matrices:

if $S(J \times K) = \emptyset$ or $S(K \times I) = \emptyset$
  Compute $\mathbf{H}' := \mathbf{H}^{(1)}|_{J\times K}\mathbf{H}^{(2)}|_{K\times I}$
  Sum $\mathbf{H}'$ to $\tilde{\mathbf{H}}|_{J\times I}$ (formatted addition)
end
if $J' \in S(J)$, $I' \in S(I)$
  Initialise $\mathbf{H}'|_{J',I'} = 0$
  if $K' \in S(K)$
    MulAddRk($\mathbf{H}'|_{J',I'}, J', K', I', \mathbf{H}^{(1)}, \mathbf{H}^{(2)}$ ($\mathbf{H}'|_{J',I'}$ is smaller than $\mathbf{H}$ and extended by zeros)
    $\tilde{\mathbf{H}} := \mathbf{H} \oplus \sum_{J'\in S(J)} \sum_{I'\in S(I)} \mathbf{H}'|_{J\times I}$
  end
end

Algorithm 6 Inverse of 2×2 block $\mathcal{H}$-matrices:

if $S(J \times K) = \emptyset$
  Compute the exact inverse of $\tilde{\mathbf{H}}' := \mathbf{H}^{-1}$ (for small matrices)
else
  $\left\{ S(J) = \{J_1, J_2\}, S(I) = \{I_1, I_2\}, \mathbf{H} = \begin{bmatrix} \mathbf{H}_{11} & \mathbf{H}_{12} \\ \mathbf{H}_{21} & \mathbf{H}_{22} \end{bmatrix} \right\}$
  Invert $(\mathbf{Y}, J_1, I_1\mathbf{H}|_{J_1\times I_1})$
$\mathbf{S} := \mathbf{H}_{22} \ominus (\mathbf{L}_{21} \odot (\mathbf{Y} \odot \mathbf{H}_{12}))$
  Invert $(\tilde{\mathbf{H}}|_{J_2\times I_2}, J_2, I_2\mathbf{S})$
  $\tilde{\mathbf{H}}|_{J_1\times I_1} := \mathbf{Y} \oplus (\mathbf{Y} \odot (\mathbf{H}_{12} \odot (\tilde{\mathbf{H}}|_{J_2\times I_2} \odot (\mathbf{H}_{21} \odot \mathbf{Y}))))$
  $\tilde{\mathbf{H}}|_{J_1\times I_2} := -\mathbf{Y} \odot (\mathbf{H}_{12} \odot \tilde{\mathbf{H}}|_{J_2\times I_2})$
  $\tilde{\mathbf{H}}|_{J_2\times I_1} := \mathbf{H}_{12} \odot (\mathbf{H}_{21} \odot \mathbf{Y})$
end

One last fundamental operation which has to be defined in analogy with its counterpart for the classic matricial algebra involves the LU factorization, which can be indeed performed also for $\mathcal{H}$-matrices. Such decomposition allows both to compute the direct solution of linear systems through substitutions, as well as constructing an incomplete preconditioner to speed up the resolution of the problem. The latter can be effectively utilized in iterative solvers like the Generalized Minimal Residual (GMRES) method.

It can be observed that for each named operation the requirement in terms of both CPU time and memory is consistently diminished when implemented for an $\mathcal{H}$-matrix concerning the corresponding dense matrix. The following section will be fully dedicated to investigate these aspects.

In conclusion, a graphical example of the framework of an $\mathcal{H}$-matrix obtained using the HALR approach is represented in Fig.4.5. The red blocks represent fully-populated non-admissible blocks, which need either to be further decoupled or to be stored with a considerable number of elements since they are high-rank. Light green blocks, satisfy the admissibility criterion and hence they can be assumed as low-rank blocks and they can be stored using an exiguous number of entries. The integer value printed inside each of them is the effective rank of the resulting decomposition (4.19).

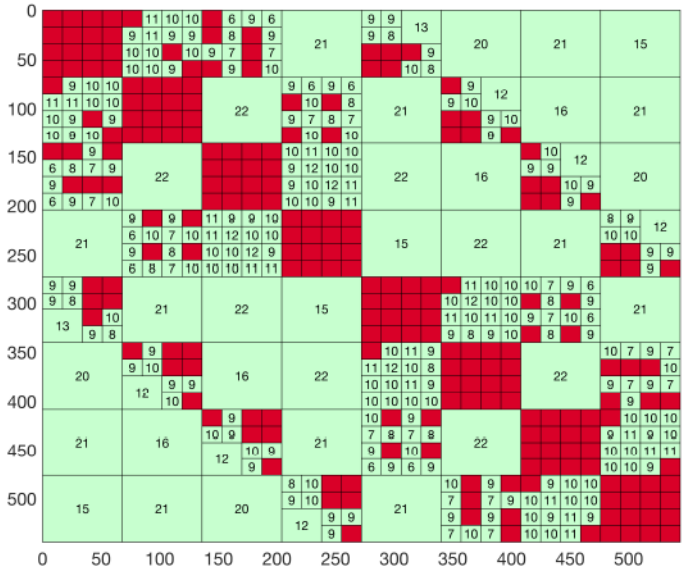

Figure 4.5: Example of $\mathcal{H}$-matrix pattern.

4.2.1 Numerical comparison of data-sparse representations

We want to analyze the behavior of the $\mathcal{H}$-matrices generated by HSS, HODLR and HALR methods. The example we will implement considers a sphere subjected to an external magnetic induction field. The solution of the induced current over the surface is solved by the magneto-quasistatic, i.e. by coupling the EFIE formulation with the

null divergence of the electric current. The problem is described by the linear system:

$$\begin{bmatrix} \mathbf{R} + i\omega\mathbf{L} & \mathbf{D}^\top \\ \mathbf{D} & \mathbf{0} \end{bmatrix} \begin{bmatrix} \mathbf{j}_e \\ \mathbf{\Phi}_e \end{bmatrix} = \begin{bmatrix} \mathbf{U}_s \\ \mathbf{I}_s \end{bmatrix} \tag{4.25}$$

where the resistance value is $\rho = 1/5.6 \cdot 10^7$ and the unknowns of the problem are the potentials $\mathbf{\Phi}_e$ and the surface current DOFs $\mathbf{j}_e$. This test case was chosen since the exact solution is known from the analytical point of view, as described in detail in Section 3.6. In particular, this analysis is performed to verify if the adoption of any of the $\mathcal{H}$-matrix shows an overall convenience or less. The comparison is made only between the analytical and the obtained current density. It is reported that the total number of DOFs for $\mathbf{j}_e$ is 4212 while for $\mathbf{\Phi}_e$ is 2808. Hence the upper-left block is 4212×4212, the lower-right block has dimension 2808×2808 and the off-diagonal rectangular clusters have dimension $\mathbf{D} = 2808 \times 4212$. The total time needed for the computation of the exact solution using the dense matrix and the simple backslash solver is ≈ 225 seconds.

First, the necessary preprocessing involving the reordering of the DOFs is performed as described in the previous section. The result of such a procedure is summarized in Fig.4.6. Such reordering has to be implemented for each block $\mathbf{L}, \mathbf{R}$ and $\mathbf{D}$, independently of their properties.

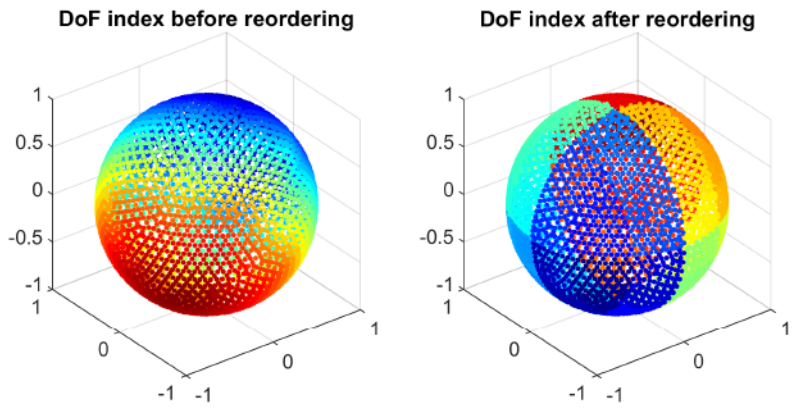

Figure 4.6: Preprocessing of reordering of DOFs for the examined problem.

The second step considers the computation of the $\mathcal{H}$-matrix for $\mathbf{L}$ adopting each method named in the first paragraph. We focus on such block since both $\mathbf{R}$ and $\mathbf{D}$ turn out to be very sparse so the compression is not needed. Furthermore, it is worth noting

that in general, it is much inconvenient to compute the full dense matrix and then to compress it. Such an approach is here adopted only because the size of the problem is particularly small and we aim to analyze a problem whose analytical solution is well known. Indeed, as we have highlighted in the previous section, only the last step of the construction of an $\mathcal{H}$-matrix is dedicated to the computation of the entries from a given function handle, and we do not start from a pre-constructed dense matrix. The lines of code for calling each type of method belonging to the hm-toolbox are reported in the Algorithm 7. Indeed, many different ways for calling each method are implemented in

Algorithm 7 $\mathcal{H}$-matrix call:

$\mathbf{HL} = \mathrm{hss}(L);$

$\mathbf{HL} = \mathrm{hodlr}('handle', Afun, M, N);$

$\mathbf{HL} = \mathrm{halr}('handle', Afun, M, N, 'cluster', \ldots);$

the hm-toolbox. They are based on the knowledge we have about the original matrix (e.g. if it is symmetric or less if its entries can be expressed by a Cauchy distribution...) and on the characteristics we want to impose on the final $\mathcal{H}$-matrix (e.g. its maximum or minimum dimensions). Furthermore, we always could define the cluster structure that has to be followed, otherwise, the default one is assumed by the software. In our case, HODLR and HALR exploit the definition of a handle function $Afun$ to construct the final matrix by the ACA strategy. M, N are the number of rows and columns of the initial matrix. In the particular case of HALR, the cluster structure is also specified as an input of the function. About the HSS, it is implemented using the standard call of the hm-toolbox after the proper reordering of the entries of $\mathbf{L}$. Let's note once again that the structure implemented for the HSS method is never used in a practical context since it would require the full structure of the dense matrix. However, because of the impossibility of adopting the same structure as the other two methods, this analysis is performed for the sake of completeness. Finally, for each method, four additional options should be properly introduced. The first one consists of the definition of the sizes of the reduced blocks. The second one requires a threshold for off-diagonal truncation and we arbitrarily assume it as equal to 10^{-9}. The third one consists in the definition of the adopted compression method which can be either the QR factorization or the SVD one; for the solution of our test case, we opt for the latter one. Finally, the fourth option asks for the definition of the norm for the truncation, which in our case coincides with the Frobenius one.

As anticipated in the theoretical section, a completely new algebra should be defined for $\mathcal{H}$-matrices, and this case is no different. The solution of the linear problem is computed thanks to the application of the GMRES method (whose input will be briefly introduced later), after a proper introduction of a new kind of matrix-vector product. It can be proved that the matrix-vector product is indeed much faster if it involves

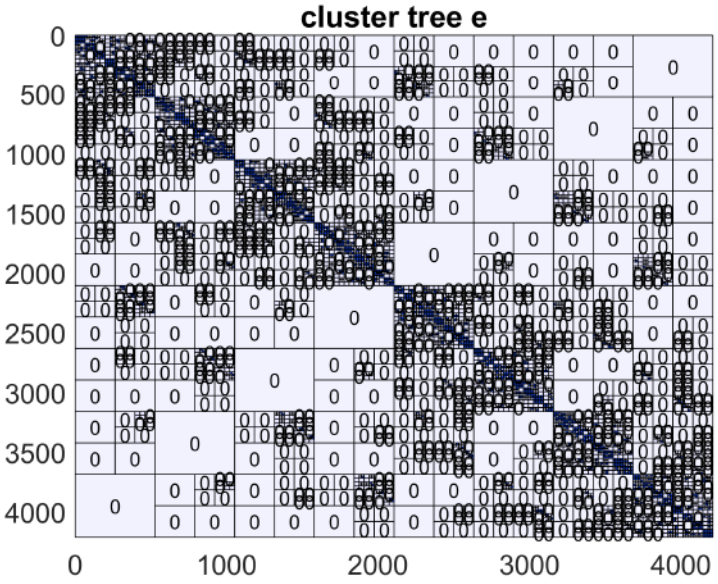

Figure 4.7: Cluster final structure for matrix $\mathbf{L}$. In this representation the number printed inside each block is not related to their effective rank r, indeed only the shape of the blocks partition is important for the clustering.

a matrix obtained after the compression proceeds. However, the operations defined for the new algebra require, as for the canonical one, the matching of the sizes of the tensorial quantities involved. As a consequence, a proper product rule is introduced, which is based on the multiplication of matrices and vectors block-by-block.

About the results obtained from the application of the methods, we can observe that the compression of the matrix $\mathbf{L}$ of dimension 4212×4212 provides leaves having a minimum dimension equal to 16 entries of the original matrix, while the maximum dimension corresponds to 17 of them. The cluster structure obtained from such reasoning is presented in Fig. 4.7. Here, the squares identified with a zero are intuitively assumed as total zero blocks. Blue-filled squares are instead considered high-rank blocks and saved with a proper number of entries.

Before solving the system with the reduced block $\mathbf{L}$, a preconditioner is implemented for the total matrix, aiming to make the computation of the solution much faster. In particular, it was verified that a preconditioner based on the LU factorization of the Schur complement of the block matrix is the most effective. In this specific case, such a factor assumes the form:

$$\mathbf{S} = -\mathbf{D}(\mathbf{R} + i\omega\mathbf{L})^{-1}\mathbf{D}^{\top} \tag{4.26}$$

One further simplification was implemented by considering the components in brackets: if we can hypothesize that the main contributions for $\mathbf{HL}$ and $\mathbf{R}$ are disposed along the diagonal, we can also suppose to identify both of them with their respective diagonal. In this way, we can refer to the whole upper-right block with a simple vector,

Method	HSS	HODLR	HALR
Compression [%]	21.81	49.94	92.23
Compression time [s]	52.73	19.33	10.40
Solution time[s]	4.16	2.45	1.24
Relative error [%]	$4.8 \cdot 10^{-4}$	$4.8 \cdot 10^{-4}$	1.05

Table 4.1: Comparison of memory saved and CPU time gained adopting computation of $\mathcal{H}$-matrix and solution of the problem with the reduced matrix.

which does not require a huge quantity of memory to be stored, even for big-size problems. Furthermore, this operation makes the computation of the inverse much easier and faster. One further consideration that is taken into account before proceeding with the resolution of the problem regards the fact that the incidence matrix $\mathbf{D}$ is in general composed of linearly dependent rows and columns. To solve this issue, one potential is removed from the right-hand side vector described in (4.28). At the same time also a row of the incidence matrix itself is deleted to avoid the singularity which otherwise would characterize the total matrix. The solution to the problem is computed by adopting the GMRES solver implemented with a tolerance of 10^{-6}, 80 inner iterations/restart iterations, and a total maximum of iterations equal to 20. Two more inputs are given by the matrix expressing the problem, which is obtained from the vector-product multiplication block-by-block involving the four main clusters, and by the preconditioner.

The final results are summarized in table 4.1. The percentage of compression of the $\mathbf{L}$ block is computed as:

$$\text{compression ratio} = \left(1 - \frac{\text{size}(\mathbf{HL})}{\text{DOFs}(\mathbf{j})^2 \cdot 16}\right) \cdot 100\% \tag{4.27}$$

and we can deduce that it is increasing from 0 to 99% as the number of entries of the cluster diminishes. About the relative error committed in estimating the solution by solving the system with $\mathbf{HL}$, the formulation which describes its value is:

$$\epsilon_{rel} = \frac{\|\mathbf{x} - \mathbf{x}_{exact}\|}{\|\mathbf{x}_{exact}\|} \tag{4.28}$$

where $\mathbf{x}$ is the total solution of the system, but we focus in particular on the current term $\mathbf{J}_e$. Again, we can notice that its value lies inside the range $[0-99]\%$ (0 associated with the exact analytical solution, and increasing as we move away from it). Finally, the times reported in table 4.1 is computed adopting the function "tic-toc" of MATLAB®. At first sight, it is immediately noticed that each method requires a total CPU time (sum of the one for the compression of $\mathbf{L}$ and the one for solving the system) which is remarkably lower than the one required for solving the fully dense system. This convenience is also stressed by observing that the relative error concerning the analytical solution is very small (at most $\approx 1\%$) despite the reduction of the number of stored

Method	HSS			HODLR		
Threshold (ε)	10^{-7}	10^{-5}	10^{-3}	10^{-7}	10^{-5}	10^{-3}
Compression [%]	51.87	74.00	89.10	59.75	73.56	82.15
Compression time [s]	32.52	17.77	8.83	11.60	2.47	1.70
Solution time [s]	2.24	1.01	0.42	1.88	1.26	0.76
Relative error [%]	$4.8 \cdot 10^{-4}$	$1.4 \cdot 10^{-3}$	$1.9 \cdot 10^{-1}$	$4.8 \cdot 10^{-4}$	$1.1 \cdot 10^{-3}$	$8.7 \cdot 10^{-2}$

Table 4.2: Comparison between methods adopting different values for the thresholds.

entries. If we analyze in more detail in table 4.1, we can notice that the most efficient method turns out to be the HALR. Indeed, once we adopted the same threshold for the cluster-tree decomposition, such an approach provides a much more consistent compression of matrix $\mathbf{L}$, also requiring less time to perform both the compression and the computation of the solution of the linear system. That's why, supposing 1.05% a sufficiently small relative error, we can state that HALR offers in general the best performances.

It is then reasonable to ask how much the threshold impacts this analysis. Therefore one more analysis is carried out, varying both HSS and HODLR thresholds in the range $[10^{-7} - 10^{-3}]$ to try to come closer to the order of compression of HALR. The results are summarized inside table 4.2. As we could expect from the theoretical analysis of the $\mathcal{H}$-matrices in the previous section, when we increase the value of the threshold we also allow the ratio in (4.18) to be larger, and then approximation matrix to verify the inequality even storing a lower number of entries. It directly follows why the total percentage of compression increases as we increment the threshold. It is also interesting to notice that the order of increment of the percentage of compression for the HSS is greater than the one of the HODLR, at the expense of the CPU time needed for computing both the compression of the matrix and the solution of the problem. Finally, it is immediate to deduce that, as we increase the order of the approximation of $\mathbf{L}$, we also increase the error in estimating the analytical solution. Therefore, despite the certain advantage that the implementation of an $\mathcal{H}$-matrix provides, it is necessary to find a compromise between the memory and the CPU time saved by adopting any of the presented methods, and the total committed error, compatibly with the required degree of precision one desires. This section then works as an investigation of the various possibilities that could be adopted, with their respective pros and cons.

Some final considerations regard the implementation of some alternative techniques which are discussed for completeness only from the theoretical point of view and will not be considered in the following numerical analysis. First, about the adopted preconditioner, many different - and possibly more efficient than the LU factorization - ones could be adopted. It's e.g. the case of the *Algebraic Multigrid* preconditioner (AMG) [65, 66]. Introduced at the start of the '80s, during the years the AMG was improved many times, to search for a way to make it as "scalable" as possible. This adjective is associated with methods whose required time for solving a problem remains essentially constant with the increment of both the problem size and the computing resources.

Nowadays AMG provides a very fast alternative among all the preconditioners. Differently from standard *Multigrid methods* for which the central idea is to make the relative error as small as possible by refinement of the grid, the AMG constructs the reduced matrix only using information about from the original matrix.

Another interesting consideration regards the application of the $\mathcal{H}$-matrices approach itself. In principle, it would have been possible to consider the whole matrix summarizing the problem as the input for any of the methods assumed from the hm-toolbox. Such proceed would have dramatically reduced the total time for the computation of the solution thanks to the definition of the new algebra, specifically the LU decomposition. Nevertheless, the compression through $\mathcal{H}$-matrix technique of the whole 2×2 total matrix would have sparsified blocks that were already sparse, thus reducing the effectiveness of the reduction method. Since the analyzed problem is small and the compression of the only $\mathbf{L}$-block is assumed to be overall convenient in terms of CPU time required, this approach was then avoided.

Chapter 5

Conclusions

This thesis work had the main scope to investigate the advantages of the application of *Integral Equations*, with specific attention to *Surface* ones, concerning the classic *Finite Element Method*. After a suitable introduction of all the tools we needed, a theoretical description concerning how to solve the problem was given, stressing the pros and cons of this technique. Then, many different semi-analytical approaches were introduced to provide some useful and different tools to solve the theoretical issues related to the singularities appearing in the formulation of the problem. These methods were first tested against a classic fully numeric approach based on the definition of an increasing number of Gauss points.

The most recent technique that was implemented regarded the *Modified Line Integral method*, which showed its effectiveness in approximating the exact results. In particular, this method turned out to be an optimal alternative to fully numeric approaches, which otherwise require a huge number of quadrature points to reach a satisfying approximation degree concerning the exact solution, making the computation load too heavy. The results computed with the *Modified Line Integral* method were tested against the solution of a PEC sphere subjected to a specific electric field. Such a test case is well known from the state of the art since the RCS solution of a PEC sphere is known analytically. It was observed that such a semi-analytic method replicates very well the behavior of the exact solution. However, it was also noticed that the problem expressed in terms of *Surface Integral Equations* should be properly addressed if we want to keep bounded the load for solving it.

Last, a section fully dedicated to the acceleration of integral equations was reported. Here, different methods for the compression of dense matrices were described from the theoretical point of view. The core of such a section is the discussion of *Hierarchical matrices*, with the definition of a proper new algebra associated with them. To verify the effectiveness of such a method, the final part of the section was dedicated to its implementation through different codes. In particular, it was observed how, independently of the adopted code, the initial dense matrix was reduced to a sparse one. Furthermore, it was also stressed how the total CPU time required for solving a simple

small-size problem was consistently reduced.

We can conclude that the application of well-addressed and properly accelerated *Surface Integral Equations* constitutes an optimal alternative - if not the best option - for solving some specific electromagnetic problems, such as the aforementioned open-boundary problems or related to conductors subjected to marked skin effect which verifies at very high frequencies.

Bibliography

[1] Weng Chew, Mei-Song Tong, and HU Bin. *Integral equation methods for electromagnetic and elastic waves*. Springer Nature, 2022.

[2] Riccardo Torchio. "A volume PEEC formulation based on the cell method for electromagnetic problems from low to high frequency". In: *IEEE Transactions on Antennas and Propagation* 67.12 (2019), pp. 7452–7465.

[3] Zhen Peng, Kheng-Hwee Lim, and Jin-Fa Lee. "A Discontinuous Galerkin Surface Integral Equation Method for Electromagnetic Wave Scattering From Nonpenetrable Targets". In: *IEEE Transactions on Antennas and Propagation* 61.7 (2013), pp. 3617–3628. DOI: 10.1109/TAP.2013.2258394.

[4] Gaobiao Xiao and Yibei Hou. "Intuitive Formulation of Discontinuous Galerkin Surface Integral Equations for Electromagnetic Scattering Problems". In: *IEEE Transactions on Antennas and Propagation* 65.1 (2017), pp. 287–294. DOI: 10.1109/TAP.2016.2630501.

[5] Zhi-Guo Qian and Weng Cho Chew. "Fast Full-Wave Surface Integral Equation Solver for Multiscale Structure Modeling". In: *IEEE Transactions on Antennas and Propagation* 57.11 (Nov. 2009), pp. 3594–3601. DOI: 10.1109/tap.2009.2023629. URL: https://doi.org/10.1109/tap.2009.2023629.

[6] Tian Xia et al. "An Enhanced Augmented Electric-Field Integral Equation Formulation for Dielectric Objects". In: *IEEE Transactions on Antennas and Propagation* 64.6 (June 2016), pp. 2339–2347. DOI: 10.1109/tap.2016.2537389. URL: https://doi.org/10.1109/tap.2016.2537389.

[7] Li Zhang and Mei Song Tong. "Low-Frequency Analysis of Lossy Interconnect Structures Based on Two-Region Augmented Volume-Surface Integral Equations". In: *IEEE Transactions on Antennas and Propagation* 70.4 (Apr. 2022), pp. 2863–2872. DOI: 10.1109/tap.2021.3118849. URL: https://doi.org/10.1109/tap.2021.3118849.

[8] Piergiorgio Alotto et al. *The cell method for electrical engineering and multiphysics problems: an introduction*. Vol. 230. Springer Science & Business Media, 2013.

[9] ACL Barnard et al. "The application of electromagnetic theory to electrocardiology: II. Numerical solution of the integral equations". In: *Biophysical Journal* 7.5 (1967), pp. 463–491.

[10] Jussi Rahola and Satu Tissari. "Iterative solution of dense linear systems arising from the electrostatic integral equation in MEG". In: *Physics in Medicine & Biology* 47.6 (2002), p. 961.

[11] Tian Xia et al. "An Integral Equation Modeling of Lossy Conductors With the Enhanced Augmented Electric Field Integral Equation". In: *IEEE Transactions on Antennas and Propagation* 65.8 (Aug. 2017), pp. 4181–4190. DOI: 10.1109/tap.2017.2718587. URL: https://doi.org/10.1109/tap.2017.2718587.

[12] Sadasiva Rao, Donald Wilton, and Allen Glisson. "Electromagnetic scattering by surfaces of arbitrary shape". In: *IEEE Transactions on antennas and propagation* 30.3 (1982), pp. 409–418.

[13] P. Yla-Oijala and M. Taskinen. "Calculation of cfie impedance matrix elements with RWG and n x RWG functions". In: *IEEE Transactions on Antennas and Propagation* 51.8 (Aug. 2003), pp. 1837–1846. DOI: 10.1109/tap.2003.814745. URL: https://doi.org/10.1109/tap.2003.814745.

[14] Annalisa Buffa and Snorre Christiansen. "A dual finite element complex on the barycentric refinement". In: *Mathematics of computation* 76.260 (2007), pp. 1743–1769.

[15] Francesco P Andriulli et al. "A multiplicative Calderon preconditioner for the electric field integral equation". In: *IEEE Transactions on Antennas and Propagation* 56.8 (2008), pp. 2398–2412.

[16] Francesco P Andriulli et al. "On a well-conditioned electric field integral operator for multiply connected geometries". In: *IEEE transactions on antennas and propagation* 61.4 (2012), pp. 2077–2087.

[17] Seppo Jarvenpaa, Matti Taskinen, and P Yla-Oijala. "Singularity subtraction technique for high-order polynomial vector basis functions on planar triangles". In: *IEEE transactions on antennas and propagation* 54.1 (2006), pp. 42–49.

[18] M. Fabbri. "Magnetic Flux Density and Vector Potential of Uniform Polyhedral Sources". In: *IEEE Transactions on Magnetics* 44.1 (Jan. 2008), pp. 32–36. DOI: 10.1109/tmag.2007.908698. URL: https://doi.org/10.1109/tmag.2007.908698.

[19] Robert A Werner and Daniel J Scheeres. "Exterior gravitation of a polyhedron derived and compared with harmonic and mascon gravitation representations of asteroid 4769 Castalia". In: *Celestial Mechanics and Dynamical Astronomy* 65 (1996), pp. 313–344.

[20] Ilari Hanninen, Matti Taskinen, and Jukka Sarvas. "Singularity subtraction integral formulae for surface integral equations with RWG, rooftop and hybrid basis functions". In: *Progress In Electromagnetics Research* 63 (2006), pp. 243–278.

[21] DRSM Wilton et al. "Potential integrals for uniform and linear source distributions on polygonal and polyhedral domains". In: *IEEE Transactions on Antennas and Propagation* 32.3 (1984), pp. 276–281.

[22] Roberto D Graglia. "On the numerical integration of the linear shape functions times the 3-D Green's function or its gradient on a plane triangle". In: *IEEE transactions on antennas and propagation* 41.10 (1993), pp. 1448–1455.

[23] S Caorsi, D Moreno, and F Sidoti. "Theoretical and numerical treatment of surface integrals involving the free-space Green's function". In: *IEEE transactions on antennas and propagation* 41.9 (1993), pp. 1296–1301.

[24] Thomas F Eibert and Volkert Hansen. "On the calculation of potential integrals for linear source distributions on triangular domains". In: *IEEE transactions on antennas and propagation* 43.12 (1995), pp. 1499–1502.

[25] Zhi Guo Qian, Weng Cho Chew, and R. Suaya. "Generalized Impedance Boundary Condition for Conductor Modeling in Surface Integral Equation". In: *IEEE Transactions on Microwave Theory and Techniques* 55.11 (Nov. 2007), pp. 2354–2364. DOI: 10.1109/tmtt.2007.908678. URL: https://doi.org/10.1109/tmtt.2007.908678.

[26] S. Rao, D. Wilton, and A. Glisson. "Electromagnetic scattering by surfaces of arbitrary shape". In: *IEEE Transactions on Antennas and Propagation* 30.3 (May 1982), pp. 409–418. DOI: 10.1109/tap.1982.1142818. URL: https://doi.org/10.1109/tap.1982.1142818.

[27] Athanasios G. Polimeridis et al. "DIRECTFN: Fully Numerical Algorithms for High Precision Computation of Singular Integrals in Galerkin SIE Methods". In: *IEEE Transactions on Antennas and Propagation* 61.6 (June 2013), pp. 3112–3122. DOI: 10.1109/tap.2013.2246854. URL: https://doi.org/10.1109/tap.2013.2246854.

[28] Athanasios G. Polimeridis. *DIRECTFN package*. 2012. URL: http://lema.epfl.ch/Members/thanos/Software.html.

[29] H. Contopanagos et al. "Well-conditioned boundary integral equations for three-dimensional electromagnetic scattering". In: *IEEE Transactions on Antennas and Propagation* 50.12 (Dec. 2002), pp. 1824–1830. ISSN: 0018-926X. DOI: 10.1109/tap.2002.803956. URL: http://dx.doi.org/10.1109/TAP.2002.803956.

[30] Yang Liu et al. "A Scalable Parallel PWTD-Accelerated SIE Solver for Analyzing Transient Scattering From Electrically Large Objects". In: *IEEE Transactions on Antennas and Propagation* 64.2 (Feb. 2016), pp. 663–674. ISSN: 1558-2221. DOI:

10.1109/tap.2015.2508483. URL: http://dx.doi.org/10.1109/TAP.2015.2508483.

[31] Pasi Yla-Oijala et al. "Surface Integral Equation-Based Characteristic Mode Formulation for Penetrable Bodies". In: *IEEE Transactions on Antennas and Propagation* 66.7 (July 2018), pp. 3532–3539. ISSN: 1558-2221. DOI: 10.1109/tap.2018.2835313. URL: http://dx.doi.org/10.1109/TAP.2018.2835313.

[32] CJ Reddy et al. "Fast RCS computation over a frequency band using method of moments in conjunction with asymptotic waveform evaluation technique". In: *IEEE Transactions on Antennas and Propagation* 46.8 (1998), pp. 1229–1233.

[33] CC Lu and WC Chew. "Electromagnetic scattering from material coated PEC objects: a hybrid volume and surface integral equation approach". In: *IEEE Antennas and Propagation Society International Symposium. 1999 Digest. Held in conjunction with: USNC/URSI National Radio Science Meeting (Cat. No. 99CH37010)*. Vol. 4. IEEE. 1999, pp. 2562–2565.

[34] Cagatay Uluisik et al. "Radar cross section (RCS) modeling and simulation, part 1: a tutorial review of definitions, strategies, and canonical examples". In: *IEEE Antennas and Propagation Magazine* 50.1 (2008), pp. 115–126.

[35] Levent Sevgi, Zubair Rafiq, and Irfan Majid. "Radar cross section (RCS) measurements [Testing ourselves]". In: *IEEE Antennas and Propagation Magazine* 55.6 (2013), pp. 277–291.

[36] James R Nagel. "Induced eddy currents in simple conductive geometries: mathematical formalism describes the excitation of electrical eddy currents in a time-varying magnetic field". In: *IEEE Antennas and Propagation Magazine* 60.1 (2017), pp. 81–88.

[37] Constantine A Balanis. *Advanced engineering electromagnetics*. John Wiley & Sons, 2012.

[38] Dimitris Achlioptas and Frank McSherry. "Fast computation of low-rank matrix approximations". In: *Journal of the ACM (JACM)* 54.2 (2007), 9–es.

[39] Ivan V Oseledets. "Tensor-train decomposition". In: *SIAM Journal on Scientific Computing* 33.5 (2011), pp. 2295–2317.

[40] Christian Lubich et al. "Dynamical Approximation by Hierarchical Tucker and Tensor-Train Tensors". In: *SIAM Journal on Matrix Analysis and Applications* 34.2 (Jan. 2013), pp. 470–494. ISSN: 1095-7162. DOI: 10.1137/120885723. URL: http://dx.doi.org/10.1137/120885723.

[41] Zhuotong Chen, Shucheng Zheng, and Vladimir I Okhmatovski. "Tensor train accelerated solution of volume integral equation for 2-D scattering problems and magneto-quasi-static characterization of multiconductor transmission lines". In: *IEEE Transactions on Microwave Theory and Techniques* 67.6 (2019), pp. 2181–2196.

[42] J-R Poirier, Olivier Coulaud, and Oguz Kaya. "Fast BEM solution for 2-D scattering problems using quantized tensor-train format". In: *IEEE Transactions on Magnetics* 56.3 (2020), pp. 1–4.

[43] Antonino Vacalebre, Silvano Pitassi, and Ruben Specogna. "Low-rank compression techniques in integral methods for eddy currents problems". In: *Computer Physics Communications* 289 (2023), p. 108756.

[44] Mauro Passarotto, Silvano Pitassi, and Ruben Specogna. "Foundations of volume integral methods for eddy current problems". In: *Computer Methods in Applied Mechanics and Engineering* 392 (Mar. 2022), p. 114626. ISSN: 0045-7825. DOI: 10.1016/j.cma.2022.114626. URL: http://dx.doi.org/10.1016/j.cma.2022.114626.

[45] Nader Engheta et al. "The fast multipole method (FMM) for electromagnetic scattering problems". In: *IEEE Transactions on Antennas and Propagation* 40.6 (1992), pp. 634–641.

[46] JM Song and Weng Cho Chew. "Fast multipole method solution of three dimensional integral equation". In: *IEEE Antennas and Propagation Society International Symposium. 1995 Digest.* Vol. 3. IEEE. 1995, pp. 1528–1531.

[47] YH Chen, WC Chew, and S Zeroug. "Fast multipole method as an efficient solver for 2D elastic wave surface integral equations". In: *Computational mechanics* 20.6 (1997), pp. 495–506.

[48] B. Carpentieri et al. "Combining Fast Multipole Techniques and an Approximate Inverse Preconditioner for Large Electromagnetism Calculations". In: *SIAM Journal on Scientific Computing* 27.3 (Jan. 2005), pp. 774–792. DOI: 10.1137/040603917. URL: https://doi.org/10.1137/040603917.

[49] Ismatullah and T.F. Eibert. "Surface Integral Equation Solutions by Hierarchical Vector Basis Functions and Spherical Harmonics Based Multilevel Fast Multipole Method". In: *IEEE Transactions on Antennas and Propagation* 57.7 (July 2009), pp. 2084–2093. DOI: 10.1109/tap.2009.2021932. URL: https://doi.org/10.1109/tap.2009.2021932.

[50] Vladimir Rokhlin. "Rapid solution of integral equations of classical potential theory". In: *Journal of computational physics* 60.2 (1985), pp. 187–207.

[51] Piergiorgio Alotto, Paolo Bettini, and Ruben Specogna. "Sparsification of BEM matrices for large-scale eddy current problems". In: *IEEE Transactions on Magnetics* 52.3 (2015), pp. 1–4.

[52] Riccardo Torchio, Paolo Bettini, and Piergiorgio Alotto. "PEEC-based analysis of complex fusion magnets during fast voltage transients with H-matrix compression". In: *IEEE Transactions on Magnetics* 53.6 (2017), pp. 1–4.

[53] Riccardo Torchio et al. "Fast uncertainty quantification in low frequency electromagnetic problems by an integral equation method based on hierarchical matrix compression". In: *IEEE Access* 7 (2019), pp. 163919–163932.

[54] Dimitri Voltolina et al. "High-performance PEEC analysis of electromagnetic scatterers". In: *IEEE Transactions on Magnetics* 55.6 (2019), pp. 1–4.

[55] Riccardo Torchio et al. "Challenges in the EM Simulation of Large Scale Thermonuclear Fusion Devices". In: *2021 International Applied Computational Electromagnetics Society Symposium (ACES)*. IEEE. 2021, pp. 1–4.

[56] F Lucchini and N Marconato. "A comparison between current-based integral equations approaches for eddy current problems". In: *Journal of Physics: Conference Series*. Vol. 2090. 1. IOP Publishing. 2021, p. 012137.

[57] F Lucchini and N Marconato. "Accelerating the charge inversion algorithm with hierarchical matrices for gas insulated systems". In: *Journal of Physics: Conference Series*. Vol. 2090. 1. IOP Publishing. 2021, p. 012136.

[58] Nicolas Boullé and Alex Townsend. "A generalization of the randomized singular value decomposition". In: *arXiv preprint arXiv:2105.13052* (2021).

[59] Nathan Halko, Per-Gunnar Martinsson, and Joel A Tropp. "Finding structure with randomness: Probabilistic algorithms for constructing approximate matrix decompositions". In: *SIAM review* 53.2 (2011), pp. 217–288.

[60] TY Li and Zhonggang Zeng. "A rank revealing method and its applications". In: *preprint* (2003).

[61] K. Zhao, M.N. Vouvakis, and J.-F. Lee. "The Adaptive Cross Approximation Algorithm for Accelerated Method of Moments Computations of EMC Problems". In: *IEEE Transactions on Electromagnetic Compatibility* 47.4 (Nov. 2005), pp. 763–773. DOI: 10.1109/temc.2005.857898. URL: https://doi.org/10.1109/temc.2005.857898.

[62] Steffen Börm, Lars Grasedyck, and Wolfgang Hackbusch. "Introduction to hierarchical matrices with applications". In: *Engineering Analysis with Boundary Elements* 27.5 (May 2003), pp. 405–422. ISSN: 0955-7997. DOI: 10.1016/s0955-7997(02)00152-2. URL: http://dx.doi.org/10.1016/S0955-7997(02)00152-2.

[63] Lars Grasedyck. "Theorie und anwendungen hierarchischer matrizen". PhD thesis. 2001.

[64] Lars Grasedyck and Wolfgang Hackbusch. "Construction and arithmetics of H-matrices". In: *Computing* 70 (2003), pp. 295–334.

[65] Achi Brandt. "Algebraic multigrid theory: The symmetric case". In: *Applied mathematics and computation* 19.1-4 (1986), pp. 23–56.

[66] Ulrike Meier Yang et al. "BoomerAMG: A parallel algebraic multigrid solver and preconditioner". In: *Applied Numerical Mathematics* 41.1 (2002), pp. 155–177.